Norwegian University
of Life Sciences

Master's Thesis 2024 60 ECTS
Faculty of Environmental Sciences and Natural Resource Management

Investigation of cobalt nanoparticle induced toxicity and hypoxic response in *Caenorhabditis elegans*

Tania Kaur Walia
Environmental Science

Acknowledgments

This thesis is the final part of a master's program in Environment Science at the Norwegian University of Life Sciences (NMBU). The project was funded by The Faculty of Environmental Sciences and Natural Resource Management (MINA) and all experimental work was performed at the Isotope Laboratory at NMBU. The work was supervised by Dr. Dag Anders Brede (main supervisor), Dr. Erica Maremonti (co-supervisor), and Dr. Lisa Magdalena Rossbach (co-supervisor).

I sincerely thank Dag for his time and wisdom, and for offering an open door whenever I needed guidance. His expertise, support, and patience have been instrumental in this project's progress. I also want to express my deep gratitude to Erica for her constant assistance and accessibility, always making time to help me and address my questions. Additionally, I want to thank Lisa for her invaluable contributions to nanoparticle preparation and characterization. It was an absolute pleasure working with each of you!

Special thanks to Lene Cecilie Hermansen and Hilde Raanaas Kolstad for their assistance with fluorescence imaging, Karl Andreas for his help with ICP-MS measurements, and Marit Nandrup Pettersen for the training.

Thanks to everyone at the Isotope Laboratory for their warm welcome.

To my fellow students and friends, thank you for your camaraderie, encouragement, laughter, and moments of joy. These shared experiences have enriched my academic journey in countless ways.

Lastly, I express my deepest gratitude to my family for their unwavering support and encouragement. Their prayers and dedication to creating opportunities have been the cornerstone of my achievements. Thank you for believing in me and allowing me to chase my dreams with confidence and determination.

Tania Kaur Walia

Ås, May 2024

Abstract

The use of nanoparticles, defined as particles smaller than 100 nm, is experiencing a notable surge worldwide. Among these are cobalt nanoparticles (CoNPs) which have applications across various fields including electronics, biotechnology, medicine, and aerospace engineering. With their widespread use, organisms face an elevated risk of exposure to CoNPs. Despite their prevalence, the understanding of the toxicity potential and underlying mechanisms of CoNPs is limited. This study addresses this knowledge gap by investigating the toxic effects of CoNPs compared to those of cobalt chloride ($CoCl_2$) employing the model organism *C. elegans*.

The CoNPs were characterized with respect to size and surface charge. Transmission electron microscopy (TEM) micrographs revealed a high degree of NP aggregation, with individual particles in the NP suspension measuring smaller than 10 nm. Dynamic light scattering (DLS) determined an NP hydrodynamic diameter of 155 ± 0.8 mm with a polydispersity index of 0.362 ± 0.011. The zeta potential of CoNPs was -16.2 ± 0.3 mV, indicating low suspension stability.

Chronic toxicity tests revealed that CoNPs cause less potent toxicity on growth and reproduction compared to $CoCl_2$. It was demonstrated that CoNP toxicity could to a significant extent be ascribed to ion leaching Additionally, observations of the effects of CoNPs on reproduction suggest there are particle-specific mechanisms that contribute to the toxicity of CoNPs.

CoNPs were shown to induce a hypoxic response in *C. elegans* following acute exposure. The observations revealed that the assessed hypoxic response, expression of nhr-57, is highly localized to embryos.

Additionally, vulva abnormalities were observed across all exposure concentrations in nematodes subject to acute exposure to $CoCl_2$. Nematodes exposed to CoNPs did not display similar vulva abnormalities.

This project has confirmed the potential toxic effects of CoNPs and their potential risk to the environment. The results indicate unidentified particle-specific mechanisms contribute to the toxicity of CoNPs. Further studies should focus on understanding the particle-specific mechanisms that cause effects on growth, reproduction, and induction of hypoxic response following CoNP exposure.

Sammendrag

Bruken av nanopartikler, definert som partikler mindre enn 100 nm, opplever en betydelig økning på verdensbasis. Blant disse er kobaltnanopartikler (CoNPs), som anvendes innen mange ulike felt inkludert elektronikk, bioteknologi, medisin og luftfartsteknologi. Den utbredte bruken har også økt organismers risikoen for å bli eksponert for CoNPs. Til tross for deres utbredelse, er det toksiske potensialet og de underliggende mekanismene til CoNPs toksisitet ikke godt forstått. Denne oppgaven skal ta tak i dette kunnskapshuller ved å undersøke de toksiske effektene av CoNPs og sammenligne de med kobaltklorid ($CoCl_2$) ved å bruke modellorganismen *C. elegans*.

CoNPs ble karakterisert med tanke på størrelse og overflateladning. Bilder fra Ttransmisjonselektronmikroskopi (TEM) viste høy grad av NP aggregering. TEM bildene avslørte også at individuelle partikler i NP suspensjonen hadde en størrelse på mindre enn 10 nm. Dynamisk lysspredning (DLS) målte en hydrodynamisk diameter på 155 ± 0.8 nm og en polydispersitetsindeks (PDI) på 0.362 ± 0.011. Zeta potentialet til CoNPs var -16.2 ± 0.3 mV, som indikerer lav suspensjonsstabilitet.

Kroniske toksisitetstester avslørte at CoNPs ikke forårsaket like stor grad av potent toksisitet på vekst og reproduksjon som $CoCl_2$. Det ble også vist at den observerte toksisiteten til CoNP i stor grad kunne tilskrives utlekking av ioner. I tillegg viser observasjonene i denne oppgaven at den toksiske effekten av CoNPs på reproduksjon kan skyldes partikkelspesifikke mekanismer.

Det ble vist at akutt eksponering for CoNPs indusere hypoksisk respons i *C. elegans*. Observasjoner viser at den induserte hypoksiske responsen, uttrykk av nhr-57, er i hovedsak lokalisert i embryoene.

Hos nematoder utsatt for akutt eksponering for $CoCl_2$ ble det observert vulva abnormiteter. Slike abnormiteter ble ikke observert hos nematoder eksponert for CoNPs.

Denne oppgaven har bekreftet de potensielle toksiske effektene av CoNPs i miljøet. Resultatene peker mot en potensiell, men ennå udefinert partikkelspesifikk mekanisme forårsaker effekter på vekst, reproduksjon og induksjon av hypoksisk respons ved eksponering for CoNPs.

Abbreviations

Co	Cobalt
$CoCl_2$	Cobalt chloride
CoNP	Cobalt nanoparticle
DLS	Dynamic light scattering
EC50	Half maximal effective concentration
EGL-9	Egg-laying abnormal-9
GFP	Green fluorescent protein
HIF	Hypoxia-inducible factor
HRE	Hypoxia response element
ICP-MS	Inductively coupled plasma mass spectrometry
LMM	Low molecular mass
MHRW	Moderately hard reconstituted water
N2	Wild type Bristol *C. elegans* strain
nhr-57	Nuclear hormone receptor 57
NP	Nanoparticle
PHDs	Prolyl hydroxylases
Pnhr-57	Promoter region associated with the nhr-57 gene
RCF	Relative centrifugal force
ROS	Reactive oxygen species
rpm	Rotations per minute
TEM	Transmission electron microscopy
VHL	von Hippel-Lindau tumor suppressor protein
VPC	Vulval precursor cell
ZG120	*C. elegans* reporter strain *iaIs07[Pnhr-57::gfp unc-119 (+)] IV*
ZG444	*C. elegans* reporter strain *iaIs07[Pnhr-57::gfp unc-119 (+)] IV; egl-9 (gk277) V*

Table of contents

1. Introduction

Toxicology is the study of adverse effects of chemical, physical, and biological agents on living organisms (Kent, 1998; Pope et al., 2020). In the 16th century, the Swiss physician Paracelsus, widely regarded as the founding father of modern toxicology, famously declared, *"Solely the dose determines that a thing is not a poison"* (Sola dosis facit venenum) (P. G. C. Campbell et al., 2022). Through this assertion, he introduced the relationship between toxicant exposure dose and biological response. Additionally, the species of the toxicant significantly influence availability for biological uptake, while environmental factors such as temperature, pH, and ionic strength can render seemingly harmless substances lethal under altered conditions (VanLoon & Duffy, 2017).

The recent surge of interest in nanotechnology has led to the emergence of nanotoxicology, driven by concerns about the potential adverse effects associated with nanoparticles (NPs) (Donaldson, 2004). Unlike bulk materials, the toxicity of NPs may largely be attributed to their small size and surface chemistry (P. G. C. Campbell et al., 2022). The widespread application of various NPs prompts a growing demand for comprehensive nanotoxicological research, intending to bridge the existing knowledge gaps and inform regulatory frameworks (P. G. C. Campbell et al., 2022; Donaldson, 2004).

Cobalt (Co) is a transition metal with widespread industrial applications, particularly in rechargeable batteries and superalloys for aircraft turbine engines (Khusnuriyalova et al., 2021; Slack et al., 2017). The recent technological and industrial developments of renewable energy have increased the demand for Co (G. A. Campbell, 2020; Fu et al., 2020). Co^{2+} appears to be the most bioavailable form of cobalt, and its toxic mechanisms and effects have been investigated thoroughly in a range of organisms (Leyssens et al., 2017; Simonsen et al., 2012). Previous studies have demonstrated that Co^{2+} exposure causes multiple toxic effects, including hypoxic response (Padmanabha et al., 2015; Simonsen et al., 2012; Triantafyllou et al., 2006).

Concurrently, cobalt nanoparticles (CoNPs) have emerged as efficient NPs in catalysis, and therefore widely used in both industrial and medical fields (Cagno et al., 2017; Khusnuriyalova et al., 2021). As a result of their widespread use and prevalence, organisms face a heightened risk of exposure to CoNPs. NPs, including CoNPs, are known to be highly reactive due to their small size and high specific surface area (Jiang et al., 2009). However, limited research has been conducted to investigate the potential effect of CoNP exposure on organisms (Cagno et al., 2017). Previous studies examining the physical, chemical, and toxicological properties of

CoNPs have shown adverse effects on the earthworm *Eisenia fetida* (Coutris et al., 2012; Oughton et al., 2008). Therefore, investigating the effects of CoNP exposure on living organisms is highly relevant (Cagno et al., 2017).

The objective of this master's project was to investigate the toxicity of CoNPs compared to that of Co ions and determine whether CoNP exposure induced a hypoxic response. The CoNPs were characterized, and the possible mechanism of toxicity was investigated using *Caenorhabditis elegans* (*C. elegans*) as the model organism. The following research questions were investigated during this project:

I. Does Co ion leaching from CoNPs contribute to toxicity?
II. Do CoNPs induce particle-specific toxic effects?
III. Does chronic CoNP exposure induce a hypoxic response in *C. elegans*?
IV. Does acute CoNP exposure induce a hypoxic response in *C. elegans*?

To address research questions I and II, the following set of hypotheses were formulated:

H0: Particle-specific mechanisms do not contribute to the toxicity of CoNPs.

H1: Particle-specific mechanisms contribute significantly to the toxicity of CoNPs.

To address research questions III and IV, the following set of hypotheses were formulated:

H0. CoNP exposure does not induce a hypoxic response in *C. elegans.*

H1: CoNP exposure induces a significant hypoxic response in *C. elegans*.

2. Theory

2.1. Cobalt

Cobalt (Co) is a hard silver-gray metal and comprises 29 ppm of the Earth's crust (Slack et al., 2017). Although Co in its pure form is not naturally occurring, Co-bearing minerals and compounds are abundant and widespread (Slack et al., 2017). The production of Co is primarily a byproduct of nickel and copper mining (G. A. Campbell, 2020). From 1950 to 2011, there has been a tenfold increase in Co production. Notable, over 50% of global Co production originates from the Democratic Republic of the Congo, while countries including Canada, China, Russia, Zambia, Cuba, Australia, and Brazil account for less than 7% of the production each (G. A. Campbell, 2020; Slack et al., 2017).

The metal finds a wide range of applications due to its key properties, including prominent hardness, enhanced wear resistance when incorporated into metal alloys, relatively low thermal and electrical conductivity, a high melting point, and multiple oxidation states. Additionally, Co exhibits ferromagnetism, retaining this magnetic property at the highest temperature of any metal (Khusnuriyalova et al., 2021; Slack et al., 2017). Historically, Co has been valued for its rich blue hue, produced by heating cobalt (II) oxide with aluminum oxide or silica (Slack et al., 2017; Zhang et al., 2023). This vibrant blue pigment has been used for centuries in ceramics, glass, paints, and other applications. Co is an important component in rechargeable batteries, which are used in consumer electronics, electric and hybrid electric vehicles, energy storage units, and power tools (Slack et al., 2017). Additionally, Co is frequently employed in alloys, enhancing mechanical properties such as hardness, strength, and corrosion resistance. These alloys are used for manufacturing components utilized in various industries, including aerospace, automotive, construction, mining, and medical. (Slack et al., 2017).

The solubility and transport of Co are influenced by pH, ionic strength, and temperature (L. Chen et al., 2011). Co is usually concentrated in sulfide and arsenide minerals. The instability of these minerals causes Co, typically occurring as Co^{2+} and Co^{3+}, to dissolve from host minerals in weathering environments on Earth's surface (Slack et al., 2017). The dissolution of sulfide minerals, in particular, releases metals and forms sulfuric acid. This results in a lower pH and enhances the dissolution of metals. These metals, including Co, can migrate through precipitation, sorption onto oxide minerals, or dilution by mixing with circumneutral pH water

(VanLoon & Duffy, 2017). If the metals are not remediated, Co and other metals can be dispersed more widely in the environment (Slack et al., 2017).

Biological functions

Co is a trace element essential for many life forms, primarily because it is a vital component of the active site of vitamin B12, also known as cobalamin. Vitamin B12 acts as an enzyme cofactor in various physiological processes, including red blood cell formation (erythropoiesis), DNA synthesis, neurological functions, and energy metabolism (González-Montaña et al., 2020; Rizzo & Laganà, 2020). The central Co atom in vitamin B12 (Figure 1) can exist in three distinct oxidation states: I, II, and III. These various states enable different ligands to coordinate around the Co atom, resulting in alterations to the configuration of vitamin B12. The conformation of vitamin B12 is crucial for its interaction with chaperones and target proteins, as well as for regulating its reactivity in catalytic processes (Osman et al., 2021; Patel, 2020).

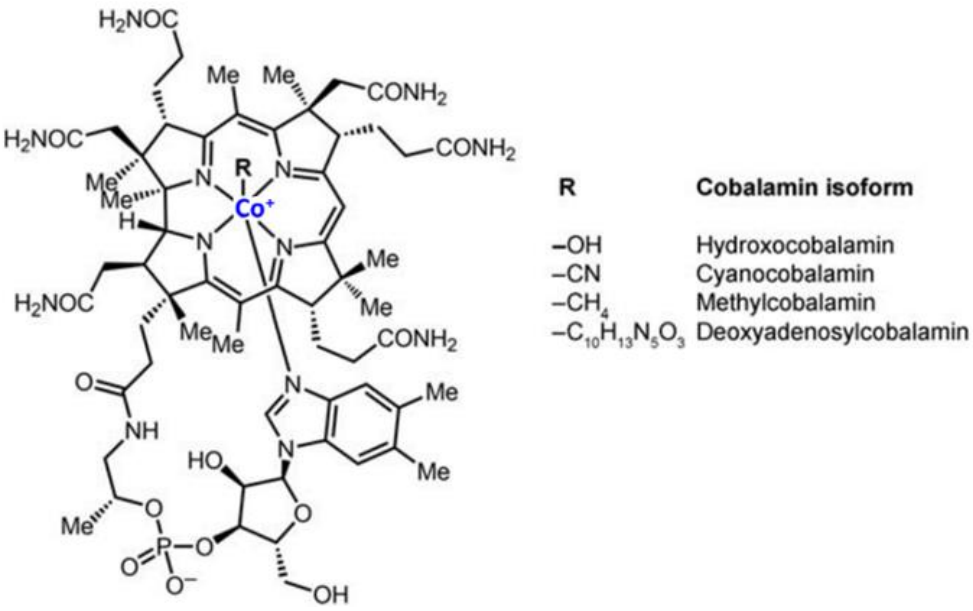

Figure 1: Structure of vitamin B12, specifically the cyanocobalamin isoform. The figure also illustrates the most common ligands (R) that bind to Co (highlighted in blue), thereby characterizing the different vitamin B12 isoforms. Adapted from Patel (2020).

Most animals lack the necessary enzymes required to synthesize vitamin B12. Consequently, they rely on obtaining it through their diet or the absorption of vitamin B12 produced by intestinal or ruminal bacteria (González-Montaña et al., 2020; Patel, 2020) Ruminants, such as cows, goats, and sheep, can absorb vitamin B12 synthesized by bacteria within their rumen. However, in various animals, including humans, efficient absorption of vitamin B12 produced

by bacteria in their intestines is limited (González-Montaña et al., 2020). Vitamin B12 deficiency is linked to conditions like megaloblastic anemia, neurological disorders, developmental abnormalities, and metabolic disorders (González-Montaña et al., 2020; Osman et al., 2021). Therefore, ensuring adequate dietary intake of vitamin B12 is essential for maintaining optimal health.

2.2. Cobalt toxicity

Excess Co, particularly Co^{2+}, is associated with a range of adverse effects. In 2016, Co was named the "Allergen of the Year" by the American Contact Dermatitis Society, as Co is capable of causing contact dermatitis (Burkemper, 2015; Duarte et al., 2018). Studies show that severe cases of Co toxicity in humans can lead to neurotoxicity, pneumonia, and increased risk of lung cancer when inhaled (Barceloux, 1999; Leyssens et al., 2017; Osman et al., 2021). It is essential to understand the balance between Co necessity and its potential harm to ensure both organism health and environmental sustainability (Osman et al., 2021).

Several mechanisms of Co toxicity stem from the competitive relationship between Co and iron (Fe) (Osman et al., 2021). Given their similar size and charge, Co^{2+} can interfere with the cellular functions of Fe^{2+} by outcompeting Fe at metal binding sites, for example during the formation of heme (Majtan et al., 2011; Ranquet et al., 2007). This can cause inhibition of crucial enzymes, including those involved in mitochondrial respiration (Barceloux, 1999; González-Montaña et al., 2020). Additionally, it has been suggested that Co^{2+} acts as an antagonist of the calcium (Ca^{2+}) channel, thereby inhibiting Ca^{2+} entry into cells (Simonsen et al., 2012). This can disrupt normal cellular processes that rely on Ca^{2+} signaling, including neurotransmitter release, muscle contraction, and cell signaling. Co^{2+} also competes with Ca^{2+} for intracellular Ca^{2+}-binding proteins(González-Montaña et al., 2020; Simonsen et al., 2012).

It is well documented that Co^{2+} induces the production of reactive oxygen species (ROS) within cells (Leonard et al., 1998). ROS lead to oxidative DNA damage and inhibit DNA repair mechanisms, rendering Co^{2+} genotoxic (Leonard et al., 1998; Osman et al., 2021; Simonsen et al., 2012). Furthermore, Co^{2+} may activate the hypoxia-inducible factor (HIF), a key regulator of genes sensitive to hypoxia (Simonsen et al., 2012). By replacing Fe^{2+} at the active site of proline hydroxylases, Co^{2+} leads to the inactivation of these enzymes (Yuan et al., 2003). This interference ultimately results in an accumulation of HIF, which alters various cellular mechanisms, including angiogenesis, erythropoiesis, glucose transport, and modulation of

apoptosis and cell proliferation, to adapt to the hypoxic environment. The ability of Co^{2+} to activate HIF under normoxic conditions can be favorable for tumor progression, and enhance performance in athletes (Brewer et al., 2016; Simonsen et al., 2012).

2.3. Hypoxia

Multicellular organisms rely on a continuous supply of oxygen (O_2) to sustain vital cellular functions. O_2 serves as the final electron acceptor in oxidative phosphorylation, a process by which cells produce energy in the form of adenosine triphosphate (ATP) (Nelson et al., 2017). The electron transport chain functions optimally under normoxic conditions, and deviations from these O_2 levels can disrupt its function (Hockel & Vaupel, 2001; Prabhakar & Semenza, 2015). During instances of decreased O_2 availability, known as hypoxia, the electron transport chain can produce elevated levels of ROS, which induce oxidative damage to lipids, proteins, and DNA within cells (Jomova & Valko, 2011). This oxidative stress can lead to cellular dysfunction and eventual cell death. Thus, organisms have evolved homeostatic mechanisms to tightly regulate O_2 levels within cells and tissues, ensuring an optimal O_2 supply for proper cellular function (Prabhakar & Semenza, 2015).

Hypoxia arises when the O_2 supply fails to meet demand, leading to various biological consequences. Hypoxia induces the transcription of genes involved in glycolysis, glucose transport, angiogenesis, and the expression of survival and growth factors (Hockel & Vaupel, 2001). In mammals, these hypoxia-inducible genes are controlled by hypoxia-inducible factors (HIF), transcriptional factors composed of two subunits, HIF-α and HIF-β (Epstein et al., 2001; G. L. Wang et al., 1995). The activity of HIF is modulated by the O_2-dependent hydroxylation of HIF-α.

In normoxia, prolyl hydroxylases (PHDs) use O_2 as a co-substrate to hydroxylate conserved proline residues in HIF-α (Shao et al., 2009). Proline hydroxylation causes HIF-α to bind to the von Hippel-Lindau tumor suppressor protein (VHL), which recruits an ubiquitin-protein ligase complex, leading to the proteasomal destruction of HIF-α (Epstein et al., 2001; Padmanabha et al., 2015; Shao et al., 2009). However, in hypoxia, decreased PHD activity results in the accumulation of non-hydroxylated HIF-α, which forms a complex with HIF -β (Berra et al., 2006; Padmanabha et al., 2015). The now transcriptionally active HIF binds to hypoxia-response elements (HREs) in the promoter regions of the hypoxia-inducible genes, initiating transcription of genes involved in cellular adaptation to hypoxia.

In *C. elegans* the HIF pathway is conserved and the homologous transcription factor called HIF-1, functions analogously to mammalian HIF-α subunits (Epstein et al., 2001). Epstein and colleagues identified egg-laying abnormal-9 (EGL-9) as the PHD responsible for regulating HIF-1 in *C. elegans* (Berra et al., 2006; Epstein et al., 2001). EGL-9 has both an MYND zinc finger domain and a prolyl hydroxylase domain, with the latter containing a highly conserved Fe(II)-binding pocket in its catalytic core (Shao et al., 2009). Under normoxia, EGL-9 hydroxylates HIF-1 at proline 621, a reaction dependent on the presence of O_2, Fe(II), and 2-oxoglutarate (Shao et al., 2009). The hydroxylation enables the binding of HIF-1 to VHL-1 E3 ligase complex, leading to the degradation of HIF-1 (Figure 2) (Shao et al., 2009).

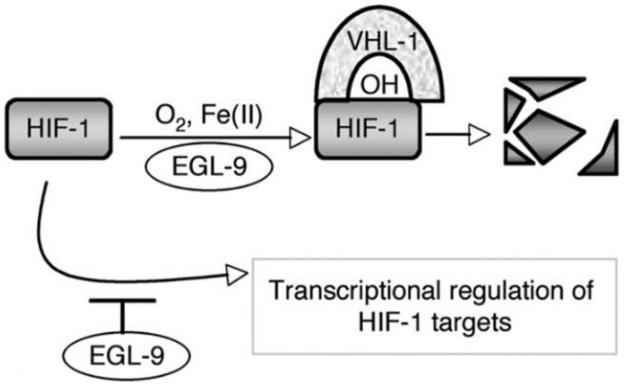

Figure 2: The oxygen-dependent regulation of HIF-1 by EGL-9. Adapted from Shao et al. (2009).

Under hypoxia, the accumulated HIF-1 translocates to the nucleus, where it forms a heterodimer with the HIF-1β subunit. This complex then binds to HREs and activates the transcription of target genes. One such target gene is *nhr-57*, which encodes a nuclear hormone receptor in *C. elegans* (Maxeiner et al., 2019). Nhr-57 regulates the signaling pathways known as RAS/MAPK in vulval precursor cells (VPCs) in *C. elegans* (Maxeiner et al., 2019). Activation of the RAS/MAPK pathway would trigger differentiation of the VPCs. However, nhr-57 inhibits this signaling pathway, preventing premature differentiation of the VPCs (Maxeiner et al., 2019). This allows the VPCs to adjust their developmental fate based on the O_2 levels in their environment.

2.4. Nanotoxicity

Nanoparticles (NPs) are three-dimensional structures that exhibit unique physicochemical properties and functionalities due to their small size, typically less than 100 nm (Jiang et al., 2009). These properties are attributed to two primary factors: their relatively larger surface area, which makes them more chemically reactive, and the influence of quantum effects at the nanoscale, which profoundly impacts optical, electrical, and magnetic characteristics (Donaldson, 2004; The Royal Society, 2004). The distinctive properties of NPs have led to significant attention across various fields including electronics, biotechnology, medicine, and aerospace engineering. For instance, in the medical field, NPs are increasingly used as an innovative delivery system for drugs, proteins, DNA, and monoclonal antibodies (De Jong, 2008). It is, however, important to recognize that the same properties that make NPs industrially valuable also raise concerns regarding their potential adverse health and environmental effects (Donaldson, 2004; The Royal Society, 2004).

To understand the toxicity potential of NPs, toxicological studies must account for various properties of NPs, such as size, dispersion state, surface charge, shape, chemical composition, surface area, and surface chemistry (Jiang et al., 2009). For example, the size of particles dictates the pathway through which they enter cells. NPs, being smaller than 200 nm, can enter cells through endocytosis, reach sensitive tissues, and potentially disrupt normal cellular function (Pourmand & Abdollahi, 2012; Rejman et al., 2004; Vishwakarma et al., 2010). When foreign materials like NPs are taken up via endocytosis, they can trigger inflammatory reactions, leading to oxidative stress response (Pourmand & Abdollahi, 2012). Generally, the toxicity of a particle is inversely proportional to its size (Vishwakarma et al., 2010). Therefore, NPs may be more toxic than larger particles of the same chemical substance. Consequently, the aggregation of NPs may potentially reduce the toxicity of NPs.

Cobalt nanotoxicity

Cobalt nanoparticles (CoNPs) have emerged as materials with diverse applications across various fields due to their remarkable magnetic, electrical, and catalytic properties. They are particularly used in magnetic sensors, magnetic fluids, and catalysis. They are also used for drug delivery and magnetic resonance imaging (MRI) in the medical field (Ansari et al., 2017).

CoNPs have been observed to leach Co^{2+} from their surface into the surrounding medium (Fouad & Hafez, 2018; Ma et al., 2024). The extent of ion leaching can vary depending on factors such as NP size, surface properties, and environmental conditions (Gaikwad et al.,

2007). The leaching of Co^{2+} ions from CoNPs may be a potential mechanism for toxicity, as excess Co^{2+} has been associated with various adverse effects, as discussed in Section 2.2. Therefore, understanding the mechanisms of Co^{2+} release from CoNPs is essential for assessing their potential toxicity.

Previous studies have shown that CoNPs enter leukocytes, interact with DNA, and result in in-vitro genotoxic effects (Colognato et al., 2008). CoNPs may be cytotoxic, as studies conducted on cell lines demonstrated that exposure to magnetic NPs reduced cell viability, inhibited the normal formation of neuronal cells, and decreased mitochondrial activity (Auffan et al., 2006; Brunner et al., 2006; Pisanic et al., 2007; Soto et al., 2007).

2.4. *Caenorhabditis elegans*

C. elegans are small non-parasitic nematodes that survive by feeding primarily on bacteria (Altun & Hall, 2009). Adults are approximately 1 mm long, while newly hatched larvae are 0.25 mm long (Corsi et al., 2015). They are found worldwide in temperate soil environments, as well as in decaying organic matter such as rotting fruit and vegetal material (Kiontke et al., 2011). In response to food scarcity, they can enter a dormant larval stage known as the dauer stage and survive several months without food (Corsi et al., 2015). In laboratory settings, *C. elegans* are easily cultivated on agar plates and fed the bacterium *Escherichia coli* (Meneely et al., 2019).

C. elegans are predominantly hermaphrodites that self-fertilize, as each individual produces both sperm and oocytes. They reach reproductive maturity within three days and can produce about 300 offspring per individual, because of the limited number of sperm (Altun & Hall, 2009; Emmons, 2014). Male individuals arise through spontaneous non-disjunction in the hermaphrodite germ line, occurring at a rate of 0.1%. However, through mating the frequency of male emergence increases substantially, up to 50% (Altun & Hall, 2009). In the presence of males, hermaphrodites are capable of producing approximately 1000 offspring per adult (Corsi et al., 2015).

The life cycle of a hermaphrodite (Figure 3) consists of the embryonic stage, four larval stages (L1-L4), and adulthood. Each transition is marked by molting, during which the old cuticle is shed (Altun & Hall, 2009). Under optimal conditions, an embryo can develop into an adult nematode within three days. After hatching, L1 stage nematodes can undergo developmental

arrest in the absence of food. During this arrested stage, they can survive for 6-10 days, and resume normal development once the conditions improve. At the end of the L2 stage, nematodes may enter an arrested state called the dauer larva if environmental conditions are unfavorable for further growth (Altun & Hall, 2009). A dauer larva can survive in harsh conditions for up to four months. Under favorable conditions the dauer state ends, and the nematode molts to the L4 stage. During the L4 stage, hermaphrodite nematodes reach sexual maturity and germ cells differentiate into mature sperm (Altun & Hall, 2009). Additionally, the egg-laying apparatus undergoes significant development during the L4 larval stage. This apparatus consists of the uterus, the uterine muscles, the vulva, the vulval muscles, and a neuropil (Lints & Hall, 2004). Sperm production stops at the L4/adult molt, and subsequent germline cells exclusively differentiate to produce oocytes (Altun & Hall, 2009). Adult hermaphrodites have fully developed reproductive organs and are fully sexually mature. Matured oocytes are self-fertilized by sperm in the spermatheca, and the resulting zygotes are stored in the uterus and laid outside through the vulva (Altun & Hall, 2009).

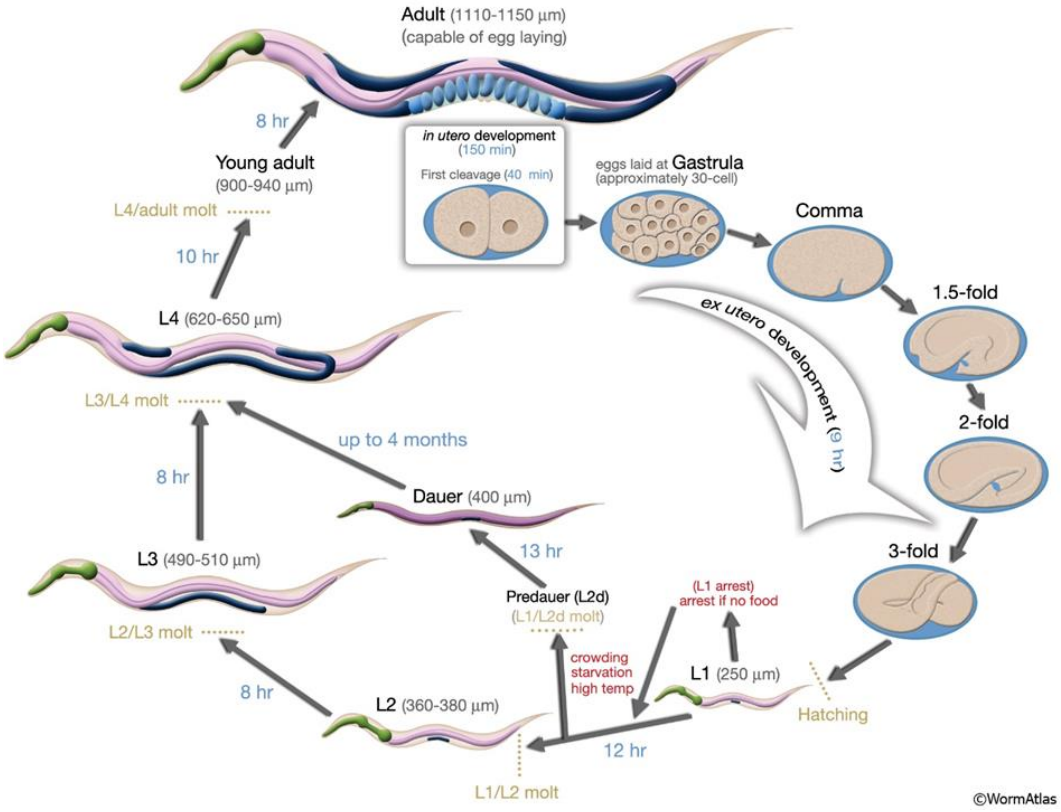

Figure 3: The life cycle of a hermaphrodite *C. elegans*, from egg to adult via four larval stages. Numbers in blue along the arrows indicate the length of time the nematode spends at a certain larval stage at 20°C. Adapted from Altun and Hall (2009).

C. elegans was the first multicellular organism with a fully sequenced genome. The genome contains between 20 250 and 21700 protein-coding genes, and many genes have human homologs (Hunt, 2017; Shaye & Greenwald, 2011). An adult hermaphrodite has 959 somatic cells, which originate from embryonic cells and follow an identical developmental pattern across all individuals. Due to extensive knowledge about its biology and physiology, *C. elegans* is an excellent model organism. Since the 1970s, when their potential as a model organism was first realized, *C. elegans* has been extensively used in a wide range of toxicological studies (Brenner, 1974). Due to their small size and transparent bodies, *C. elegans* are well suited for in vivo imaging, especially fluorescence analysis. Additionally, their short generation time and high fecundity make *C. elegans* an attractive model organism for toxicity tests, especially in nanotoxicology studies due to the tendency of NPs to agglomerate and dissolve over time (Handy et al., 2012). These traits make them a suitable model organism in ecotoxicity research. L1 stage larvae can be age synchronized by using established laboratory protocols, which enables the assessment of the effect of toxic compounds on toxicological endpoints such as survival, fertility, reproduction, and growth.

Furthermore, numerous genetically modified strains of *C. elegans* have been developed for investigation of the underlying mechanisms of toxic effects. The green fluorescent protein (GFP) labeled reporter strains ZG120 and ZG444 are examples of transgenic strains (Shao et al., 2009). The ZG120 is a wildtype GFP label strain, while the ZG444 strain carries an additional *egl-9(gk277)* deletion, which renders EGL-9 partially functional (Shao et al., 2009).

In both ZG120 and ZG444, the gene encoding GFP is under the control of the same promoter (Pnhr-57) as the nuclear hormone receptor 57 (nhr-57) gene. When Pnhr-57 is activated both GFP and nhr-57 are expressed simultaneously. Consequently, the GFP fluorescence signal intensity is correlated with the nhr-57 expression, and ZG120 and ZG444 can be used as reporters of HIF-1 activity and hypoxic response. The GFP fluorescence emission from both the transgenic strains is a quasi-quantifiable measurement, and useful only when compared to a control value.

2.5. Optical microscopy

Optical microscopes, also known as light microscopes, utilize visible light and lenses to magnify the image of a specimen. The transparency of *C. elegans* can pose challenges for conventional bright-field microscopy, due to the low contrast they yield (Mann et al., 2005).

Nematodes can be visualized through staining, such as using Rose Bengal which imparts a fuchsia color to the nematodes. However, staining cannot be done on living specimens. Phase-contrast microscopy can be used to enhance the contrast of transparent, unstained samples. When light passes through a transparent specimen, it undergoes a phase shift compared to the surrounding medium due to differences in refractive index (Davidson & Abramowitz, 1999; Zernike, 1942). This phase shift results in contrast, enabling visualization of the specimen.

Stereo microscopy

A stereo microscope provides a three-dimensional view of the specimen being observed. It uses two separate optical paths with two eyepieces to create a stereoscopic image (Liao et al., 1997). They are commonly used for tasks that require low magnification but high resolution and are therefore a useful tool during *C. elegans* cultivation and research.

Fluorescence microscopy

Fluorescence microscopy is widely used in biological research for visualization and studying various cellular and molecular processes. This imaging technique relies on fluorescent labels, that can be tailored to bind selectively to targets, such as proteins, lipids, ions, or other biomolecules (Sanderson et al., 2014; X. Wang & Lai, 2021). With exceptional contrast and a wide variety of fluorescent labels and transgenic strains, researchers can visualize various cellular and subcellular components within a single specimen. Additionally, the non-invasive nature of fluorescence imaging makes it suitable for live-cell imaging studies, where dynamic processes can be observed in real-time.

The process of fluorescence involves the interaction between light and atoms or molecules within a specimen. Upon absorption of a photon, electrons are excited to higher, unstable energy levels. Subsequently, as these electrons return to their ground state, excess energy is emitted in the form of a new photon, typically of lower energy and longer wavelength. This change in energy levels, known as the Stokes shift, facilitates the differentiation between the emitted fluorescence and the initial excitation light (Sanderson et al., 2014).

In fluorescence microscopy, the process of fluorescence is used to visualize fluorophores, which are molecules that exhibit fluorescence. While many organic substances display autofluorescence, only some are suitable for labeling specific targets of interest. Instead, synthesized compounds are often preferred as they allow for the optimization of excitation and emission wavelengths, and fluorophore efficiency. Additionally, researchers have introduced genetically encoded fluorescent probes. Among these, the GFP is extensively employed for

genetically tagging protein components. In 1992, The GFP gene was cloned from the jellyfish *Aequorea victoria*, and by 1994, Chalfie and colleagues demonstrated its ability to induce fluorescence when expressed in *C. elegans* (Chalfie et al., 1994; Prasher et al., 1992). By fusing the GFP gene to other genes of interest, the expression and localization of those genes can be visualized (Chalfie et al., 1994).

The emitted fluorescence can be detected and quantified using a high-intensity light source to excite fluorophores. In the Leica DM6 B, a fluorescent light microscope, this process begins with a laser followed by an excitation filter, which selectively permits desired wavelengths to pass through (Leica Microsystems GmBH, 2020; Sanderson et al., 2014). Subsequently, a dichroic mirror and objective lens direct this filtered beam onto the specimen, where the photon excites electrons in the fluorophore. The resulting emitted light, a product of fluorescence, then passes the objective lens, dichroic mirror, and an emission filter. This filter blocks unwanted wavelengths from reaching the ocular or the detector. The emitted fluorescence can be viewed by the eyes or captured electronically to generate an image showcasing fluorescence within the specimen (X. Wang & Lai, 2021). Figure 4 shows the schematic illustration of the setup of a fluorescence microscope.

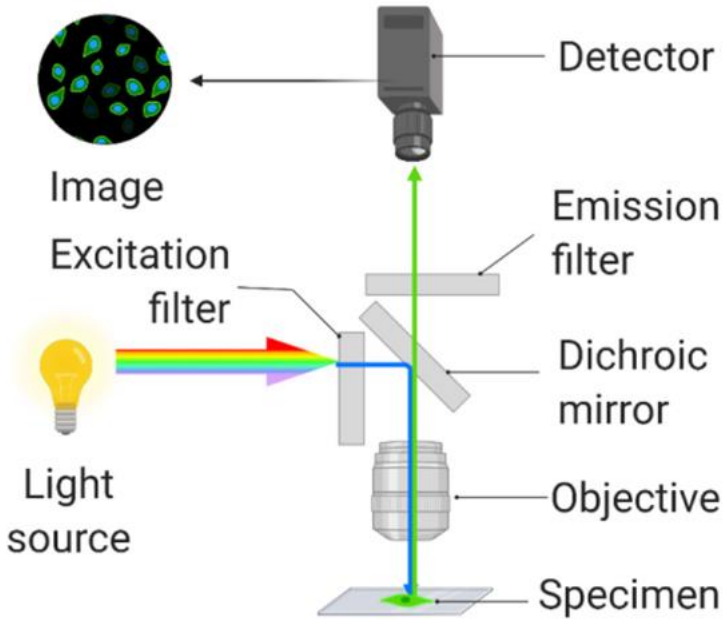

Figure 4: The basic setup of a fluorescence microscope. Adapted from Wang and Lai (2021).

2.6. Transmission electron microscopy

Transmission electron microscopy (TEM) is a technique used to visualize specimens at nanometer scales by employing an electron beam instead of photons. Electrons have shorter wavelengths than visible light, which enables TEM to achieve significantly higher resolution than optical microscopy (Lin et al., 2014). This allows for the highest magnification of nanosized structures, making TEM useful for viewing the crystallographic structure, size, and shape of individual NPs (Arenas-Alatorre et al., 2010; Handy et al., 2012).

The TEM instrument consists of an electron gun, a lens system, a sample holder, and a detector. The electron gun has a tungsten filament cathode which is heated to release electrons. These electrons are accelerated towards an anode and directed into the lens system. Magnetic lenses within the lens system focus the electron beam onto a thin specimen (< 100 nm) mounted on a copper grid (Williams & Carter, 2009). Upon interaction with the specimen, some electrons are transmitted while others are scattered or absorbed, depending on the specimen's density and thickness. Notably, electrons encountering low-density areas within the specimen are transmitted through, and these transmitted electrons are ultimately converted to an image of the sample (Williams & Carter, 2009).

The high-resolution visualization of specimens offered by TEM is unparalleled. However, it is not without limitations (Williams & Carter, 2009). One significant constraint is the limited sampling size, allowing only a small portion of the specimen to be studied at a time. Furthermore, three-dimensional objects are projected onto a two-dimensional plane, potentially obscuring valuable information about the specimen's shape. Moreover, the contrast in TEM micrographs depends on the specimen thickness and electron density, lacking depth sensitivity. Thus, micrographs do not provide detailed information about differences at different depths within the specimen. Additionally, specimens should ideally be thinner than 100 nm to ensure electron transparency. However, particles may agglomerate during the preparation of NP suspension samples for TEM imaging, leading to artifacts.

2.7. Dynamic light scattering

Dynamic light scattering (DLS) is an analytical technique used to determine the size distribution and dynamic behavior of particles in suspension. DLS relies on the principle of light scattering and statistical analysis to provide information about the size of particles. A laser is directed onto

a sample containing suspended particles, causing light scattering in multiple directions. DLS then quantifies the intensity of the scattered light at specific angles over time. This intensity fluctuates due to Brownian motion, the random movement of particles in suspension (Stetefeld et al., 2016). Particles experiencing Brownian motion move more rapidly if they are smaller in size, as they encounter less resistance from the surrounding liquid. As a result, light scattering from smaller particles exhibits more rapid intensity fluctuations, whereas larger particles cause slower fluctuations (Hassan et al., 2015). The Zetasizer Nano ZS (Malvern Panalytical) measures the rate of intensity fluctuation and uses correlation analysis to determine the hydrodynamic size of the particles (Malvern Instruments Ltd., 2013).

Additionally, the Zetasizer Nano ZS facilitates measurements of the polydispersity index (PDI), a parameter for the heterogeneity or dispersity of particle size within a sample. PDI is derived by analyzing the width of the particle size distribution obtained through DLS measurements. A narrow size distribution, characterized by a PDI value between 0.1 and 0.7, suggests a more monodisperse sample, promoting suspension stability. Conversely, a broader size distribution, reflected by a PDI value between 0.7 – 1.0, indicates greater variability in particle size, increasing the likelihood of particle settling and instability (Stetefeld et al., 2016). According to the International Organization for Standardization (ISO), a sample is considered monodisperse when its PDI value is below 0.07 (ISO, 2017).

DLS measurements have various limitations, including low sensitivity at lower concentrations and low resolution and non-selective material detection (Bhattacharjee, 2016). Moreover, larger particles or aggregates are more effective at scattering light, which can skew the size distribution. Despite these limitations, DLS is used to validate stock preparations and facilitate comparisons among stock suspensions due to its relatively quick and convenient operational efficiency compared to techniques like TEM analysis.

2.8. Zeta potential measurement

A charged particle in suspension attracts ions of the opposite charge to its charged surface due to Coulomb forces. This leads to the accumulation of ions near the particle surface, forming an electrical double layer comprised of the Stern layer and the diffuse layer (Figure 5). The Stern layer consists of ions strongly attracted, thereby tightly bound, to the particle surface. In contrast, the diffuse layer contains ions more loosely bound to the particle surface and therefore exhibits higher mobility. These ions are distributed more widely in the solution surrounding the

particle. The slipping plane is a hypothetical boundary in the diffuse layer. Ions within this boundary will travel along with the particle as it moves through the solution, while any ions outside this boundary remain immobile (Bhattacharjee, 2016; Malvern Instruments Ltd., 2013).

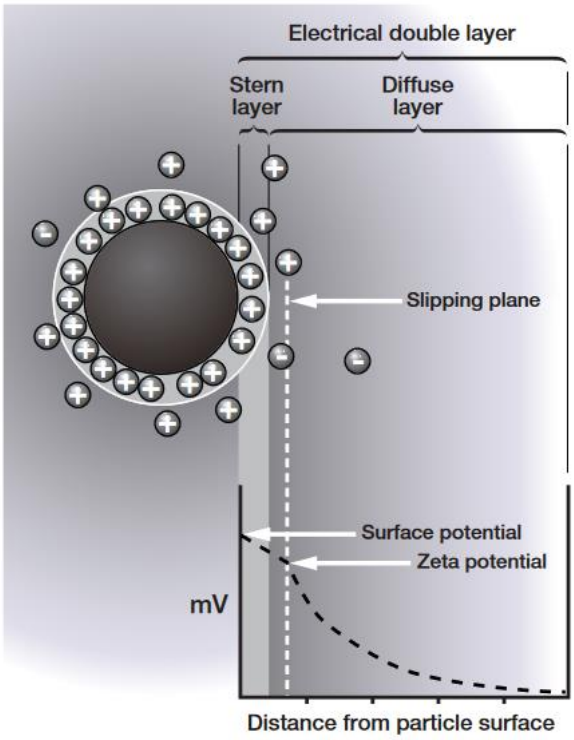

Figure 5: The electrical double layer surrounding a charged particle. Adapted from Malvern Instruments (2013).

Zeta potential is the electrical potential at the slipping plane of a particle and serves as an indicator of suspension stability. The Zetasizer Nano ZS uses laser doppler velocimetry to determine the zeta potential of suspended particles (Malvern Instruments Ltd., 2013). When an electric field is applied to the suspension, charged particles migrate towards oppositely charged electrodes. A laser is directed onto the sample, inducing light scattering. The scattered light exhibits a different frequency than the original laser, resulting in a frequency shift known as the Doppler shift (Bhattacharjee, 2016). The Doppler shift is proportional to the velocity of the particles and is used to derive electrophoretic mobility. The obtained electrophoretic mobility is used to calculate the zeta potential by application of the Henry equation:

$$U_E = \frac{2\epsilon z f(Ka)}{3\eta} \qquad (1)$$

where U_E is the electrophoretic mobility, ϵ is the dielectric constant, z is the zeta potential, f(ka) is Henry's function, and η is viscosity.

Particles with a higher absolute zeta potential will repel each other. This decreases the probability of particle agglomeration and enhances suspension stability. Conversely, lower absolute zeta potential indicates an unstable suspension prone to increased particle aggregation. A zeta potential of ± 30 mV is generally chosen to infer particle stability (Clogston & Patri, 2011; Lin et al., 2014). However, zeta potential alone might not be enough to classify suspension stability. According to the DLVO theory, the combination of van der Waals attraction and electric double layer repulsion explains colloidal stability. (Agmo Hernández, 2023; Derjaguin et al., 1987). Therefore, suspension stability can be observed even at zeta potential values between 10 – 15 mV (Bhattacharjee, 2016).

2.9. Inductively coupled plasma mass spectrometry

Assessing the exposure concentration of a substance is crucial for evaluating its toxic effects. Inductively coupled plasma mass spectrometry (ICP-MS) is a precise and highly sensitive method used to determine the chemical composition of a sample. In ICP-MS, a sample is first nebulized and then ionized in a high-temperature plasma, followed by mass analysis of the resulting ions. With its wide dynamic detection range, ICP-MS can simultaneously measure multiple elements (Pröfrock & Prange, 2012; Wilschefski & Baxter, 2019). It excels at detecting trace elements at low concentrations and plays a significant role in qualitative and quantitative analysis (Wilschefski & Baxter, 2019).

Figure 6 illustrates a cross-section of a single quadrupole ICP-MS instrument. Liquid samples undergo nebulization within the sample introduction system, forming a fine aerosol. This aerosol is introduced to the argon plasma at the end of the torch. Here, the high-temperature environment both atomized the sample and ionized constituents, generating ions. These ions are then directed through a series of electrostatic lenses, which focus and direct the ion beam toward the quadrupole mass analyzer. In the mass analyzer, ions are separated based on their mass-to-charge ratio, with the desired analyte ions reaching the mass detector. The number of ions striking the detector every second is counted, providing the measured signal in the units of “counts per second”. These signals are compared against a calibration curve, which is created using data obtained from standard solutions with known concentrations, allowing for the accurate quantification of analyte concentration in the sample.

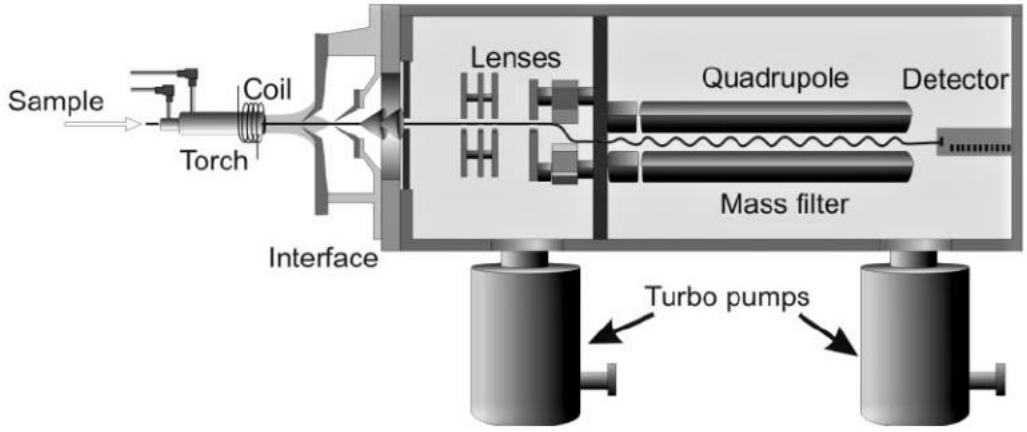

Figure 6: A schematic diagram of the cross-section of a single quadrupole ICP-MS instrument. Adapted from Kosler and Sylverster (2003).

A drawback to the technique is interference, either spectroscopic or non-spectroscopic. Spectroscopic interference occurs when non-analyte ions share the same mass-to-charge ratio as the analyte (Wilschefski & Baxter, 2019). Non-spectroscopic interference refers to influences stemming from the sample matrix or instrumental drift, which can result in analytical error if not appropriately corrected (Wilschefski & Baxter, 2019). The design of a mass spectrometer, particularly the type of mass filter and detection systems used, significantly influences the precision of isotopic measurements attainable (Kosler & Sylvester, 2003). Instruments equipped with triple quadrupole technology, such as the Agilent 8800, have four mass filter in series and offer very high level of interference control (Arenas-Alatorre et al., 2010).

3. Materials and methods

3.1. Nanoparticle suspension

To prepare an NP suspension, 10 mg of CoNPs (QSI-nano cobalt, 3.9 ± 0.8 nm; Quantum Sphere) were weighed and transferred to a 15 mL Falcon tube. The CoNPs were then suspended in MilliQ-water with 0.2% Tween 20 (P1379, Sigma-Aldrich) at a concentration of 1 mg/mL. Tween 20 is a non-ionic surfactant that promotes NP dispersion and suspension stability (Fernando et al., 2019). The NP suspension was vortexed at 3000 rotations per minutes (rpm) (MS3 basic, IKA) for 5 minutes. Next, it was alternately sonicated at 35kHz (Sonorex RK106, Bandelin) for 5 minutes and vortexed for 10 seconds for 1 hour. The suspension was diluted 1:9 in moderately hard reconstituted water (0.44 mM $CaSO_4$, 0.50 mM $MgSO_4$, and 1.14 mM $NaHCO_3$, MHRW) with 0.2% Tween 20. The NP suspension underwent another round of alternate sonication for 5 minutes and vortexing for 10 seconds for 1 hour. To allow for sedimentation of NP agglomerated, the NP suspension was incubated at room temperature without agitation for 24 hours. After the incubation period, 1 mL aliquots were pipetted from the center of the water column. These aliquots were immediately used for characterization and toxicity testing. New NP suspension was prepared before each toxicity test.

3.2. Nanoparticle characterization

TEM was employed to visualize CoNPs and estimate their size. TEM micrographs were taken for CoNPs suspended in two different mediums: MHRW with 0.2% Tween 20 and ethanol. The NP suspension in ethanol was prepared following the protocol described in section 3.3, but 96% ethanol replaced the solvents in all steps. From each of the prepared CoNP suspensions, a 5µL sample was taken from the middle of the water column and individually deposited onto separate 400 mesh carbon copper grids. The grids were left to evaporate overnight covered by a petri dish to minimize contamination. Prior to imaging, the samples underwent plasma exposure for 10 minutes to avoid hydrocarbon contamination. TEM micrographs were taken with a high-resolution TEM (JEM-2100Plus, JEOL) operating at an acceleration voltage of 200 kV.

DLS was used to analyze the size distribution and PDI of the CoNPs in the prepared NP suspension. A 1 mL aliquot of the NP suspension was transferred to a 10 mm square polystyrene

cuvette (DTS0012, Malvern Panalytical), and the cuvette was placed in the sample holder of the Zetasizer Nano ZS for DLS analysis.

The surface charge of the CoNPs was determined by performing zeta potential measurements. 1 mL of the NP suspension was pipetted into a folded capillary zeta cell (DTS10170, Malvern Panalytical). The zeta cell was then placed in the Zetasizer Nano ZS sample holder for zeta potential measurement.

3.3. Cobalt chloride stock solution

A $CoCl_2$ stock solution with a concentration of 0.2 M Co was prepared by weighing out and adding 0.2597 g $CoCl_2$ (232696-5G, Sigma Aldrich) into a 15 mL Falcon tube. MilliQ-water was then added to the tube until the volume reached 10 mL. The solution was thoroughly shaken to ensure complete dissolution of $CoCl_2$.

Subsequently, the stock solution was further diluted to obtain a working stock solution with a concentration of 3201 mg/L Co. To achieve this, 4.076 mL of the 0.2 M Co stock solution was transferred to a new 15 mL Falcon tube, and MilliQ-water was added to reach a total volume of 15 mL. This working stock was utilized for all Co ion exposures and characterizations throughout the project.

3.4. *C. elegans* cultivation

During this project, three different strains of nematodes were used, all of which were obtained from the *Caenorhabditis* Genetic Center, USA. The wildtype N2 strain served as the primary model organism to investigate the effects of Co ion and CoNP exposure on endpoints such as reproduction, growth, and morphological abnormalities. To assess the expression levels of HIF-1, reporter strains ZG120 and ZG444 were used.

Since the toxicity tests were performed in liquid medium, all nematode strains were maintained as liquid cultures. The protocols described below were executed twice a week to ensure healthy and active nematode cultures. All handling of *Escherichia coli* (*E. coli*) and *C. elegans* was carried out under aseptic conditions, by working in a laminar flow cabinet using sterile equipment. Prior to utilization, Erlenmeyer flasks, pipette tips, and liquid media underwent autoclaving.

Preparation of growth medium

The liquid growth medium for *C. elegans* culture consisted of *E. coli* OP50 resuspended in S-base with cholesterol (51 mM NaCl, 1 mM $MgSO_4$, 24 mM KPO_4, 0.13 µM cholesterol). First, a liquid culture of *E. coli* OP50 was prepared by transferring an *E. coli* colony, grown on a streak plate stored at 4°C, into an Erlenmeyer flask with 50 mL of lysogeny broth (10 g/L Tryptone, 5 g/L yeast extract, 10 g/L NaCl). The culture was incubated overnight at 37°C with shaking at 200 rpm to ensure sufficient oxygenation. The following day, the *E. coli* culture was transferred into a 50 mL Falcon tube and centrifuged at 5000 RCF for 10 minutes. This led to the formation of a bacterial pellet, and the supernatant was removed from the tube. Subsequently, the pellet underwent two washes with 50 mL of S-base (51 mM NaCl, 1 mM $MgSO_4$, 24 mM KPO_4) by centrifugation at 5000 RCF for 5 minutes, with the supernatant being discarded after each centrifugation round. Finally, the pellet was resuspended in 50 mL of S-base with cholesterol and transferred to a sterile Erlenmeyer flask.

Preparation of *C. elegans* culture

A three to four day old liquid nematode culture was checked using a stereo microscope (M205C, Leica) to ensure healthy nematodes. Following the assessment, 1 mL of the *C. elegans* culture was transferred to 50 mL of the freshly prepared growth medium. The culture was stored in the dark at 20°C with gentle shaking (125 rpm). After an incubation period of three days, the nematode culture had a sufficient number of gravid nematodes and was deemed ready for bleaching.

Age synchronization

The day before an exposure experiment the *C. elegans* liquid culture was treated with alkaline hypochlorite to obtain an age-synchronized population of nematodes. Prior to alkaline hypochlorite treatment, the culture was assessed under a stereo microscope to ensure an active culture with sufficient gravid nematodes. Depending on the density of mature nematodes, 5-15 mL of the culture was transferred from the Erlenmeyer flask into a 50 mL Falcon tube. The nematodes were allowed to settle at the bottom of the tube before most of the supernatant was removed, leaving 3.5 mL in the tube. The volume was then adjusted to 15 mL with S-base, and again the nematodes were left to settle at the bottom of the tube before the supernatant was removed down to 3.5 mL. The washing with S-base was repeated thrice, ensuring a visible nematode pellet at the bottom of the Falcon tube.

1.5 mL of alkaline hypochlorite solution (500 µL sodium hypochlorite (425044, Honeywell), 500 µL NaOH 5 M, 500 µL ddH_2O) was added to the Falcon tube with the washed nematodes.

A combination of vigorously shaking and resuspending the content of the tube with a pipette was employed to aid in nematode dissolution. This enhances collision frequency, thereby increasing the reaction rate and promoting more effective dissolution of nematodes. The presence of eggshells makes eggs more resistant to alkaline hypochlorite. After 5 minutes, the nematodes were frequently checked by a stereo microscope to ensure that only free eggs were left, with no intact adults or debris.

To neutralize alkaline hypochlorite, 15 mL of M9 (22 mM KH_2PO_4, 42 mM Na_2HPO_4, 86 mM NaCl, 1 mM $MgSO_4$) was added to the Falcon tube, immediately followed by centrifugation at 1500 RCF for 1 minute. The supernatant was then carefully removed, and the egg pellet was washed with another 15 mL of M9. The tube was centrifuged at 1500 RCF for 2 minutes before the supernatant was removed. The washing process was repeated 3-4 times to ensure thorough removal of alkaline hypochlorite solution.

After the final centrifugation and removal of the supernatant, the egg pellet was resuspended with 2 mL of M9. Using pipette tips that have been conditioned with S-base containing 0.2% Tween 20, the entire volume of the Falcon tube was transferred to a sterile glass beaker. An additional 2 mL of M9 was added to the Falcon tube and transferred to the glass beaker, ensuring the transfer of any eggs that might have adhered to the walls of the tube. A representative sample of the egg culture was assessed using a stereo microscope. The glass beaker containing the egg culture was then covered with Parafilm punctured with holes and then incubated in the dark overnight at 20° C with gentle shaking (75 rpm). Overnight, the eggs hatched at different times, but the absence of food caused the hatched L1 stage nematodes to arrest their development, ensuring that the L1 stage nematodes were age-synchronized at the beginning of a toxicity test.

3.5. Toxicity tests

During this project, both chronic (96h and 72h) and acute (24h) toxicity tests were performed on the nematode strains. An overview of the performed toxicity tests is presented in Table 1. The chronic toxicity tests adhered to the International Organization for Standardization (ISO) 10872-2020 standard for water quality, with some modifications (ISO, 2020). Notably, MHRW with 0.2% Tween 20 was used as the test medium, as it is more suitable in assessing NP toxicity. Tween 20 is non-hazardous and does not influence toxicological assessment. All toxicity tests were conducted in sterile 24-well cell culture plates. Each concentration was tested in triplicate wells, and the control was performed in three replicates per plate.

Table 1: An overview of the toxicity tests conducted during this project.

Test	Strain	Exposure type
E1	N2	96h chronic exposure
E2*	N2	72h chronic exposure
E3	N2	24h acute exposure
E4	ZG444	72h chronic exposure
E5	ZG444	24h acute exposure
E6	ZG120	24h acute exposure

* E2 was performed twice. Round 1 provided samples to determine Co exposure concentrations, while round 2 resulted in micrographs used to study the toxic effects of chronic exposure. In this thesis, "E2" refers to the second round of 72h chronic toxicity test performed on N2 nematodes, unless stated otherwise.

96-hour chronic toxicity test

For E1, N2 nematodes were exposed to $CoCl_2$ and CoNPs separately in distinct 24-well cell culture plates. On the $CoCl_2$ toxicity test plate, each well had 1 mL of *E. coli* resuspended in MHRW with 0.2% Tween 20. The *E. coli* for the toxicity tests was prepared according to the protocol described in 3.4, with some adjustments. The bacterial pellet underwent two washes with MHRW instead of S-base. Following the final centrifugation, the pellet was resuspended in 50 mL MHRW with 0.2% Tween 20. For wells designated with the highest $CoCl_2$ concentration, an additional 0.99 mL of *E. coli* resuspended in MHRW with 0.2% Tween 20 was added. $CoCl_2$ toxicity was tested in the range of 0.22 – 16 mg/L, with seven concentrations. For the highest concentration, 10 µL from the $CoCl_2$ working stock solution with concentration of 3201 mg/L Co was added to the well with 1.99 mL *E. coli*, to obtain a nominal concentration of 16 mg/L in the highest exposure. A two-fold dilution series was performed until the lowest nominal concentration of 0.25 mg/L Co was obtained.

Six concentrations were included in the CoNP toxicity test. Each well, except those designated for the highest CoNP concentration, received 1 mL of *E. coli* resuspended in MHRW with 0.2% Tween 20. In the wells with the highest concentration, 1 mL of a 2x concentrated *E. coli* culture was added. This concentrated culture was prepared by resuspending the *E. coli* pellet in only 25 mL MHRW with 0.2% Tween 20 after washing the pellet with MHRW. Then, 1 mL of NP suspension was added from the center of the water column to these wells. Following the same procedure as the $CoCl_2$ toxicity test, a two-fold dilution series was performed across the plate.

The L1 stage *C. elegans* larvae were checked using a stereo microscope to ensure a healthy culture and count the number of larvae in 30 µL of the culture. Three 10 µL droplets were examined, each containing 8-12 larvae. Since the aim during E1 was to add around 10 nematodes per well, 10 µL of the L1 stage *C. elegans* culture was added to each well, including the control wells. To ensure a homogenous culture, the glass beaker containing L1 stage nematodes was swirled each time 10 µL was pipetted out of the beaker. The plates were covered with lids and stored in the dark at 20°C, with gentle shaking (75 rpm). After 96 hours, the toxicity test was terminated by the addition of 300 µL Rose Bengal (300 mg/L) to all wells. The plates were then placed in an 80°C oven for 10 minutes. The plates were then stored at 4°C until the measurement of endpoints, which was completed within six weeks.

72-hour chronic toxicity test

72-hour chronic toxicity tests (E2 and E4) were performed to assess adult nematodes before they produced a new generation of L1 stage nematodes. The tests were conducted on both the N2 and ZG444 strains, separately. Furthermore, the $CoCl_2$ and CoNP toxicity tests were carried out sequentially, rather than simultaneously, to allow sufficient time for microscopy and imaging of at least 10 nematodes per exposure concentration. The protocol for the 72-hour chronic toxicity tests followed a similar procedure as described for the 96-hour chronic toxicity test. Six concentrations were included for both $CoCl_2$ and CoNP toxicity tests. To ensure an adequate number of nematodes to study under a light microscope (DM6 B, Leica), approximately 25-30 nematodes were aimed to be added to each well. Depending on the density of the L1 stage *C. elegans* culture, the volume of larvae culture added to each well varied between 10-30 µL for each toxicity test. After the addition of nematodes to all wells, the plates were incubated in the dark at 20°C with gentle shaking (75 rpm) for 72 hours.

Please note that E2 was performed on 2 separate occasions since a low volume of the L1 stage culture was added to each well during the first round. This resulted in an insufficient number of N2 nematodes for microscopic study. 150 µL samples were collected during the first round to determine Co exposure concentration. In the second round, a satisfactory number of nematodes were obtained for each exposure concentration, ensuring representative imaging. However, no samples were taken for Co concentration analysis. In this thesis, "E2" refers to the second round of 72h chronic toxicity test performed on N2 nematodes, unless stated otherwise.

24-hour acute toxicity test

24-hour acute toxicity tests were individually performed for all three strains of nematodes (E3, E5, and E6). To minimize the effect of *C. elegans* developmental stage on the hypoxic response,

L1 stage nematodes were cultured for 48 hours under control condition before undergoing a 24-hour acute exposure to either $CoCl_2$ or CONP. After hatching overnight, the L1 stage culture was transferred from the glass beaker to an Erlenmeyer flask with 25 mL *E. coli* resuspended in S-base with cholesterol. The flask was incubated in the dark at 20°C with gentle shaking (125 rpm) for 48 hours. The access to *E. coli* caused the arrested L1 stage nematodes to resume development, which after 48 hours had developed into L4 stage nematodes.

After 48 hours of development, the L4 stage nematodes were separated from *E. coli* by a 15 µm pore size filter. While the liquid *E. coli* passed through the filter, the nematodes were retained on top. The nematodes were washed by adding 5-10 mL of S-base on top of the filter. After a couple of rounds of washing, the filter was turned upside down on a clean 50 mL Falcon tube, so the filter surface with the L4 stage nematodes faced towards the bottom of the tube. Then, 5 mL of S-base was added to the filter, so the nematodes released the filter surface and dropped into the tube.

The acute toxicity test performed on N2 (E4) used three exposure concentrations for $CoCl_2$, ranging from 3.30 mg/L to 13.3 mg/L Co, and three exposure concentrations for CoNPs, ranging from 1.36 mg/L to 5.55 mg/L Co. ZG120 nematodes (E6) were examined for four exposure concentrations for $CoCl_2$, ranging from 1.67 mg/L to 13.3 mg/L Co, and three exposure concentrations for CoNPs, ranging from 1.36 mg/L to 5.55 mg/L. For each strain, both $CoCl_2$ and CoNP exposures were conducted on the same 24-well cell culture plate, with triplicates for the control. During E5, ZG444 nematodes were exposed to a single of $CoCl_2$, CoNP, and paraquat. The nematodes were exposed to 4 mM paraquat, included as a positive control to investigate whether exposure to $CoCl_2$ at 3.30 mg/L Co and CoNPs at 5.55 mg/L Co induces activation of *nhr-57* gene (Padmanabha et al., 2015). This toxicity test was also conducted on a single 24-well cell culture plate, with triplicates included for the control.

The preparation of the *E. coli* suspension and the two-fold dilution series of $CoCl_2$ and CoNPs followed the same procedure as for the chronic toxicity tests. For the paraquat exposure during E5, 1.2 mL of the concentrated *E. coli* suspension was added to a well. Subsequently, 0.8 mL from a 10 mM paraquat solution was added to the same well, achieving a paraquat concentration of 4 mM. After thorough homogenization with a pipette, 1 ml of the well content was discarded.

The density of the washed L4 stage culture was examined by counting the number of nematodes per 10 µL droplet, using a stereo microscope. As for the 72-hour chronic toxicity tests, approximately 25-30 nematodes were aimed to be added to each well. The 24-well cell culture

plates, one each *C. elegans* strain, were then incubated in the dark at 20°C with gentle shaking (75 rpm) for 24 hours.

3.6. Toxicity assessment

96-hour chronic toxicity

After the termination of the N2 96-hour toxicity test, several endpoints were assessed within six weeks. Survival, growth, and reproduction were assessed using a stereo microscope (M205C, Leica) equipped with a camera (MC170 HD, Leica). Nematode growth was determined by measuring their length with the Leica Application Suite software (LAS v.4.9). Reproduction was determined by calculating the ratio of offspring to adult nematodes in each well. The number of offspring and adults in each well was counted using a handheld tally counter.

In vivo optical microscopy

For the other toxicity tests (E2 – E6), in vivo micrographs were captured by using a fluorescent light microscope (DM6 B, Leica) equipped with a camera (DMC 4500, Leica). Following the incubation period, either 72 or 24 hours, the content of the wells was transferred to 15 mL Falcon tubes. The supernatant from each tube was carefully removed after letting the nematodes settle at the bottom. The nematodes were washed twice with 1-2 mL MHRW, and the supernatant was removed after each wash. Following the final wash, 1 mL MHRW was added to each Falcon tube to prevent nematode dehydration.

During microscopy, only microscope slides coated with a thin layer of agarose were used. A 100 µL droplet of melted 2% agarose was added on top of a microscope slide and streaked along its length to achieve a uniform layer of agarose on its surface. After developing for 72 hours, the nematodes are heavily gravid and prone to bursting under the pressure of a cover slip. The presence of an agarose layer on the microscope slide minimized the risk of nematodes bursting during microscopy. A 10 µL droplet was taken from the washed nematodes and added to a microscope side with an agarose layer. The nematodes were anesthetized by adding 10 µL 30 mM sodium azide (NaN_3) on top of the nematode droplet. After letting NaN_3 work for a minute, a cover slip was carefully placed on top of the nematode sample.

To assess morphological changes following $CoCl_2$ or CoNP exposure, phase contrast images of exposed N2 nematodes were captured in vivo. The hypoxia response resulting from exposure

to CoCl2 and CoNPs was investigated by imaging exposed ZG120 and ZG444 nematodes in vivo using a fluorescence microscope. The aim was to capture images of approximately 10 nematodes from each exposure concentration, with images taken at 10x and 20x magnification.

The GFP signal from ZG120 and ZG444 strains was measured using a 450-490 nm excitation and 500-550 nm emission filter cube. To ensure comparable and unbiased measurements, consistent settings for exposure and gain were maintained across all concentrations, including the control. The fluorescence signal was quantified using the image analysis software ImageJ, by measuring pixel-based average intensity. The average fluorescence intensity for each nematode was normalized to the relative size of the nematode. The brightness and contrast in some of the fluorescence micrographs presented in this thesis were adjusted to enhance image visibility. The adjustments were made uniformly across all nematodes within the same toxicity test to maintain comparability.

3.7. Characterization of cobalt concentration

Total Co concentration during toxicity tests

To determine the exposure Co concentrations during the 96-hour chronic toxicity test, a 150 µL sample was taken from every well at T-0, before nematode addition. Similar samples were also taken at T-0 of the first round of E2. Each sample was mixed with 1.5 mL ultrapure HNO_3 and incubated at 90°C for 2 hours. Subsequently, the samples were diluted to 15 mL with Milliwater, resulting in a 10% acid concentration. Following the digestion and dilution, the samples were ready to be analyzed by ICP-MS.

Fractionation

Fractionation was performed to investigate the dynamics and behavior of Co ions and CoNPs. This included low, medium, and high Co concentrations, as well as control groups for both $CoCl_2$ and CoNP exposure. Aggregated, suspended, and low molecular mass (LMM) Co fractions were investigated at the beginning (T-0) and the end (96h) of the exposure period. This allowed for the determination of whether different fractions of Co underwent transformation during the exposure. To evaluate the influence of bacterial presence on the fraction transformation, fractionation was conducted both with and without *E. coli* present during the exposure. The fractionation was immediately performed at T-0 and 96h to prevent further Co agglomeration and dissolution. It is important to note that the fractionation samples of CoNPs

at T-0 and 96h were not taken from the same NP suspension, but rather individual NP suspensions.

For each 1 mL replicate, 100 µL was extracted for ICP-MS measurement of the total Co concentration. The remaining 900 µL from each replicate were transferred to their corresponding labeled Eppendorf tubes and centrifuged at 2000 RCF for 5 minutes. Following centrifugation, 100 µL of the supernatant was extracted for ICP-MS measurement of suspended Co concentration. To obtain the LMM fractions, 3 kDa Millipore Centrifugal filters (Amicon, Millipore) were pre-conditioned with 200 µL of the remaining supernatant and centrifuged for 14000 RCF for 15 minutes. After centrifugation, the now preconditioned filters were transferred to clean Eppendorf tubes. 400 µL of the supernatant from the initial centrifugation at 2000 RCF was added to the filters and centrifuged at 14000 RCF for 30 minutes. The filters were then removed from the Eppendorf tubes, and 100 µL of each filtrate was collected for ICP-MS measurement of LMM Co concentration.

Prior to measuring Co concentration using ICP-MS, the collected 100 µL samples underwent digestion and dilution. Each sample was mixed with 1.5 mL ultrapure HNO_3 and was incubated at 90° C for 2 hours. Subsequently, the samples were diluted to 15 mL with MilliQ-water, resulting in a 10% acid concentration.

ICP-MS measurement

The Co concentration in the samples was measured using a triple quadrupole ICP-MS (8800, Agilent Technologies) in helium mode. The samples were placed in an autosampler which was connected to the ICP-MS. The calibration curve was made using a calibration blank and 3 standard solutions with Co concentrations of 2 µg/L, 20 µg/L, and 200 µg/L, respectively. Drift checks were performed by analyzing the 20 µg/L Co standard solution after every 15th sample. This allowed for the correction of any drift and ensured the accuracy of the analytical results. Rhodium served as an online standard and was introduced into the ICP-MS instrument along with the samples to control the accuracy of the measurements. The limit of detection (LOD) and limit of quantification (LOQ) were determined as 3x and 10x the standard deviation in the control samples respectively.

3.8. Statistical analysis

Statistical analysis was performed using R (version 4.3.2). A one-way analysis of variance (ANOVA) was performed to check for statistically significant differences between groups. In instances where such differences were detected, a post-hoc Tukey's Honest Significant Difference (HSD) test was employed to check for significant differences between all group combinations. Differences were considered statistically significant for p-values lower than 0.05. JMP Trail (17.2.0) was used to fit dose-response curves and predict EC50 values, which were obtained by Probit 4P as four parameters logistic regression model and relative inverse prediction curves.

3.9. Language correction

The language correction AI tools ChatGPT 3.5 and Microsoft Copilot were used during the refinement process of this thesis. Please note that these AI tools were not used as text generators, but rather for reviewing and refining the language.

4. Results

4.1. Nanoparticle characterization

TEM micrographs of CoNPs were taken of NPs suspended in different media: MHRW with 0.2% Tween 20 and 96% ethanol. Images of CoNPs suspended in ethanol are presented in Figure 7. This selection was made due to the superior visibility of CoNPs in ethanol, possibly due to the presence of salts in MHRW interfering with the visibility of the NPs in the images.

TEM analysis indicated a high degree of aggregation (Figure 7A) of the NPs in suspensions used throughout this project. High-resolution TEM (HRTEM) micrographs (Figures 7B and 7C) revealed the crystalline structure of the NPs, as evidenced by the observed fringes. Individual NPs in our suspension had a diameter of less than 10 nm.

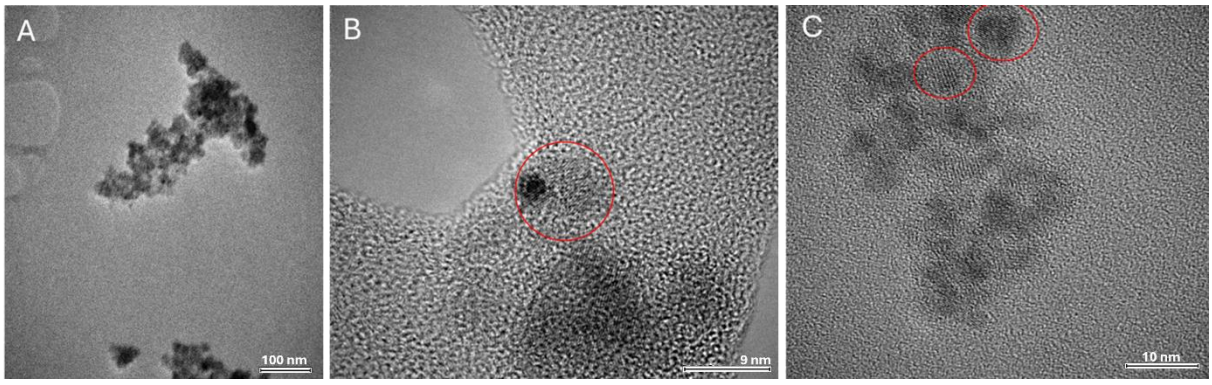

Figure 7: TEM micrographs of the CoNPs suspended in 96% ethanol. Bright-field TEM image (A) reveals a high degree of aggregation of the NPs on the TEM grid. HRTEM micrographs (B) show the crystallinity of particles (highlighted with red circles).

Measurements of size distribution, PDI, and zeta potential of the CoNPs in MHRW with 0.2% Tween 20 were conducted immediately following the 24-hour equilibration, coordinated to coincide with the start (T-0) of the exposure E1. The average hydrodynamic diameter of the NPs was determined to be 155.7 ± 0.8 nm (triplicate measurement of 10 runs each). The size distribution (Figure 8) showed that the majority of NPs fell within the size range of 40-1000 nm, and a small fraction ranged from 2000 to 6000 nm. The PDI was measured to be 0.362 ± 0.011. Additionally, the NP suspension showed a zeta potential of -16.2 ± 0.3 mV.

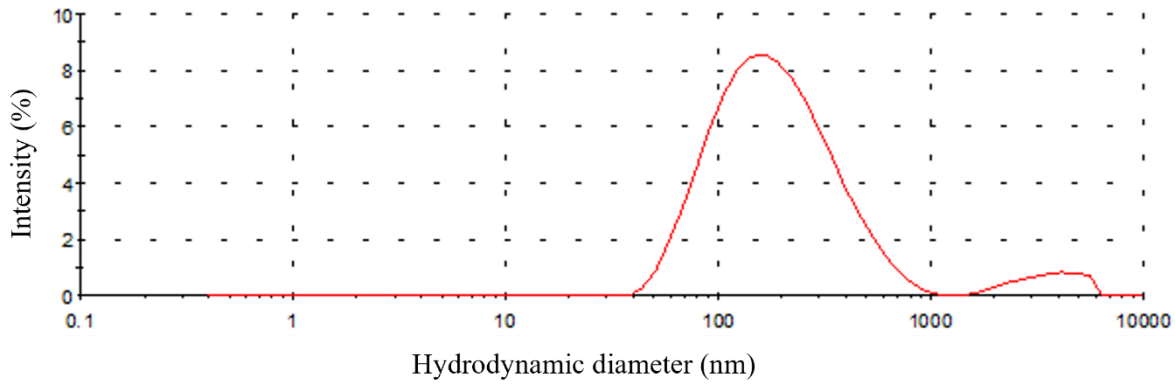

Figure 8: Average particle size distribution (nm) of CoNPs in MHRW with 0.2% Tween 20, derived from triplicate measurements of 10 runs each. The graph is adapted from the Malvern Zetasizer software.

4.2. Exposure concentrations

The $CoCl_2$ working stock solution, Co concentration of 3201 mg/L, was employed for all $CoCl_2$ exposures throughout this project, while new NP suspensions were prepared 24 hours prior to each exposure. The total Co exposure concentrations in each triplicate of exposure wells were determined through ICP-MS analysis. Samples from all exposure concentrations were taken at T-0 during E1, while samples of selected exposure concentrations (low, medium, and high) were taken at T-0 from the first round of E2 and fractionation. The Co exposure concentrations are presented in Table 2. The determined Co exposure concentrations from E1 were used to evaluate the effects observed following the 96h chronic toxicity test. Mean Co concentrations presented in Table 2 were employed for assessing morphological effects and hypoxic responses observed following the other tests, as exposure concentration at T-0 was not determined for these tests.

Table 2: Total Co exposure concentration (mean ± standard deviation) in $CoCl_2$ and CoNP exposures, determined through ICP-MS analysis.

Exposure	Dilution factor	Nominal * Co concentration (mg/L)	Mean Co concentration (mg/L) 96h chronic exposure	Mean Co concentration (mg/L) in E1, E2 and E3
$CoCl_2$	64x	0.25	0.23 ± 0.014	0.23 ± 0.014
	32x	0.50	0.40 ± 0.008	0.40 ± 0.035
	16x	1.00	0.86 ± 0.030	0.85 ± 0.062
	8x	2.00	1.70 ± 0.057	1.67 ± 0.125
	4x	4.00	3.44 ± 0.092	3.30 ± 0.321
	2x	8.00	6.94 ± 0.346	6.94 ± 0.346
	1x	16.0	13.4 ± 0.909	13.3 ± 1.582
CoNP	32x		0.22 ± 0.028	0.17 ± 0.055
	16x		0.43 ± 0.040	0.43 ± 0.040
	8x		0.92 ± 0.044	0.92 ± 0.044
	4x		1.80 ± 0.032	1.36 ± 0.482
	2x		3.56 ± 0.297	3.22 ± 0.428
	1x		6.95 ± 0.229	5.55 ± 1.394

* It was not possible to predict a nominal Co concentrations of CoNP suspension used for toxicity tests ans characterization, as it was unknown how big fraction of the 10 mg QSI-nano cobalt would be in the suspended solution following the 24h incubation period.

The degree of aggregation and ion leaching was determined by size fractionation and ICP-MS analysis at T-0 and 96h. The fractionation analysis of $CoCl_2$ and CoNP in exposure media with *E. coli* revealed notable differences. At T-0, $CoCl_2$ predominantly existed as LMM species, comprising over 70% of the total concentration at T-0. In contrast, over half of CoNP species were aggregated particles at the start of exposure (Figure 9A). Over the 96-hour period, the proportion of LMM species in $CoCl_2$ exposure decreased, while the aggregated fraction increased to approximately 50% of $CoCl_2$ species. For the CoNP exposure, the proportion of aggregated particles stayed relatively stable, while there was an increase in the suspended fraction and an equal decrease in the LMM fraction. At 96h, CoNP consisted of approximately 50% aggregated species, 45% suspended species, and 5% LMM species (Figure 9B).

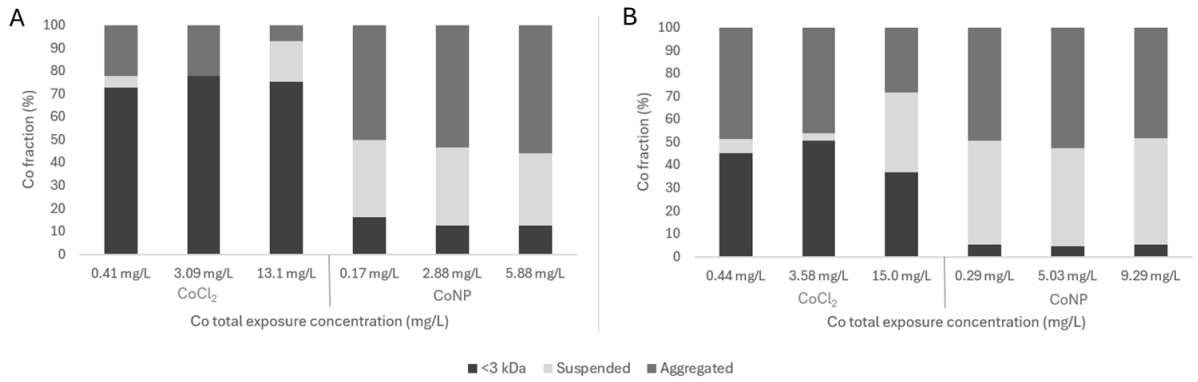

Figure 9: Size fractionation analysis of Co speciation with the presence of E. coli in the media at T-0 (A) and 96h (B). The data represents an average of triplicate measurements.

Similarly, a fractionation analysis was performed without *E. coli* in the exposure media, to evaluate the influence of bacteria on the transformation of CoNPs and $CoCl_2$. At T-0, $CoCl_2$ predominantly existed as LMM species, accounting for over 90% of the Co concentration in the 0.44 mg/L and 3.44 mg/L exposure concentrations (Figure 10A). The lowest exposure concentration (0.44 mg/L at T-0 and 0.36 mg/L at 96h) experienced a slight decrease from 97% to 80% over the 96-hour period, while the LMM fractions in the other exposure concentrations decreased significantly. The $CoCl_2$ suspended species, which comprised only a small fraction at T-0, increased to approximately 90% and 70% for the 2.98 mg/L and 13.3 mg/L exposures, respectively (Figure 10B). The CoNP suspension at T-0 consisted of approximately 25% LMM species, 30% suspended species, and 45% aggregated species (Figure 10A). The LMM fraction decreased to around 10% over the 96-hour period, while an increase in the aggregated fraction was observed across all exposure concentrations.

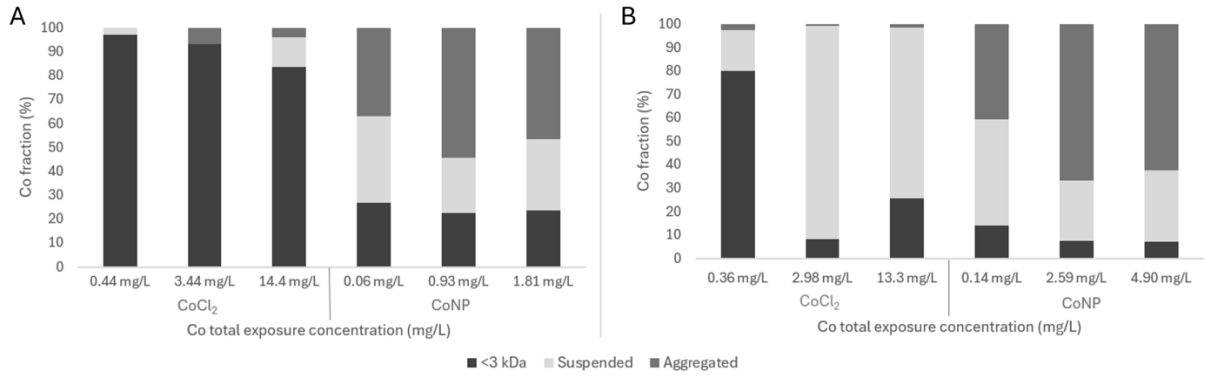

Figure 10: Size fractionation analysis of Co speciation with the presence of E. coli in the media at T-0 (A) and 96h (B). The data represents an average of triplicate measurements.

Both fractionation analyses show a consistent pattern in the described trends across different CoNP exposure concentrations, while variations were observed in the trends for $CoCl_2$ exposure concentrations.

4.3 Toxicity

The toxicity of both $CoCl_2$ and CoNPs was assessed through 96-hour chronic exposure spanning a wide range of concentrations (Table 2). Notably, no survivors were observed in the 6.94 mg/L and 13.4 mg/L exposure concentrations of $CoCl_2$, while nematodes survived in all CoNP exposure concentrations. The dose-response relationship was assessed between exposure and the following toxicological endpoints: total body length and reproduction.

Growth

The total body length of adult nematodes was used as an endpoint to assess the effect of $CoCl_2$ and CoNP exposure on growth and development. ANOVA tests indicated statistically significant differences between the average body length of control and exposed nematodes for both $CoCl_2$ and CoNP exposures. Tukey's HSD test indicated a statistically significant difference between the control nematodes and those exposed to 1.70 mg/L and 3.44 mg/L Co during chronic exposure to $CoCl_2$ (Figure 11A). Similarly, a statistically significant effect on growth was observed at a Co concentration of 6.95 mg/L for CoNP exposure (Figure 11B).

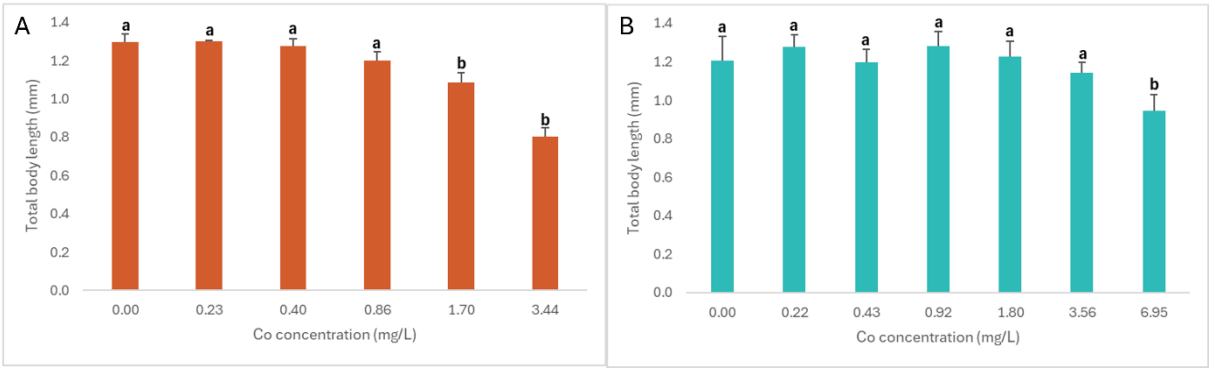

Figure 11: Mean length and standard deviation at each exposure concentration. Statistically significant differences, detected by Tukey's HSD tests, in total body length between the control and exposed nematodes are marked with "b" above the corresponding bar.

Linear regression analysis was conducted to evaluate the correlation between total Co exposure concentration and the observed reduction in growth (Figure 12). The finding revealed a strong

correlation between $CoCl_2$ exposure and growth reduction, with a more than 40% reduction caused when exposed to 3.44 mg/L. In contrast, the correlation was comparatively weaker for CoNP exposure, as indicated by an R^2 value of 0.61 suggesting a moderate correlation. Nematodes showed almost 30% reduction in body length when exposed to CoNPs at 6.95 mg/L Co.

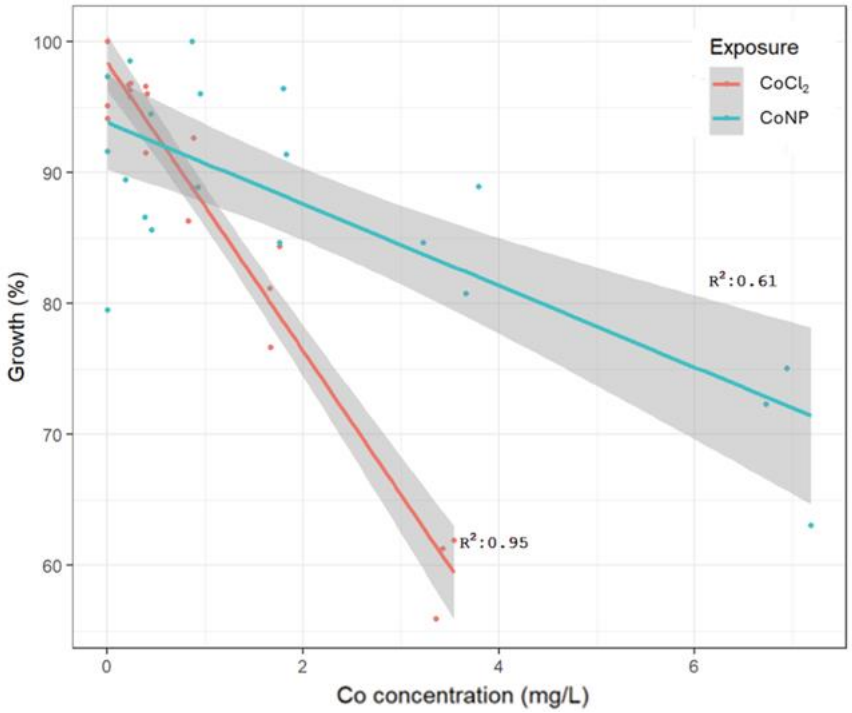

Figure 12: Linear regressions for growth in *C. elegans* exposed to increasing total concentrations of $CoCl_2$ and CoNPs. Growth data was normalized to the mean growth of nematodes in the control group. The confidence intervals for each linear regression are depicted as a grey area.

Linear regression analyses were also performed to assess the impact of LMM species on the reduction in adult nematode body length. In the presence of *E. coli* in the exposure media, LMM species heightened the correlation between exposure concentration and growth reduction for both $CoCl_2$ and CoNPs (Figure 13). Notably, the LMM species in CoNP exposure induced greater inhibition of growth compared to an equivalent concentration of LMM species in $CoCl_2$. At 96h, the correlation between LMM species concentration and growth inhibition was further intensified, as indicated by an increased R^2 value.

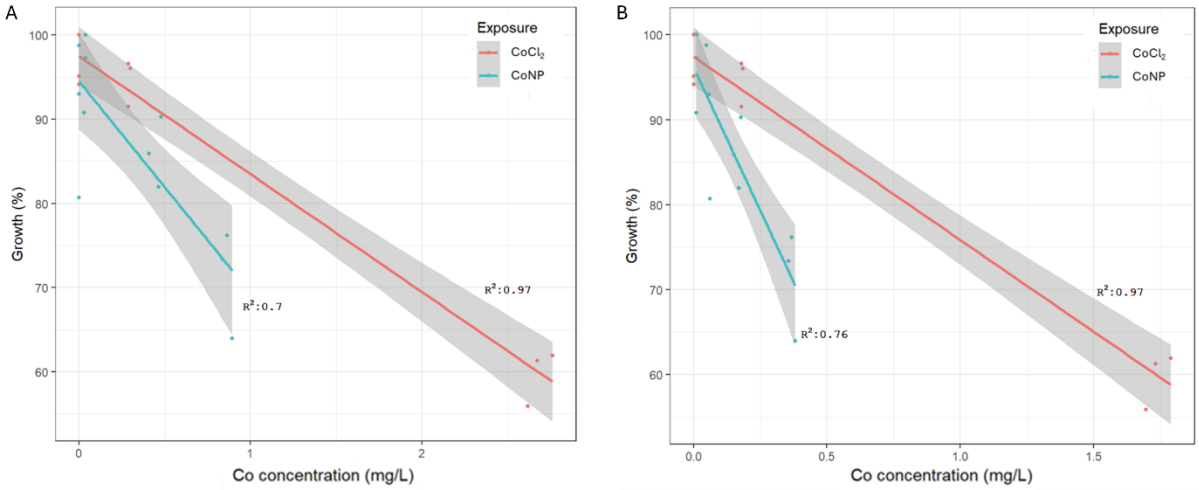

Figure 13: Linear regressions for the effect of LMM species $CoCl_2$ and CoNPs on growth in *C. elegans* at T-0 (A) and 96h (B) with *E. coli* in the exposure media. Growth data was normalized to the mean growth of nematodes in the control group. The confidence intervals for each linear regression are depicted as a grey area.

Correlation analysis of LMM species fraction from MHRW without E. coli revealed a heightened correlation between exposure concentration and growth reduction at T-0 (Figure 14A). At 96h, a moderate correlation was observed between exposure to LMM species in CoNPs and growth inhibition, while a weak correlation for exposure to LMM species in $CoCl_2$ exposure (Figure 14B). Notably, at both T-0 and 96h, the confidence intervals of $CoCl_2$ and CoNP exposures overlap.

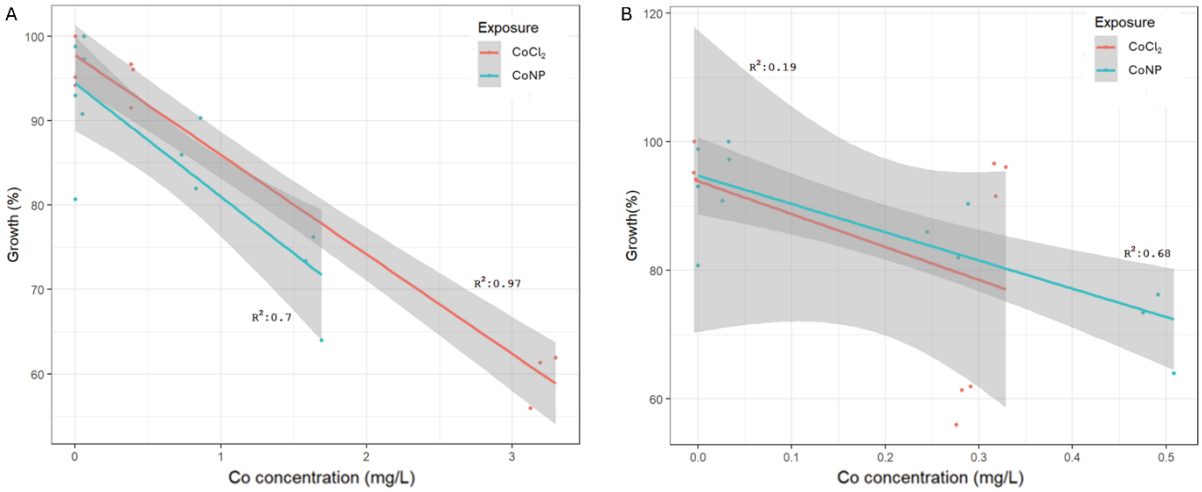

Figure 14: Linear regressions for the effect of LMM species $CoCl_2$ and CoNPs on growth in *C. elegans* from at T-0 (A) and 96h (B) without *E. coli* in the exposure media. Growth data was normalized to the mean growth of nematodes in the control group. The confidence intervals for each linear regression are depicted as a grey area.

Reproduction

Reproduction was determined by calculating the ratio of offspring to adult nematodes in each well. For the CoCl2 exposure concentrations with survivors, no offspring were observed at 3.44 mg/L Co. For CoNP exposure, offspring were detected at all exposure concentrations. ANOVA tests indicated statistically significant differences between the reproduction of control and exposed nematodes for both $CoCl_2$ and CoNP exposures. Tukey's HSD test indicated a statistically significant reduction between the control nematodes and those exposed to 1.70 mg/L and 3.44 mg/L Co during chronic exposure to $CoCl_2$ (Figure 15A). Similarly, a statistically significant reduction of growth was observed at a Co concentration of 3.56 mg/L and 6.95 mg/L for CoNP exposure (Figure 15B).

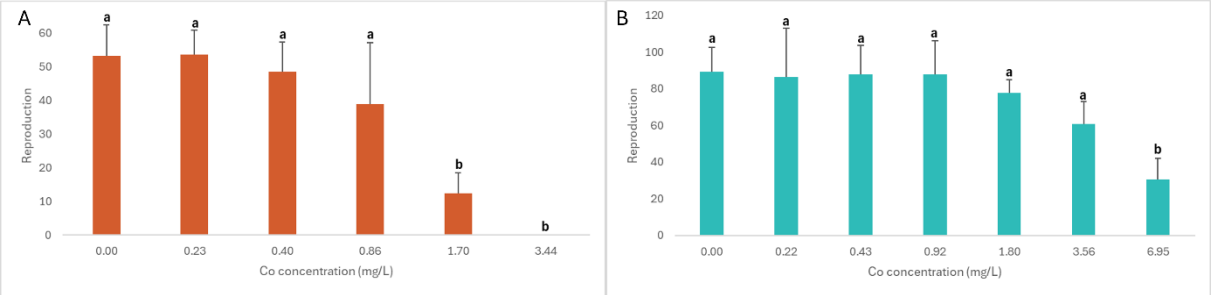

Figure 15: Mean reproduction and standard deviation at each exposure concentration. Statistically significant differences, detected by Tukey's HSD tests, in reproduction between the control and exposed nematodes are marked with "b" above the corresponding bar.

To assess a dose-response relationship between Co concentration and reproduction, both linear regression (Figure 16A) and probit logistic regression analyses (Figure 16B) were conducted. The findings revealed a strong correlation between reproduction and exposure concentration for both $CoCl_2$ and CoNPs. EC_{50} for nematode reproduction exposed to $CoCl_2$ was predicted to be 1.09 mg/L, while reproduction EC_{50} for CoNP exposed nematodes was predicted to be 4.44 mg/L.

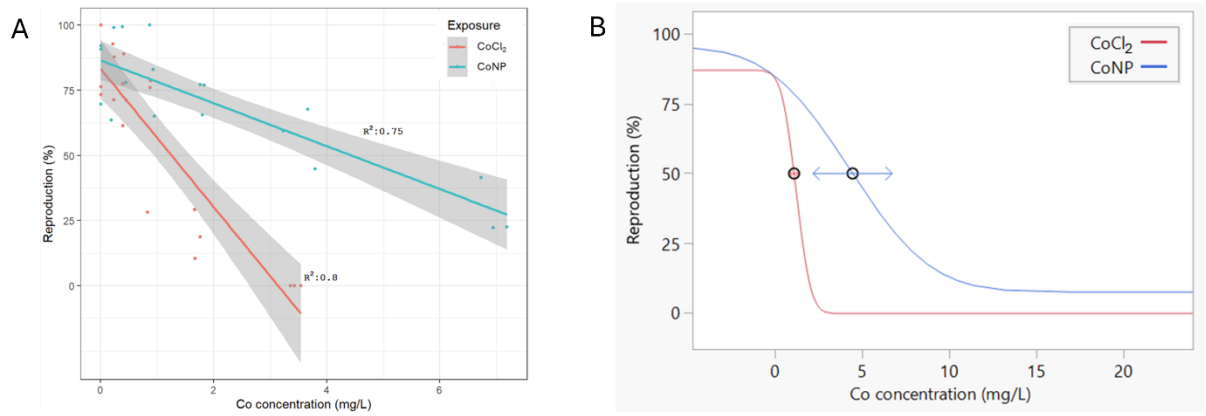

Figure 16: Linear regression analysis (A) and Probit 4P logistic regression analysis (B) for reproduction in C. *elegans* exposed to increasing total concentrations of $CoCl_2$ and CoNPs. Reproduction data was normalized to the mean reproduction of nematodes in the control group. The confidence intervals for each linear regression are depicted as a grey area (A), while confidence intervals for the logistic regression are depicted with arrows (B).

The effect of LMM species on reproduction was assessed by performing linear regression and Probit logistic regression analyses. In the presence of *E. coli*, the correlation between reproduction and LMM species from $CoCl_2$ increased compared to total Co concentration, while the correlation stayed equally strong for LMM species of CoNPs (Figure 17A). The linear regressions at 96h show that LMM species in both exposures induce reproduction effects at lower Co concentrations (Figure 17B).

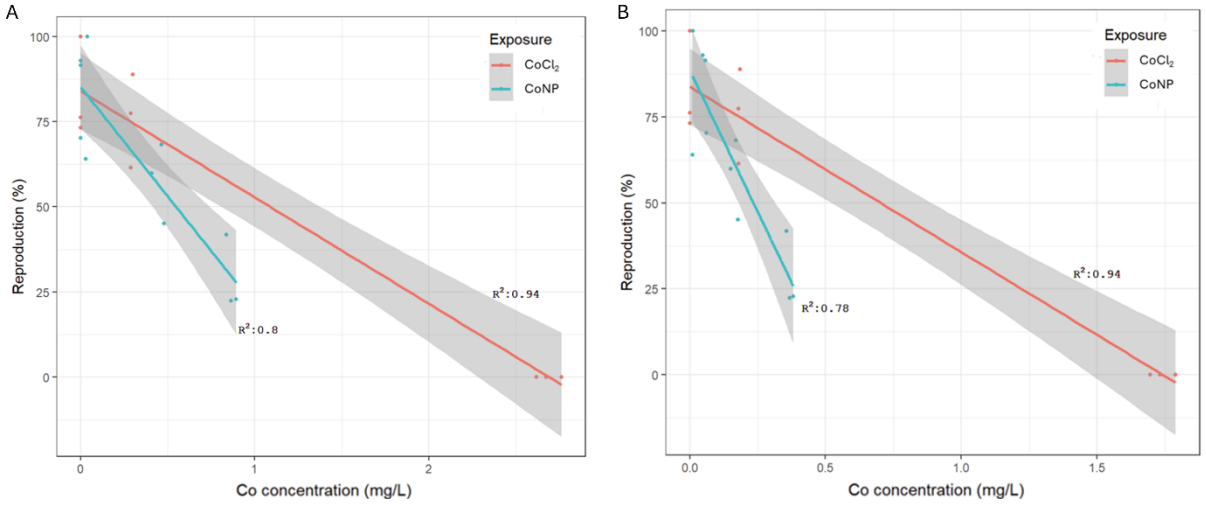

Figure 17 Linear regressions for the effect of LMM species $CoCl_2$ and CoNPs on reproduction in *C. elegans* in the presence of *E. coli* at T-0 (A) and 96h (B). Reproduction data was normalized to the mean reproduction of nematodes in the control group. The confidence intervals for each linear regression are depicted as a grey area.

In the absence of *E. coli*, the linear correlation between reproduction and LMM species from $CoCl_2$ increased compared to total Co concentration, while the correlation remained just as strong for LMM species of CoNPs (Figure 18A). At T-0, the linear regression analysis indicated that LMM species in CoNPs caused higher reduction in reproduction compared to an equivalent concentration of LMM species in $CoCl_2$ (Figure 18A). At 96h, the correlation remained strong for LMM species in CoNP exposure at 96h, while it weakened significantly for LMM species in $CoCl_2$ exposure (Figure 18B). Notably, at both T-0 (Figure 18A) and 96h (Figure 18B), the confidence intervals of $CoCl_2$ and CoNP exposures overlap.

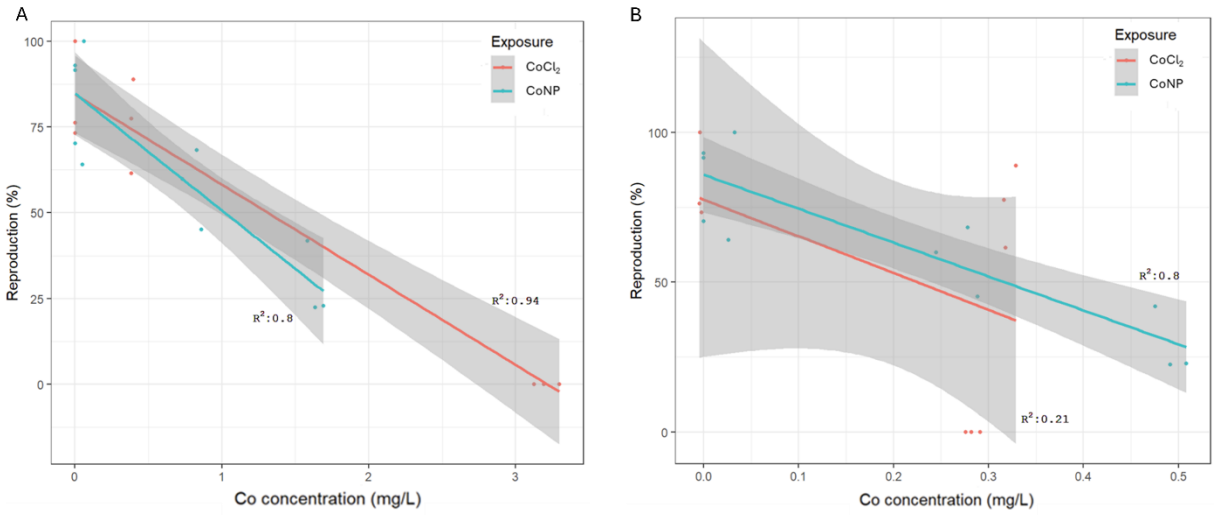

Figure 18: Linear regressions for the effect of LMM species $CoCl_2$ and CoNPs on reproduction in *C. elegans* without *E. coli* at T-0 (A) and 96h (B). Reproduction data was normalized to the mean reproduction of nematodes in the control group. The confidence intervals for each linear regression are depicted as a grey area.

Association between growth and reproduction

$CoCl_2$ and CoNP exposure showed similar trends for growth and reproduction. Therefore, a linear regression analysis was conducted to assess if there is a correlation between growth and reproduction (Figure 19). A strong positive correlation was observed between growth and reproduction in $CoCl_2$ exposed nematodes, while nematodes exposed to CoNPs showed a weaker correlation between growth and reproduction. Notably, the confidence intervals of $CoCl_2$ and CoNP exposures overlap.

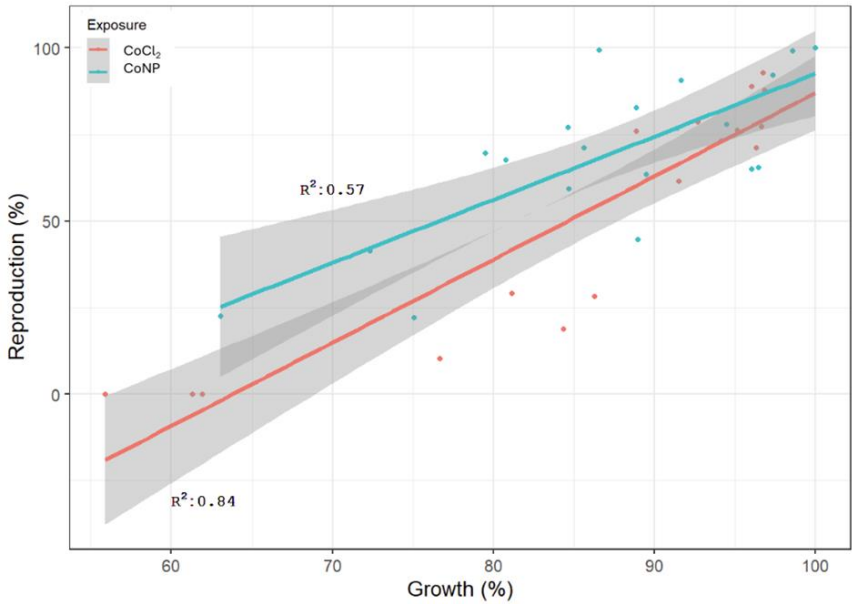

Figure 19: Linear regressions for growth and reproduction in *C. elegans* exposed to $CoCl_2$ and CoNPs. Growth data was normalized to the mean growth of nematodes in the control group. Reproduction data was normalized to the mean reproduction of nematodes in the control group. The confidence intervals for each linear regression are depicted as a grey area.

4.4. Morphological effects

Chronic exposure

Phase contrast micrographs of N2 nematodes taken 72 hours after initiation of exposure to $CoCl_2$ and CoNPs revealed impaired development. The nematodes exposed to $CoCl_2$ (Figure 20) exhibited impaired development at 1.67 mg/L and 3.30 mg/L, characterized by shortened body length, reduced number of matured oocytes, and fewer embryos. These nematodes also exhibited impaired development of the intestine. The nematode exposed to 3.30 mg/L Co showed abnormal development of the pharynx.

Nematodes exposed to CoNPs (Figure 21) showed less reduction of body length compared to the nematodes exposed to $CoCl_2$, supporting the observations in Section 4.2. However, all exposure concentrations resulted in adverse effects on oocyte maturation, with enlarged oocytes at 1.70 mg/L and 1.36 mg/L. At 5.55 mg/L, nematodes showed a reduction in the number of embryos. Furthermore, nematodes exposed to 1.36 mg/L and 5.55 mg/L Co show abnormal development of the intestine.

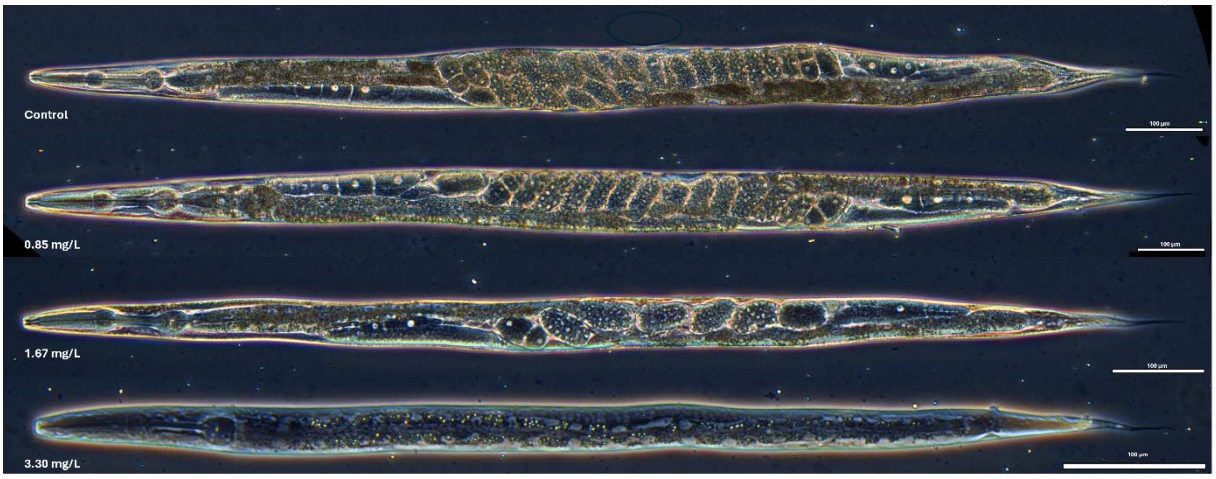

Figure 20: Representative examples of phase contrast micrographs of N2 nematodes following chronic exposure to $CoCl_2$. Scale bars represent 100 µm in all micrographs.

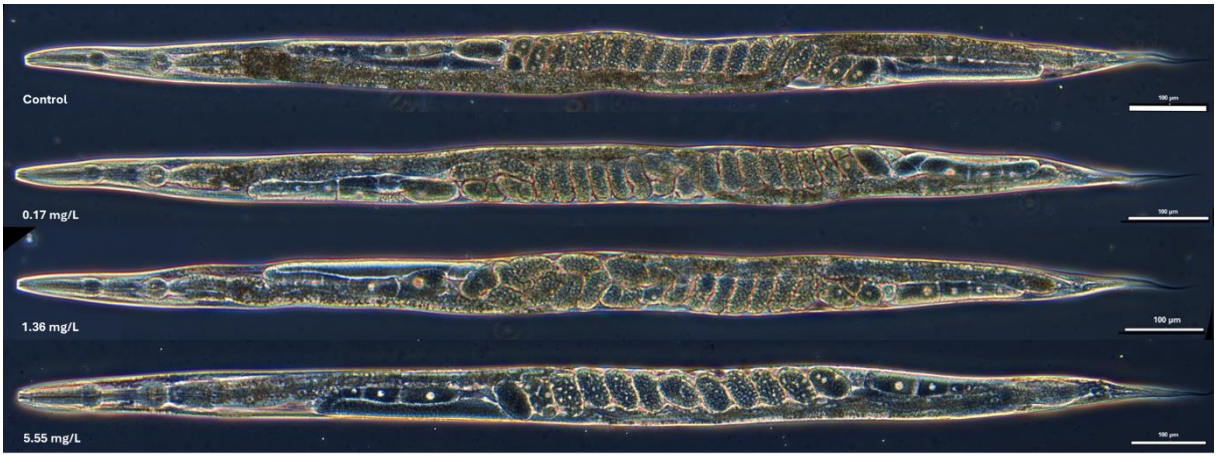

Figure 21: Representative examples of phase contrast micrographs of N2 nematodes following chronic exposure to CoNP. Scale bars represent 100 µm in all micrographs.

Acute exposure

Another set of micrographs of N2 nematodes was obtained to assess the morphological effects following acute exposure. These nematodes were developed for 48 hours, reaching the L4 stage, before a 24-hour exposure to $CoCl_2$ and CoNPs. Nematodes exposed to $CoCl_2$ (Figure 22) exhibited fewer matured oocytes and fewer embryos. Enlarged oocytes were also observed for nematodes exposed to 3.30 mg/L Co. Additionally, nematodes exposed to 3.30 mg/L and 6.94 mg/L Co had very developed embryos inside the parent nematode, indicating signs of bagging. Furthermore, nematodes exposed to 13.3 mg/L show significantly reduced development of the intestine and reproductive organs.

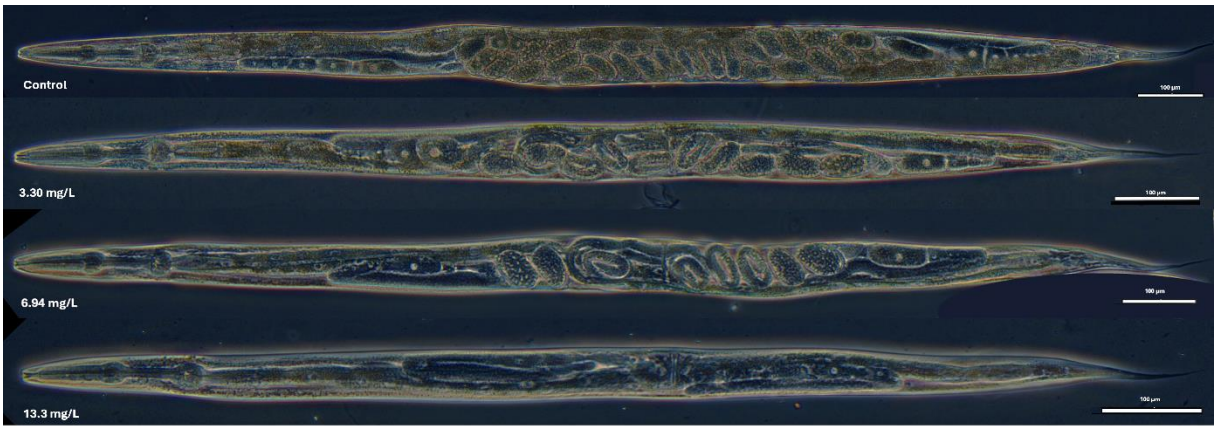

Figure 22: Representative examples of phase contrast micrographs of N2 nematodes following acute exposure to $CoCl_2$. Scale bars represent 100 µm in all micrographs.

Nematodes also exhibited vulva abnormalities (Figure 22) at every $CoCl_2$ exposure concentration. In the control group nematode, a protruding vulva with a vulva opening was observed, while in the exposed nematodes, a slit was observed (Figure 23). This vulva abnormality was neither observed in nematodes in the control group (n = 15) nor in nematodes exposed to CoNPs (n = 21). Fisher's exact tests were conducted to assess the statistical significance of the occurrence of the observed vulva abnormalities. The tests yielded statistically significant results across all $CoCl_2$ exposure concentrations (Figure 24).

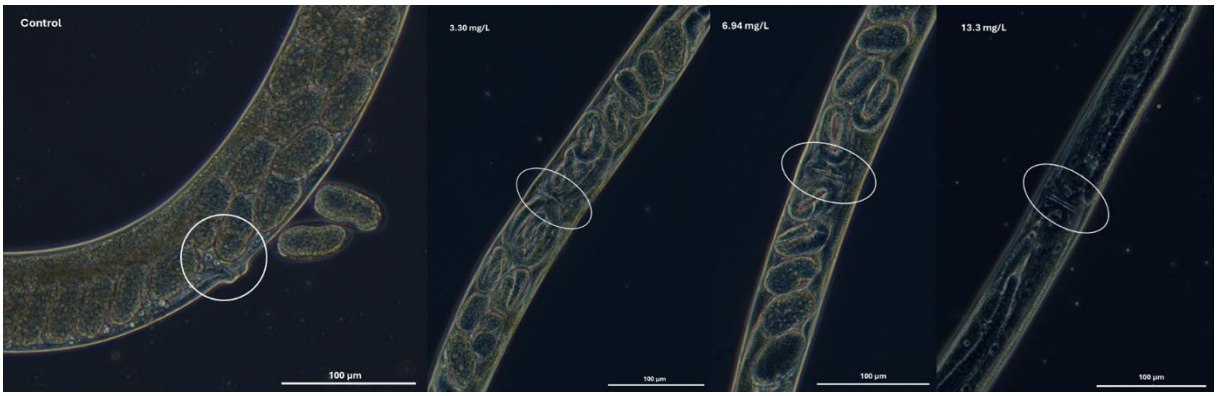

Figure 23: Vulva abnormalities (highlighted with white circles) in nematodes following acute exposure to $CoCl_2$. These micrographs were taken at 20x magnification. Scale bars represent 100 µm in all micrographs.

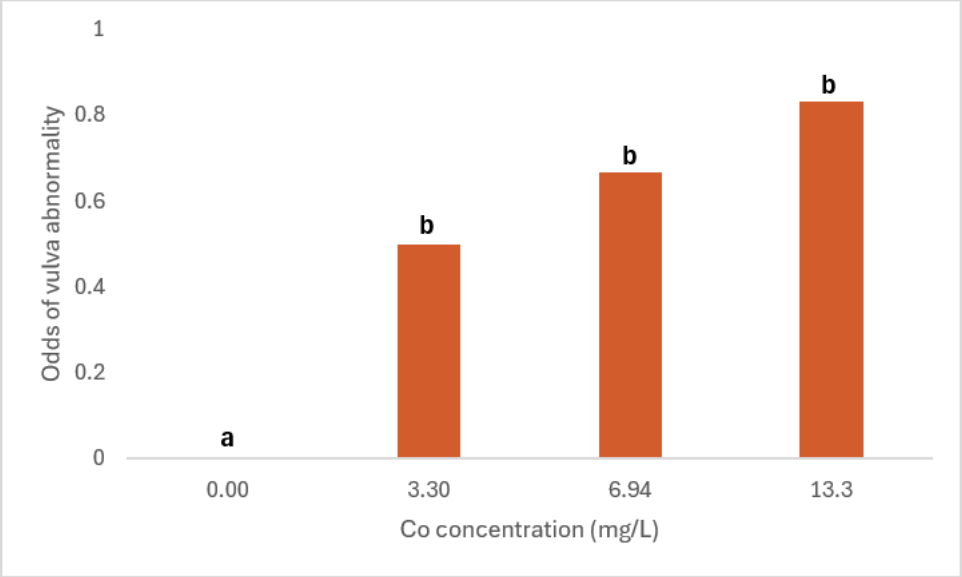

Figure 24: Odds of the occurrence of the vulva abnormalities at each $CoCl_2$ exposure concentration. Statistically significant differences, detected by Fisher's exact tests (p-value < 0.05), are marked with "b" above the corresponding bar.

Following acute exposure to CoNPs (Figure 25) nematodes across all exposure concentrations showed effects on reproduction. Fewer embryos were observed in nematodes exposed to 1.36 mg/L and 5.55 mg/L Co. Additionally, fewer matured oocytes were observed in nematodes exposed to 3.23 mg/L and 5.55 mg/L Co. Nematodes exposed to 3.23 mg/L Co showed signs of bagging as some very developed embryos were inside the parent nematode.

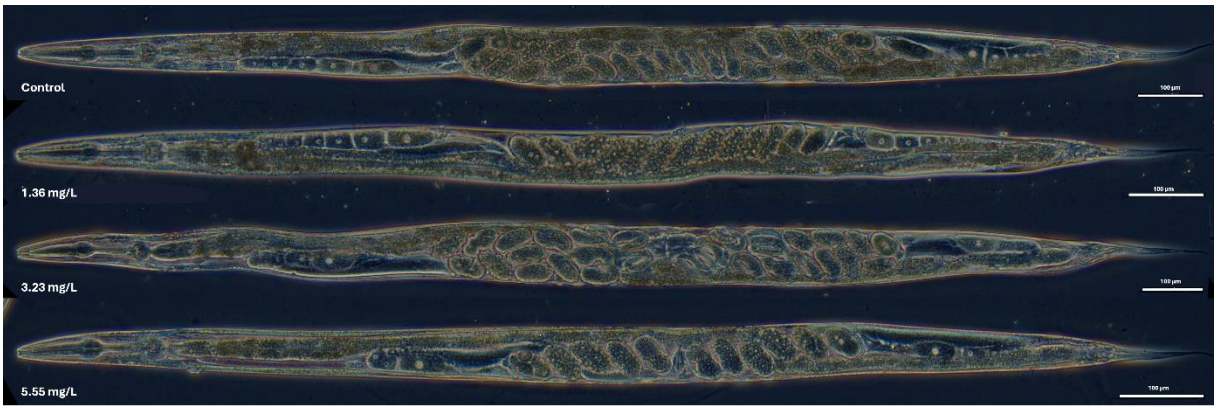

Figure 25: Representative examples of phase contrast micrographs of N2 nematodes following acute exposure to CoNP. Scale bars represent 100 µm in all micrographs.

4.5. Hypoxic response

Induction of hypoxic response in *C. elegans* was assessed using fluorescence microscopy to image the GFP signal in ZG120 and ZG444. The fluorescence intensity observed is correlated with the nhr-57 expression, which is used as an indicator of hypoxic response.

Chronic exposure

The nhr-57 expression of ZG444 nematodes was measured following 72-hour chronic exposure to $CoCl_2$ and CoNPs. The mean nhr-57 expression of individual nematodes varied within each exposure group (Figures 26). An increased expression of nhr-57 was seen in the nematodes exposed to $CoCl_2$ at 1.67 mg/L Co, while a decrease was observed at 3.30 mg/L. For the nematodes exposed to CoNPs, expression of nhr-57 seems to decrease with increasing Co exposure concentration. Figure 27 displays representative micrographs corresponding to each $CoCl_2$ exposure concentration, while Figure 28 exhibits representative micrographs for each CoNP exposure concentration.

ANOVA and Tukey's HSD tests were conducted to determine the statistical significance of fluorescence intensity differences between control and exposed nematodes. Chronic exposure to $CoCl_2$ caused a statistically significant difference between control nematodes and nematodes exposed to 1.67 mg/L Co (Figure 29A). Similarly, statistically significant differences were determined for nematodes exposed to CoNPs, particularly at concentrations 0.17 mg/L and 1.36 mg/L Co (Figure 29B).

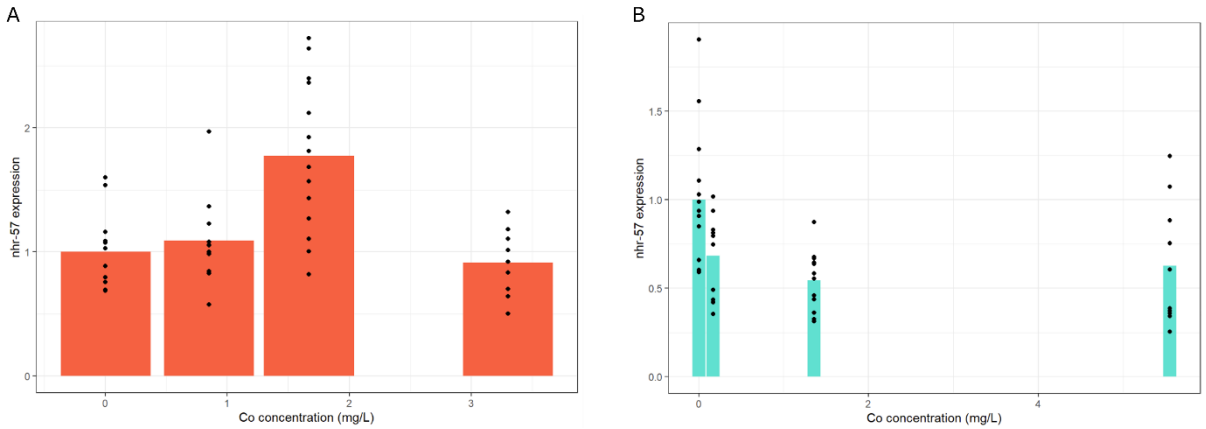

Figure 26: Mean nhr-57 expression of ZG444 nematodes at each exposure concentration following chronic exposure to $CoCl_2$ (A) and CoNPs (B). The bars represent the mean normalized fluorescence for all nematodes within an exposure group. The black dots depict the normalized fluorescence of individual nematodes observed within each exposure group.

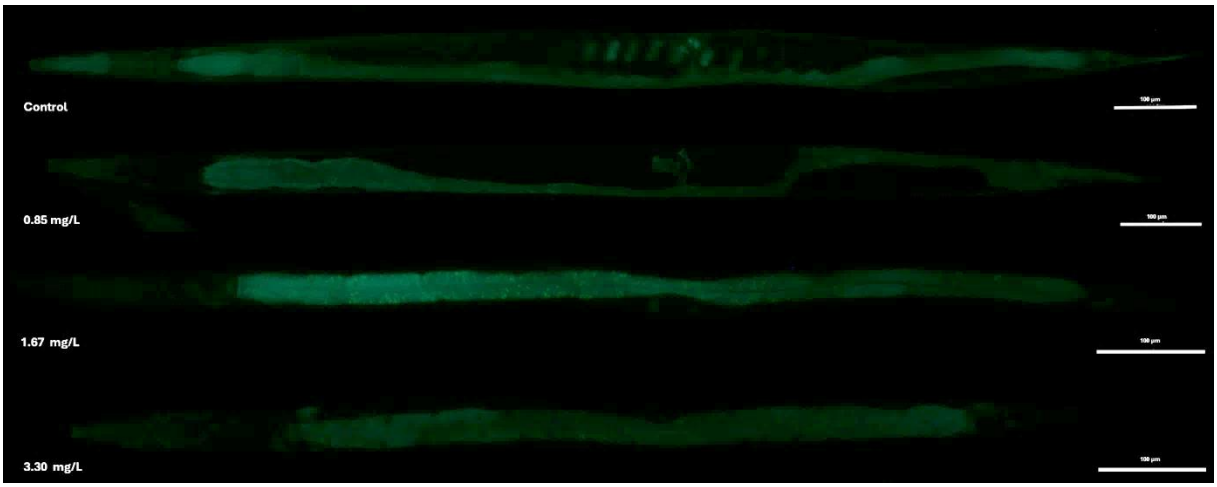

Figure 27: Representative examples of nhr-57 expression fluorescence micrographs of ZG444 nematodes following chronic exposure to $CoCl_2$. Brightness and contrast were corrected equally for all nematodes to enhance image visibility. Scale bars represent 100 µm in all micrographs.

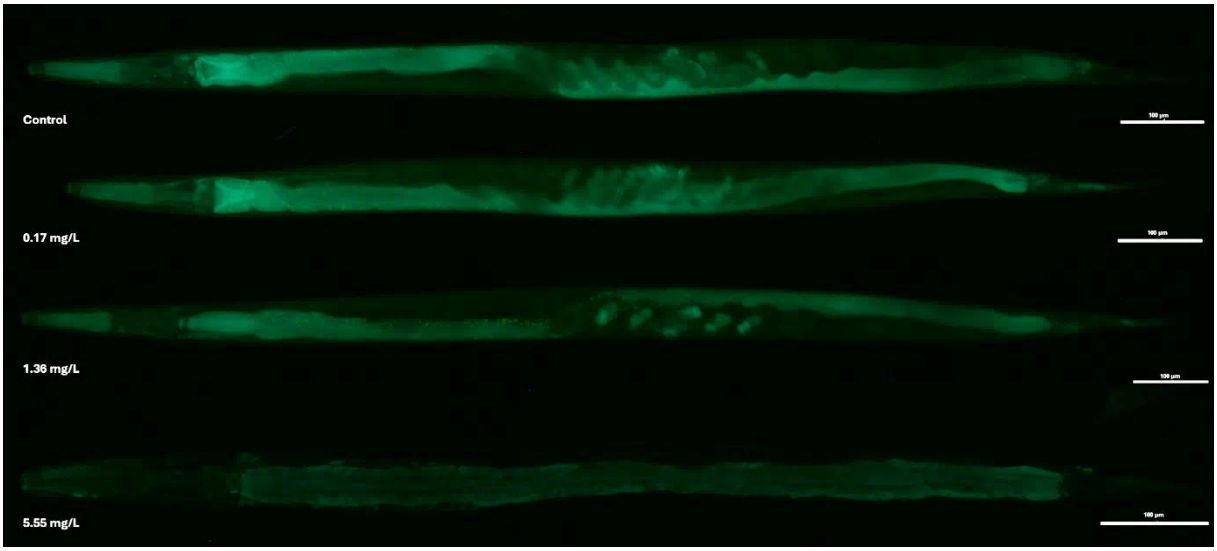

Figure 28: Representative examples of nhr-57 expression fluorescence micrographs of ZG444 nematodes following chronic exposure to CoNPs. Brightness and contrast were corrected equally for all nematodes to enhance image visibility. Scale bars represent 100 µm in all micrographs.

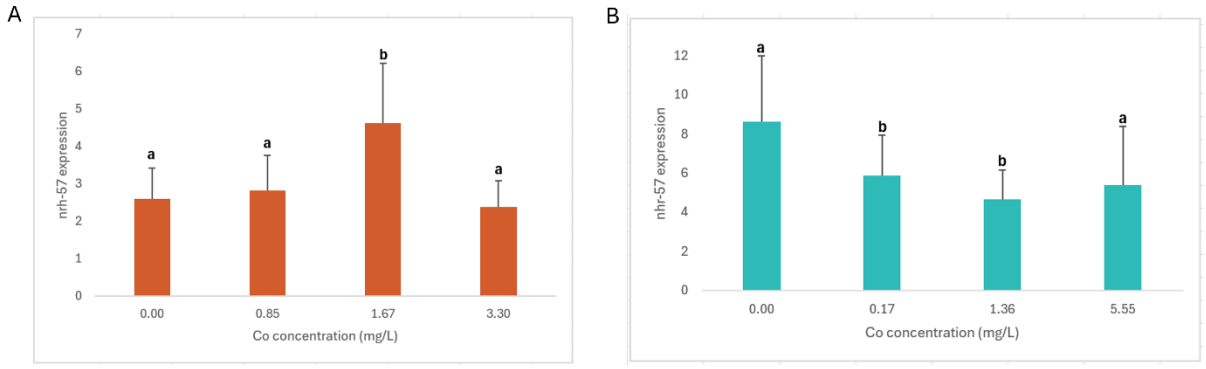

Figure 29: Mean nhr-57 expression and standard deviation at each exposure concentration. Statistically significant differences, detected by Tukey's HSD tests, in nhr-57 expression between the control and exposed nematodes are marked with "b" above the corresponding bar.

ZG444 acute exposure

L4 stage ZG444 nematodes were exposed to 4 mM paraquat, $CoCl_2$ at 3.30 mg/L Co, and CoNPs at 5.55 mg/L to assess the induction of nhr-57 expression following acute exposure. The mean nhr-57 expression of individual nematodes varied within each exposure (Figure 30A). The representative fluorescence micrographs for each exposure are shown in Figure 31. Repression of nhr-57 expression was observed for nematodes exposed to 4 mM paraquat, while the nematodes exposed to $CoCl_2$ and CoNPs showed induction of nhr-57 expression.

ANOVA and Tukey's HSD tests were employed to detect if the observed trends were statistically significant. The results show that the differences in nhr-57 expression following acute exposure to $CoCl_2$ and CoNPs are statistically significant (Figure 32).

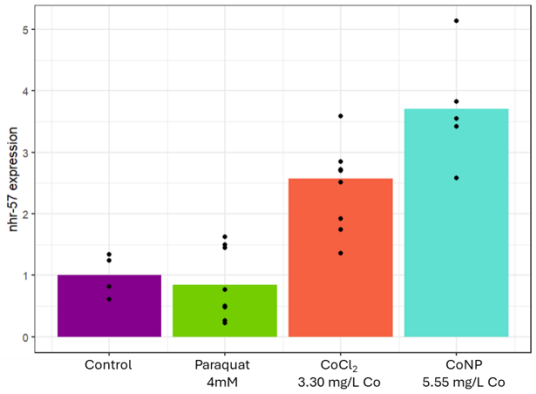

Figure 30: A: Mean nhr-57 expression of ZG444 nematodes following chronic exposure to paraquat, $CoCl_2$, and CoNPs. The bars represent the mean normalized fluorescence for all nematodes within an exposure. The black dots depict the normalized fluorescence of individual nematodes observed within each exposure.

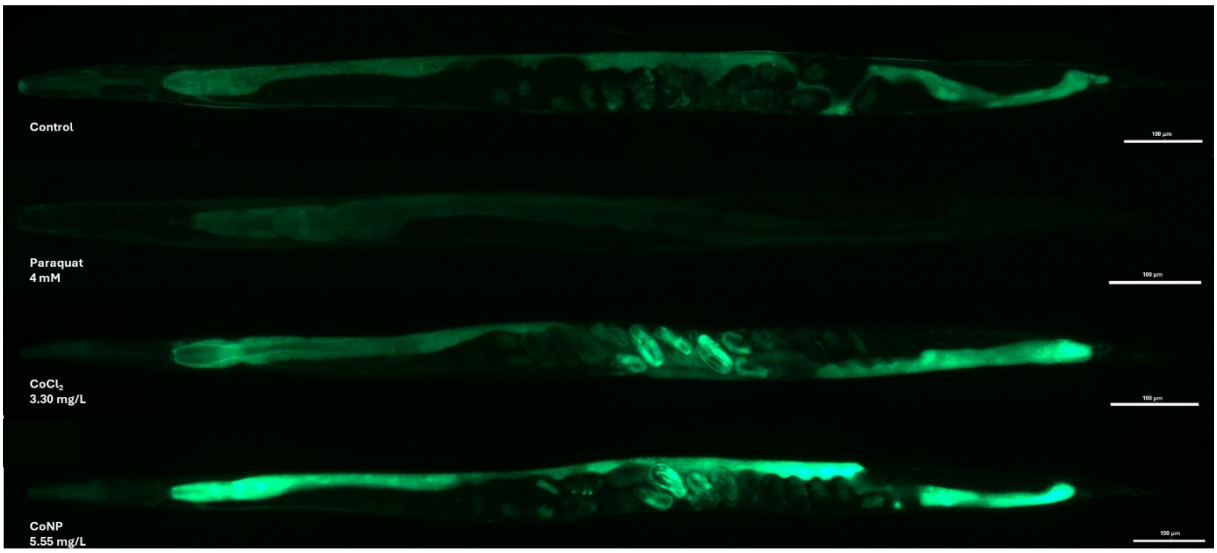

Figure 31: Representative examples of nhr-57 expression fluorescence micrographs of ZG444 nematodes following acute exposure to CoNPs. Scale bars represent 100 µm in all micrographs.

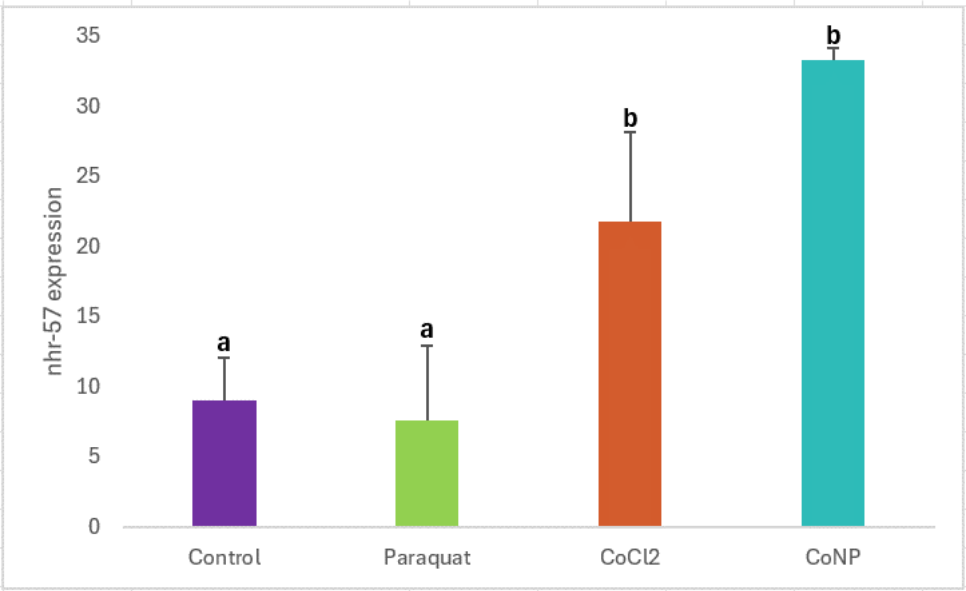

Figure 32: Mean nhr-57 expression and standard deviation at exposure. Statistically significant differences, detected by Tukey's HSD tests, in nhr-57 expression between the control and exposed nematodes are marked with "b" above the corresponding bar.

ZG120 acute exposure

ZG120 was imaged using fluorescence microscopy to assess the induction of nhr-57 expression following acute exposure to $CoCl_2$ at concentrations ranging from 1.67 mg/L, and 13.3 mg/L Co, and CoNPs, at concentrations ranging from 1.36 mg/L to 5.55 mg/L Co. The mean nhr-57

expression of individual nematodes varied within each exposure group (Figure 33). A repression of nhr-57 expression was observed for nematodes exposed to $CoCl_2$, while no clear trend was identified for nematodes to CoNPs. Figure 34 displays representative micrographs corresponding to each $CoCl_2$ exposure concentration, while Figure 35 exhibits representative micrographs for each CoNP exposure concentration.

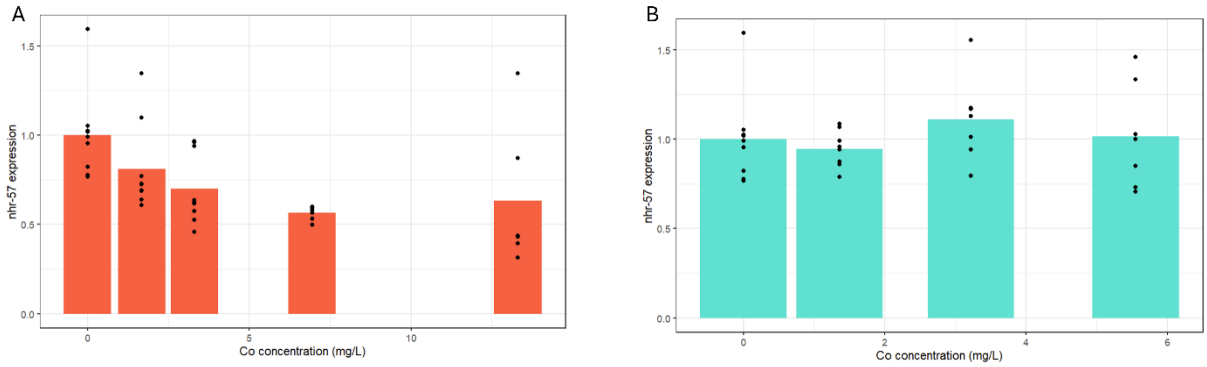

Figure 33: Mean nhr-expression of ZG120 nematodes at each exposure concentration following acute exposure to $CoCl_2$ (A) and CoNPs (B). The bars represent the mean normalized fluorescence for all nematodes within an exposure group. The black dots depict the normalized fluorescence of individual nematodes observed within each exposure group.

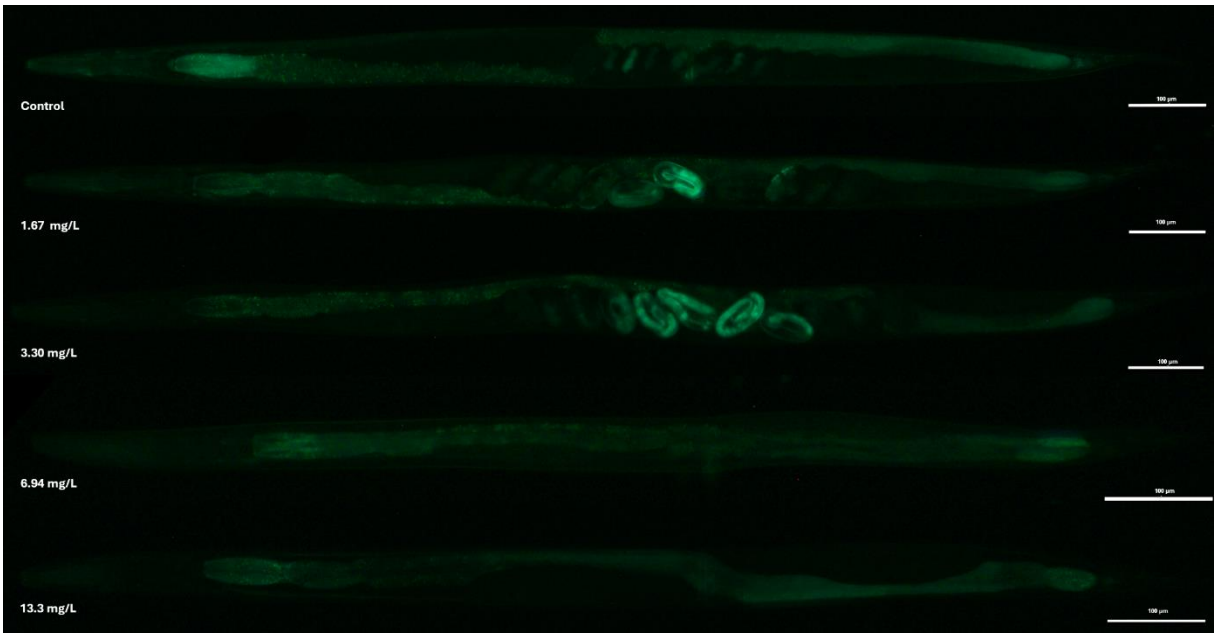

Figure 34: Representative examples of nhr-57 expression fluorescence micrographs of ZG120 nematodes following acute exposure to $CoCl_2$. Brightness and contrast were corrected equally for all nematodes to enhance image visibility. Scale bars represent 100 µm in all micrographs.

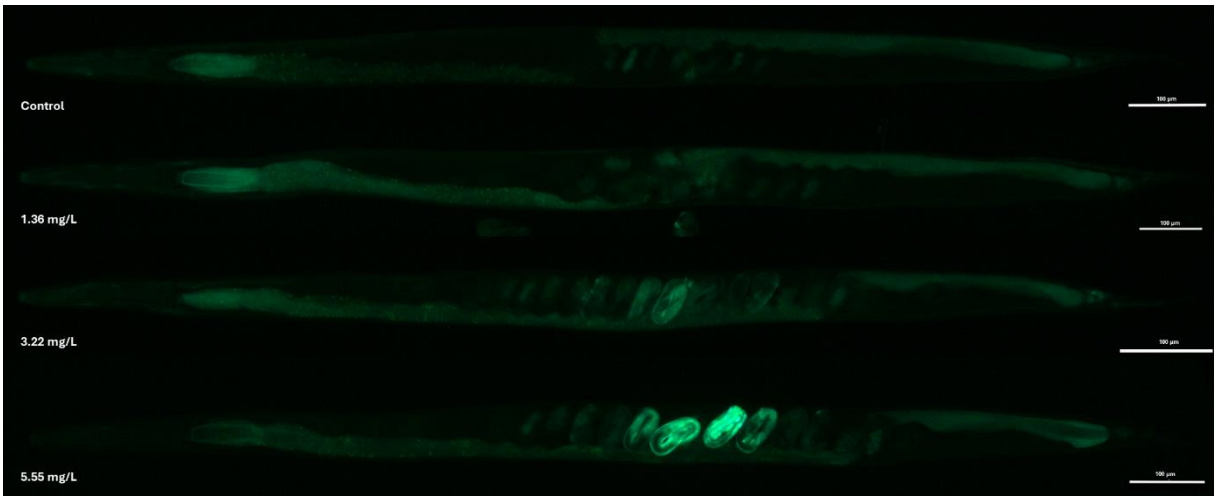

Figure 35: Representative examples of nhr-57 expression fluorescence micrographs of ZG120 nematodes following acute exposure to CoNPs. Scale bars represent 100 µm in all micrographs.

ANOVA and Tukey's HSD tests were employed to determine if the observed trends were statistically significant. Acute exposure to $CoCl_2$ caused a statistically significant difference between control nematodes and nematodes exposed to 6.94 mg/L (Figure 36). No statistical significance was detected for nematodes exposed to CoNPs.

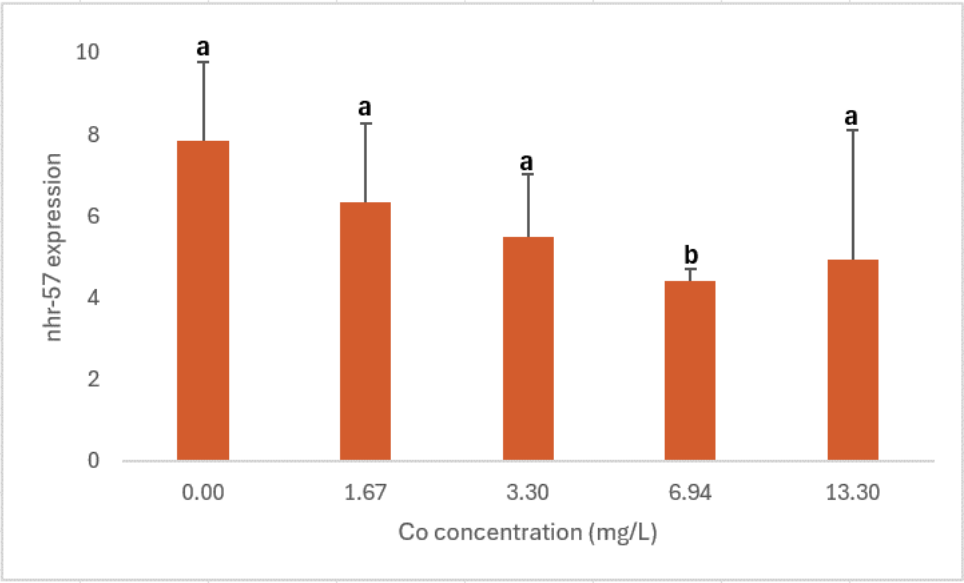

Figure 36: Mean nhr-57 expression and standard deviation at each $CoCl_2$ exposure concentration. Statistically significant differences, detected by Tukey's HSD tests, in nhr-57 expression between the control and exposed nematodes are marked with "b" above the corresponding bar. A statistically significant repression of nhr-57 expression was detected for nematodes exposed to $CoCl_2$ at the concentration of 6.94 mg/L.

In the micrographs (Figure 34 and 35) it was observed that the nhr-57 expression is localized to the embryos in the exposed nematodes. To investigate if there was a statistically significant difference in the embryos of the nematodes, the fluorescence signal in this region of interest (Figure 37) was measured for each observed nematode.

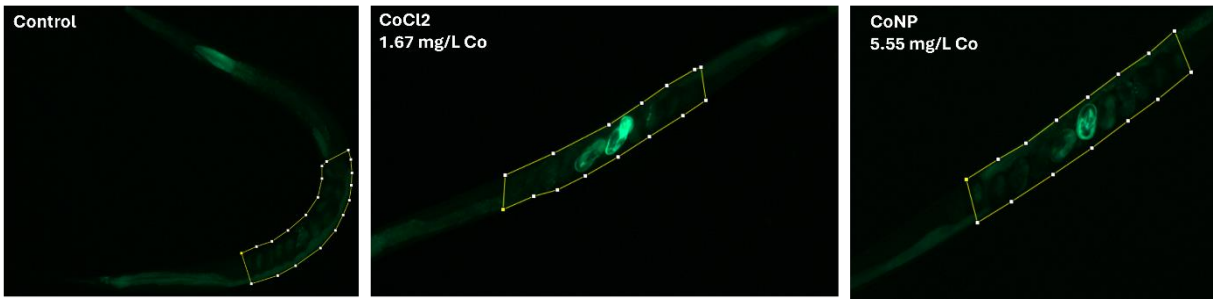

Figure 37: A depiction of how the fluorescence signal in the region of interest was isolated using ImageJ.

Figure 38 shows the mean nhr-57 expression in the region of interest in each exposure. For $CoCl_2$ (Firgure 38A) the exposed nematodes showed an increased nhr-57 expression until the 6.94 mg/L and 13.3 mg/L Co concentrations. In nematodes exposed to CoNPs (Figure 38B), nhr-57 expression increased with increasing Co concentration.

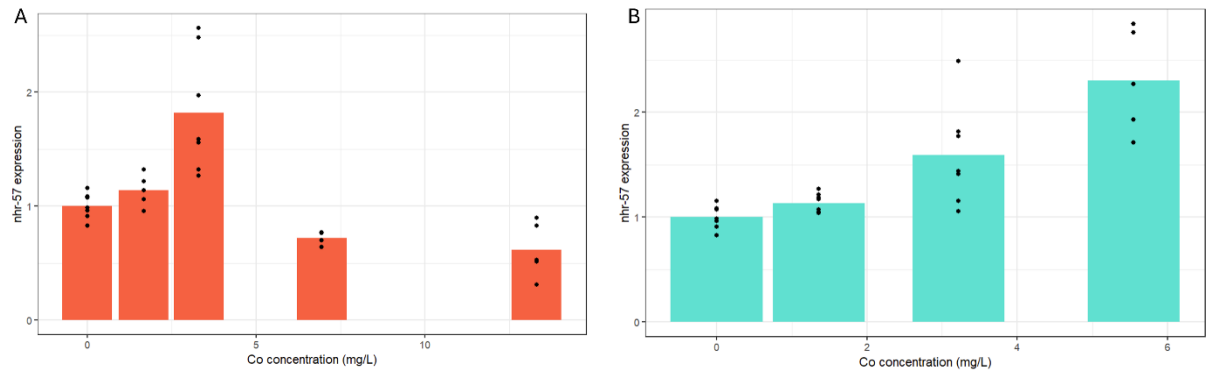

Figure 38: Mean nhr-57 expression in the region of interest in ZG120 nematodes at each exposure concentration following acute exposure to $CoCl_2$ (A) and CoNPs (B). The bars represent the mean of normalized fluorescence for all nematodes within an exposure group, while the black dots depict the normalized fluorescence of individual nematodes observed within each exposure group.

ANOVA and Tukey's HSD test were conducted to assess if the observed differences were statistically significant. In $CoCl_2$ exposures (Figure 39A) the concentration of 3.30 mg/L Co resulted in a significant induction of nhr-57 expression in the region of interest. CoNP exposure (Figure 39B) at 3.22 mg/L and 5.55 mg/L Co caused a significant induction of nhr-57 expression in the region of interest.

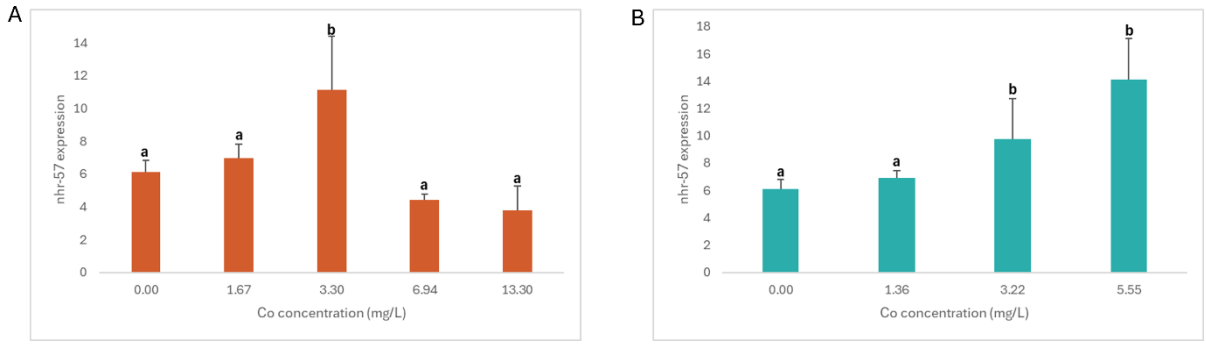

Figure 39: Mean nhr-57 expression and standard deviation in region of interest at each exposure concentration. Statistically significant differences, detected by Tukey's HSD tests, in nhr-57 expression between the control and exposed nematodes are marked with "b" above the corresponding bar.

To assess the dose-response relationship between Co concentration and nhr-57 expression in the region of interest, linear regression analyses were conducted. When all exposure concentrations of $CoCl_2$ were included in the analysis, a very weak correlation was observed between $CoCl_2$ exposure and nhr-57 expression (Figure 40A). In contrast, a strong correlation was observed between nhr-57 expression and CoNP exposure. In Figure 39B, the concentration of 6.94 mg/L and 13.3 mg/L Co from the $CoCl_2$ exposure were excluded from the analysis, as nhr-57 expression was repressed in these concentrations. The correlation between $CoCl_2$ exposure and nhr-57 expression in the region of interest increased after excluding these concentrations, while the correlation between CoNP exposure and nhr-57 expression remained unchanged. Notably, the confidence intervals of both $CoCl_2$ and CoNP exposures overlap in Figure 40B.

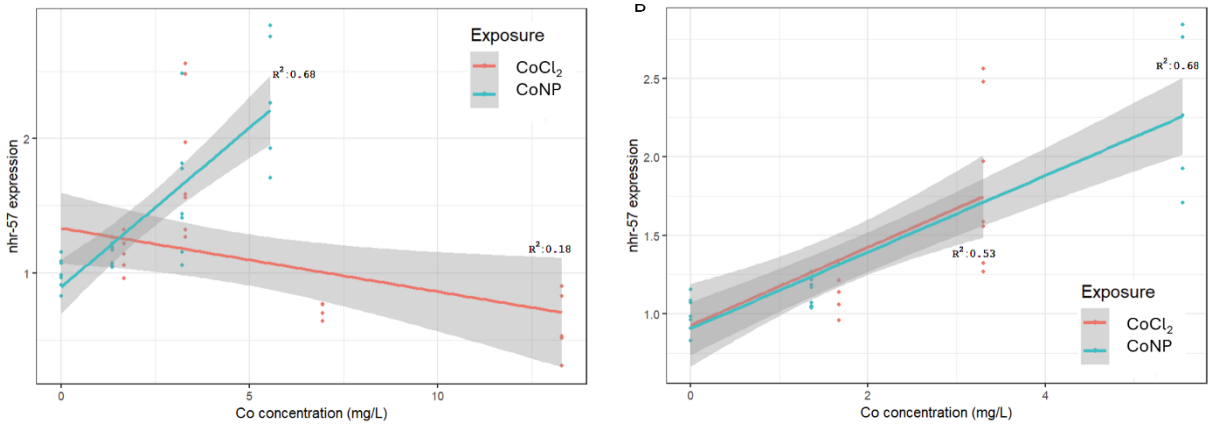

Figure 40: Linear regressions for nhr-57 expression in the region of interest in ZG120 exposed to $CoCl_2$ and CoNPs. All concentrations of $CoCl_2$ were included in analysis A, while the highest concentrations (6.94 mg/L and 13.3 mg/L Co) were excluded in analysis B. The confidence intervals for each linear regression are depicted as a grey area.

5. Discussion

5.1. Nanoparticle characteristics

As mentioned in Section 2.4, to understand the toxicity potential of NPs, several properties including size, dispersion state, and surface charge should be assessed. In this project, the CoNP suspension used to evaluate the toxicity of CoNPs was prepared using QSI-nano cobalt. Previous research has demonstrated that these nanopowder spheres have a diameter size of 3.9 ± 0.8 nm (Oughton et al., 2008).

Various methods were employed to characterize the size of CoNPs in the NP exposures. TEM analysis (Figure 7A) revealed a high degree of NP aggregation in the suspension, with individual NPs measuring a diameter below 10 nm (Figure 7B and 7C). This NP size is larger than the size demonstrated by Oughton and colleagues (2008) (Oughton et al., 2008). Synchrotron radiation analysis of NP suspension prepared with QSI-nano cobalt detected only that CoNPs that had been oxidized following equilibration (Cagno et al., 2017). Oxidation of NPs changes their structure and may explain the difference in observed NP size.

DLS measurements (Figure 8) yielded an average hydrodynamic particle diameter of 155.7 ± 0.8 nm, which is considerably larger than the size of individual CoNPs within the suspension and nanopowder. This suggests that large NP agglomerates dominated the DLS measurements. The size distribution (Figure 8) further illustrated particle aggregation, as the majority of NPs fell within the size range of 40-1000 nm, and a small fraction ranged from 2000 to 6000 nm.

Furthermore, the determination of PDI for the NP suspension resulted in a value of 0.362 ± 0.011, surpassing the ISO threshold of monodispersity, set at 0.07 (ISO, 2017). This indicates that the CoNP exhibited some degree of polydispersity, increasing the likelihood of particle settling and instability. The high PDI value also suggested a broad distribution of CoNPs in the NP suspension. Additionally, the CoNPs showed a zeta potential value of -16.2 ± 0.3 mV, indicating suspension instability and increased probability of particle aggregation. These results suggesting CoNP suspension instability and particle aggregation, are supported by observation with TEM analysis and DLS measurements.

Aggregation may decrease the cellular uptake of the large NP aggregates in the suspension, potentially reducing the toxicity of the CoNPs in the exposure. A study investigating the different uptake patterns between single NPs and aggregated gold NPs demonstrated a 25% decrease in the uptake of aggregated NPs in HeLa and A549 cells, while uptake was doubled in

MDA-MB 435 cells (Albanese & Chan, 2011). This suggests that the cell type, in addition to NP size, may significantly influence the cellular uptake of NPs, and such uptake patterns should be considered on a cell-to-cell basis.

Ideally, size distribution, zeta potential, and PDI should have been measured for each individual NP suspension before it was used in the exposure media. However, due to technical complications with the Malvern Zetasizer software, these properties were only measured for one NP suspension. This has resulted in a limited understanding of variability among the different CoNP suspensions used to assess toxicity and hypoxic response in this project and may impact the interpretation of toxicity results.

5.2. Exposure concentrations

Significant variations in the total Co concentration were observed between CoNP suspensions, even though they were prepared in a similar manner. Similarly, the two highest $CoCl_2$ exposure concentrations, with the nominal exposure concentrations of 16 mg/L and 8 mg/L, varied within the triplicate measurements. Thus, the mean Co exposure concentration used to assess morphological effects and hypoxia response might not accurately represent the actual Co exposure concentration during these exposures.

The ionic species of Co, particularly Co^{2+}, are considered the most bioavailable and toxic forms of Co. Thus, not just the total Co concentration but also the concentration of Co ion species is crucial for understanding toxicity. In this project, LMM is defined as substances with molecular weight smaller than 3 kDa, serving as an indicator of unbound Co ion species within $CoCl_2$ and CoNP exposures.

The presence of *E. coli* in the exposure media has been shown to influence the species transformation dynamics of $CoCl_2$ and CoNPs, as evidenced by comparative fractionation analyses conducted without *E. coli* (Figure 10). Notably, the decrease in the LMM fraction in the presence of *E.* coli coincided with a comparable increase in the aggregated fraction of $CoCl_2$ over the 96-hour period (Figure 9). This observation suggests a potential interaction wherein the negatively charged surface of *E. coli* binds Co^{2+} in $CoCl_2$ (Alves et al., 2010). Thus, *C. elegans* may orally ingest Co ion species bound to *E. coli*. Furthermore, the binding of Co^{2+} to *E. coli* may facilitate them through the digestive tract of *C. elegans* without cellular uptake, thereby reducing the bioavailability and toxicity associated with Co^{2+}.

Similarly, the LMM species of CoNPs experience a decrease over the 96-hour period, both with and without the presence of *E. coli*. In the absence of *E. coli,* the Co ion species accounted for approximately 25% of Co concentrations of the NP suspension at T-0, suggesting ion leaching during the 24-hour incubation period prior. A study has shown the presence of cobalt oxide (Co_3O_4) in the CoNPs, and oxidized NPs show greater ion leaching (Cagno et al., 2017). This may explain the high LMM fraction at exposure start.

The fractionation analysis (Figure 9) showed that a decrease in CoNP LMM species did not coincide with an increased aggregated fraction in the presence of *E.coli*, as observed for $CoCl_2$. Rather, the aggregated fraction of CoNPs remains virtually unchanged over the 96-hour period. This can be explained by the negative zeta potential of the CoNPs, thereby not binding to the negatively charged surface of *E. coli.* The decrease in CoNP LMM species over the 96-hour, coincides with an increase in the aggregated fraction in the absence of *E. coli*, which may suggest that the NPs more readily aggregate in the absence of *E. coli*. In respect to bioavailability, these observations of LMM species transformation can be interpreted as CoNP exposure being more toxic at the start of the exposure, as Co ion species decreased over the 96-hour period. The binding of the LMM species to *E. coli* has been shown to promote the ingestion and uptake of ions in *C. elegans* , thus making them more bioavailable (Kleiven et al., 2018).

Although fractionation analyses were conducted at T-0 and 96h and provide valuable insight into the distribution and transformation of species of $CoCl_2$ and CoNPs, they do not capture the dynamic species transformation occurring between these time points. As a result, information about species distribution, particularly the concentration of the bioavailable Co ion species, at a specific intermediate time during the exposure remains unknown.

5.3. Toxicity

Growth

Findings in this project showed that chronic exposure to both $CoCl_2$ and CoNP caused statistically significant reductions (Figure 11) in the total nematode body length. However, $CoCl_2$ exhibited higher potent toxicity as it caused higher growth reduction compared to the same total Co concentration of CoNPs, with nematodes exposed to $CoCl_2$ at concentrations as low as 1.70 mg/L experienced statistically significant growth reduction, while CoNP exposed nematodes were significantly smaller than control nematodes at 6.95 mg/L. Thus, a very strong dose-response between $CoCl_2$ exposure concentration and total body length was detected. This

dose-response was weaker for CoNPs exposed nematodes, suggesting that either CoNPs are less toxic than $CoCl_2$ or that growth reduction is linked to specific Co species, rather than total Co concentration.

Analysis of the effect of LMM species on total body length revealed that Co ion species in CoNPs led to a greater reduction of growth, as indicated by the steeper slope of the linear regression line (Figures 13 and 14) for CoNP exposure compared to $CoCl_2$. These results support the previous findings of Co ion species being the most toxic form, as it is more bioavailable (Leyssens et al., 2017; Simonsen et al., 2012). In the absence of *E. coli*, significant overlap was observed, indicating that Co ion species of CoNP cause the observed reduction in growth. Notably, no overlap was observed between the confidence intervals of Co ion species of CoNPs and Co^{2+} fraction of $CoCl_2$ when *E. coli* was present in the exposure media. These findings suggest that additional mechanisms contribute to the reduction in growth observed following chronic exposure to CoNPs. The presence of *E. coli* may have increased the uptake of Co ion species in CoNPs compared to Co^{2+} in $CoCl_2$. This might explain why Co ions species in CoNPs caused a greater reduction of growth compared to Co^{2+} from $CoCl_2$ at the same concentration of LMM species.

Reproduction

Statistically significant differences in reproduction were observed for both $CoCl_2$ and CoNP chronic exposures (Figure 15). Similarly to growth, $CoCl_2$ exhibited higher potent toxicity on reproduction compared to CoNPs at the same Co concentration. EC_{50} for nematodes exposed to $CoCl_2$ was predicted to be 1.09 mg/L, while the EC_{50} for CoNP exposed nematodes was predicted to be almost 4x higher (Figure 16), supporting the claim that $CoCl_2$ exhibited higher potent toxicity. This is likely due to a higher LMM fraction in $CoCl_2$ exposure compared to CoNP exposure, as shown by the fractionation analysis in Figure 9. By assessing the effect of LMM species on reproduction it was revealed that Co ion species in CoNPs led to greater inhibition of reproduction compared to Co^{2+} in $CoCl_2$.

Analysis of the effect of LMM species on reproduction suggests a greater reduced reproduction and that Co ion species, as indicated by the steeper slope of the linear regression line (Figures 17 and 18) for CoNP exposure compared to $CoCl_2$. The strong correlation between reduced reproduction and LMM indicates that toxicity could to a significant extent be ascribed to Co ion species.

In the absence of *E. coli*, significant overlap was observed, indicating that Co ion species of CoNP cause the observed reduction in reproduction. Notably, no overlap was observed between the confidence intervals of Co ion species of CoNPs and Co^{2+} fraction of $CoCl_2$ when *E. coli* was present in the exposure media. These findings suggest that additional mechanisms contribute to the reduction in reproduction observed following CoNP exposure. The presence of *E. coli* may have increased the uptake of Co ion species in CoNPs compared to Co^{2+} in $CoCl_2$. This might explain why Co ions species in CoNPs caused a greater reduction of reproduction compared to Co^{2+} from $CoCl_2$ at the same concentration of LMM species.

Association between growth and reproduction

Comparable trends were noted in the reduction of growth and reproduction following chronic exposure to both $CoCl_2$ and CoNPs. The linear regression analysis (Figure 19) demonstrated a strong correlation between growth and reproduction in nematodes exposed to $CoCl_2$, whereas the correlation is weaker for those exposed to CoNPs. This suggests that the reduction in reproduction may stem from the effects on development resulting from $CoCl_2$ and CoNP exposure, rather than from the exposures themselves.

5.4. Morphological effects

Chronic exposure

The effects observed on reproduction and growth following the 96-hour chronic toxicity to $CoCl_2$ and CoNP were supported by observations in the phase contrast micrographs taken of the nematodes following 72 hours of exposure. Nematodes exposed to $CoCl_2$ (Figure 20) exhibited reduced total body length at 1.67 mg/L and 3.30 mg/L compared to the control nematodes, while the reduction of body length was not as significant following CoNP exposure (Figure 21). Additionally, nematodes exposed to $CoCl_2$ and CoNPs displayed signs of impaired reproduction such as reduced oocyte maturation, enlarged oocytes, and a reduced number of embryos. The micrographs also confirmed that development had a higher effect on reproduction in nematodes exposed to $CoCl_2$ than in nematodes exposed to CoNPs. This is evidenced by the nematode exposed to CoNP at 5.55 mg/L Co being of similar length and seemingly at the same developmental stage as the control nematode exhibiting significant adverse effects on reproduction, including a reduced number of oocytes and embryos (Figure 21). This suggests that reduced reproduction is not only a direct effect of reduced growth but can also be affected by CoNP exposure.

Additionally, nematodes exposed to $CoCl_2$ at 3.30 mg/L Co display a disproportionately large pharynx compared to their size. It has been shown the pharynx in *C. elegans* develops independently from the rest of the organism. (Mörck et al., 2003). Embryos produce well-differentiated pharynx even with abnormal development in other tissues (Mango, 2007). This may explain why the pharynx did not experience the same delayed development as seen in the rest of the organs of the exposed nematodes. Furthermore, nematodes at this exposure concentration also showed significant impairment to the intestine. Nematodes exposed to CoNPs at 5.55 mg/L Co also exhibited an underdeveloped intestine. No effects exclusively due to CoNP exposure were identified.

Acute exposure

Micrographs obtained following acute exposure showed significant differences between control nematodes and nematodes exposed to $CoCl_2$ and CoNPs. $CoCl_2$ exposure at 13.3 mg/L resulted in several abnormalities, including reduced growth, no embryos, reduced oocyte maturation, fewer matured eggs, impaired intestine development, and abnormal vulva development. Nematodes exposed to $CoCl_2$ at 3.30 mg/L and 6.94 mg/L exhibited enlarged oocytes, reduced oocyte maturation, and vulva abnormalities. These nematodes also exhibit egg retention and very developed embryos, indicating bagging. Bagging is the retention and internal hatching of eggs, and the body contents of the adult nematodes are consumed by the progeny as nutrition. This is an adaptation *C. elegans* undergoes under a range of stressful conditions, such as starvation, and has also been observed in egg-laying defective mutants (J. Chen & Caswell-Chen, 2004).

The observed bagging could be a result of acute exposure to $CoCl_2$, or the vulva abnormalities observed at all $CoCl_2$ exposure concentrations (Figures 22 and 23). As mentioned in Section 2.4, the egg-laying apparatus in *C. elegans* undergoes significant development during the L4 larval stage, wherein they develop the vulva. In this project, L4 stage nematodes were exposed to $CoCl_2$, thus coinciding with the time of vulva development. In Section 4.5 it has been presented that acute $CoCl_2$ exposure at 3.30 mg/L Co induced nhr-57 expression. Nhr-57 inhibits the RAS/MAPK signaling pathway in vulval precursor cells (VPCs), preventing the differentiation of VPCs (Maxeiner et al., 2019). Thus, observed vulva abnormalities and induction of nhr-57 suggest that exposure to $CoCl_2$ at the L4 stage had a significant impact on the vulva development and the subsequent egg-laying of progeny.

The nematodes exposed to CoNPs exhibited several effects including fewer embryos at 1.36 mg/L and 5.55 mg/L Co, despite no significant reduction in growth. This once again corroborates that CoNP exposure does affect reproduction, even in nematodes that don't display reduced development. The nematodes exposed to 3.23 mg/L displayed bagging like the nematodes exposed to $CoCl_2$. However, the vulva abnormalities observed in $CoCl_2$ were not detected in CoNP exposed nematodes. In the region of interest, which included the vulva, nhr-57 expression is induced, thus the molecular mechanism of nhr-57 preventing VPCs differentiation may explain the observed bagging in nematodes exposed to CoNPs at 3.23 mg/L Co.

5.5. Hypoxic response

The fluorescence signals following chronic exposure to $CoCl_2$ showed an increased induction of the nhr-57 expression in nematodes exposed to 1.67 mg/L Co, while the nhr-57 expression was repressed at 3.30 mg/L. This suggests that exposure to $CoCl_2$ does induce hypoxic response, but until a certain exposure concentration. At high exposure concentration, $CoCl_2$ causes such significant effects on nematode development that the expression of nhr-57 is likely affected. Thus, underdeveloped nematodes have repressed nhr-57 expression than more developed nematodes.

CoNP exposed nematodes displayed repression of nhr-57 expression, with the exposure at 1.36 mg/L causing statistically significant repression. Micrographs (Figure 28) revealed that the nematodes exposed to 5.55 mg/L Co had reduced development, which may explain the repression of nhr-57 expression. Another possible explanation might be insufficient O_2 assess during *C. elegans* cultivation. Even though they are incubated with gentle shaking to ensure sufficient supply of to O_2, there is a possibility that the nematodes are subjected to hypoxia during cultivation. Ginouvès and colleagues (2008) demonstrated using HeLa cells that under chronic hypoxia initiates a negative feedback loop, which leads to the overactivation of PHDs, causing HIF degradation and a desensitized hypoxic response (Foxler et al., 2018; Ginouvès et al., 2008). Therefore, if the nematodes used experienced chronic hypoxia, they might have developed an overactive EGL-9, which might not be repressed by Co^{2+} binding in the active site.

The unexpected negative correlation observed between CoNP exposure concentration and the repression of nhr-57 expression contradicted the initial hypothesis. However, as described by

Shao etal 2009, the ZG444 strain carries a deletion, which renders EGL-9 partially functional (Shao et al., 2009). As explained in Section 2.3, EGL-9 is a hydroxylase responsible for regulating HIF-1 in *C. elegans* by hydroxylating HIF-1 at proline 621, leading to the subsequent its degradation (Berra et al., 2006; Epstein et al., 2001; Shao et al., 2009). A deletion in EGL-9 would imply that HIF-1 is readily accumulated and causes constitutive activation of hypoxia target genes, including the *nhr-57* gene. Thus, the replacement of Fe^{2+} by Co^{2+} at the active site should have little to no effect on HIF-1 activity.

The deletion in ZG444 strain is a *egl-9(gk277)* mutation, which removes the MYND domain of EGL-9 (Shao et al., 2009). The active site, with the Fe^{2+}-binding site, where proline 621 is hydroxylated is not in this domain. Shao and colleagues (2009) demonstrated that the deletion in *egl-(gk277)* has little effect on the ability of EGL-9 hydroxylate HIF-1. However, the results shown in Figures 28 and 29B clearly demonstrated that CoNPs repressed nrh-57 expression across all exposure concentrations, with exposure at 0.17 and 1.36 mg/L causing statistically significant repression.

To further investigate whether the repression of nhr-57 expression in nematodes exposed to CoNPs was due to reduced development or by the EGL-9 deletion mutation, acute exposures were conducted on both ZG444 and the ZG120 strain, which is a wildtype nematode modified to express GFP with nhr-57.

By allowing the nematodes to develop to the L4 larval stage prior to exposure, the effects of reduced development were minimized. ZG444 was subjected to acute exposure to 4 mM paraquat, CoCl at 3.30 mg/L Co, and CoNPs at 5.55 mg/L to assess if the *egl-9(gk277)* mutation causes constitutive induction of nhr-57 expression. Paraquat 4 mM was chosen as a positive control as previous research has demonstrated that 4 mM paraquat causes induction of nhr-57 expression (Padmanabha et al., 2015). The same study also showed that $CoCl_2$ does not induce nhr-57 expression. The findings in this project demonstrated that both $CoCl_2$ and CoNPs cause a statistically significant (Figure 30) induction of nhr-57 expression at 3.30 mg/L and 5.55 mg/L respectively, supporting the findings of Shao and colleagues (2009).

However, paraquat did not cause a significant difference in expression. Paraquat exposure did cause developmental arrest in the exposed nematode, likely due to the exposure concentration at 4 mM being too toxic. This does support the previous findings that suggest a relationship between development and nhr-57 expression.

The embryos and the intestine in nematodes exposed to $CoCl_2$ and CoNPs displayed intense fluorescence signals. This might explain why development influences nhr-57 expression, as underdeveloped nematodes have fewer matured embryos, where the nhr-57 expression seems to be localized.

L4 stage ZG120 nematodes were exposed to a wider range of exposure concentrations to assess the dose-response between Co concentration and nhr-57 expression. The nematodes exposed to $CoCl_2$ showed a negative correlation between exposure concentration and nhr-57 expression (Figure 33). A statistically significant repression of nhr-57 expression was detected for 6.94 mg/L Co. Micrographs of these nematodes (Figure 34) showed reduced growth and lacked embryos in the 6.94 mg/L and 13.3 mg/L Co exposures. This may explain the repression of nhr-57 expression at these exposure concentrations, further supporting the claim that there is a positive correlation between development and nhr-57 expression. For the nematodes exposed to 1.67 mg/L and 3.30 mg/L Co the nhr-57 expression is mostly localized to the embryos.

For ZG120 nematodes exposed to CoNPs, no significant trend was observed in nhr-57 expression across different exposure concentrations. The micrographs of these nematodes (Figure 35) also displayed that the nhr-57 expression is localized in the embryos, and nematodes exposed to 5.55 mg/l exhibited a significantly higher fluorescence signal in their embryos compared to the embryos in the control nematodes.

Therefore, a region of interest including the embryos was defined (Figure 37). Nematodes exposed to $CoCl_2$ showed induction of nhr-57 expression until the exposure concentrations caused reduced development and reproduction, with statistically significant induction detected at 3.30 mg/L Co (Figure 39A). Similarly, nematodes exposed to CoNPs exhibited induction of nhr-57 expression, with statistically significant induction determined at 5.55 mg/L Co (Figure 39B). Linear regression analyses was conducted to assess the dose-response between Co concentration and nhr-57 expression. In the analysis that excludes 6.94 mg/L and 13.3 mg/L Co from the $CoCl_2$ exposure (Figure 40B) it is evident that there is some correlation between Co concentration and nhr-57 expression. The variations of nhr-57 expression within each exposure concentration result in the R^2 for both $CoCl_2$ and CoNP exposure to be lower than 0.7. Notably, the confidence intervals the exposures overlap, suggesting that there is no significant difference in nhr-57 expression between the exposures. This may either imply that LMM species fraction of CoNPs, which account for approximately 15% of the Co concentration in CoNP exposures at T-0, is more bioavailable than the Co^{2+} in $CoCl_2$ exposure, or that CoNPs induce hypoxic response through particle-specific mechanisms.

5.6. Limitations in toxicity assessment

Assessment of toxicity

Ideally, the concentration of each exposure during each toxicity should have been determined to get the most accurate assessment of dose and effect. Thus, the mean Co exposure concentration used to assess observed reductions of growth and reproduction might not accurately represent the actual Co exposure concentration during these exposures, as well as caused inaccurate predictions of reproduction EC_{50} values.

Additionally, the two-fold dilution series used during the preparation of the toxicity tests resulted in wide intervals between exposure groups. This has led to interpolation of the linear regression analyses, particularly for those assessing the correlation between the toxicological endpoints, growth, and reproduction, and LMM species concentration. Thereby affecting the reliability of the conclusions drawn from these analyses.

Assessment of morphological effects

As for the assessment of toxicity, not knowing the accurate concentrations that the nematodes were exposed to might have led to uncertainties regarding the interpretations and comparison of the observed morphological effects.

During the acute exposure, the range of exposure concentrations of both $CoCl_2$ and CoNPs was narrower compared to the chronic exposure, thus limiting the information of effects outside these ranges. A wider exposure concentration range would perhaps have included concentration $CoCl_2$ that had no occurrences of the observed vulva abnormalities, giving an estimate of the no effect concentration.

Assessment of hypoxic response

During cultivation *C. elegans* are incubated with gentle shaking to ensure sufficient O_2, however, the O_2 levels during cultivation is not controlled. Therefore, hypoxia induced due to low O_2 might be a possible confounding factor in the assessment of induction of hypoxic response due to CoNP exposure.

Lack of accurate measurement of exposure concentration used to assess hypoxic response might have led to uncertainties in the results and interpretations.

During the investigating of nhr-57 expression in the region of interest, the isolation and definition of the area were based on a subjective judgment rather than an objective standard.

This could have led to unrepresentative measurements of mean fluorescence in these areas and led to inaccurate analyses and results.

5.6. Future work

In this project, it has been demonstrated that CoNPs cause significant toxicity in *C.* elegans, particularly reproduction. The particle-specific mechanism involved in the toxicity of CoNPs, should be investigated in future studies.

CoNPs have also been shown to induce hypoxic response in *C. elegans.* This response was particularly prevalent in the mature embryos that were retained. Future studies could look into the molecular mechanisms that cause nhr-57 expression in embryos. It would also be interesting to learn more about bagging exhibited by the exposed nematodes.

The vulva abnormalities observed in nematodes exposed to $CoCl_2$ should also be investigated further. Perhaps CoNPs do induce such abnormalities but at other exposure concentrations then the concentrations used in this project.

6. Conclusion

In this master's thesis, CoNPs were characterized, and their toxicity and induction of hypoxic response were assessed using *C. elegans* as a model organism.

CoNPs were characterized with respect to size and charge. TEM micrographs suggested that individual NPs had a particle size of less than 10 nm, while DLS measurements determined a hydrodynamic diameter size of approximately 156 nm with a PDI value of around 0.362, indicating NP aggregation. The zeta potential of CoNPs in MHRW was around -16.2 mV, indicating low suspension stability.

Chronic toxicity tests revealed that CoNPs cause less potent toxicity on growth and reproduction compared to $CoCl_2$ at equal Co concentrations. Further, it was demonstrated that toxicity could to an extent be ascribed to LMM. Additionally, a strong correlation between growth and reproduction was revealed. However, CoNPs were shown to reduce reproduction in even fully developed nematodes, unlike $CoCl_2$. This suggests that CoNPs might have particle-specific mechanisms that contribute to reduced reproduction. This supports the hypothesis that particle-specific mechanisms contribute to the toxicity of CoNPs.

Acute exposure to $CoCl_2$ revealed significant vulva abnormalities across all exposure concentrations, suggesting that exposure coinciding with the time of vulva development may lead to abnormal egg laying and result in bagging. Such vulva abnormalities were not observed in nematodes exposed to CoNPs. However, nematodes exposed to CoNPs did exhibit bagging.

The induction of hypoxic response was assessed by investigating the expression *nhr-57* gene. It was revealed that development influenced the induction of nhr-57 expression significantly. Acute CoNP exposure in ZG444 induced a significant induction of nhr-57 expression, which was comparable to the induction by $CoCl_2$. This suggests that other particle-specific mechanisms might induce nhr-57 expression, possibly through a pathway not regulated by EGL-9. This supports both hypotheses formulated in this thesis: particle-specific mechanisms contribute to the toxicity of CoNPs and CoNP exposure induces a significant hypoxic response in *C. elegans.*

Observations also showed that nhr-57 expression is highly localized to embryos. By assessing the expression of nhr-57 in the region of interest, it was revealed that both $CoCl_2$ and CoNPs induce a hypoxic response, unless they cause significant effect on development which in turn causes repression of the hypoxic response. No significant difference was observed in the nhr-

57 expression between nematodes exposed to $CoCl_2$ and CoNPs. These observations imply that particle-specific mechanisms contribute to the induction of hypoxic response. This supports both hypotheses formulated in this thesis: particle-specific mechanisms contribute to the toxicity of CoNPs and CoNP exposure induces a significant hypoxic response in *C. elegans.*

The findings in this master's thesis suggest that particle-specific mechanisms that contribute to the toxicity of CoNPs and induction of hypoxic response should be investigated further. Additionally, the mechanisms behind the vulva abnormalities observed should also be investigated further in future studies.

References

Agmo Hernández, V. (2023). An overview of surface forces and the DLVO theory. *ChemTexts*, *9*(4), 10. https://doi.org/10.1007/s40828-023-00182-9

Albanese, A., & Chan, W. C. W. (2011). Effect of Gold Nanoparticle Aggregation on Cell Uptake and Toxicity. *ACS Nano*, *5*(7), 5478–5489. https://doi.org/10.1021/nn2007496

Altun, Z. F., & Hall, D. H. (2009). WormAtas Hermaphrodite Handbook—Introduction. *WormAtlas*. https://doi.org/10.3908/wormatlas.1.1

Alves, C. S., Melo, M. N., Franquelim, H. G., Ferre, R., Planas, M., Feliu, L., Bardají, E., Kowalczyk, W., Andreu, D., Santos, N. C., Fernandes, M. X., & Castanho, M. A. R. B. (2010). Escherichia coli Cell Surface Perturbation and Disruption Induced by Antimicrobial Peptides BP100 and pepR. *Journal of Biological Chemistry*, *285*(36), 27536–27544. https://doi.org/10.1074/jbc.M110.130955

Ansari, S. M., Bhor, R. D., Pai, K. R., Sen, D., Mazumder, S., Ghosh, K., Kolekar, Y. D., & Ramana, C. V. (2017). Cobalt nanoparticles for biomedical applications: Facile synthesis, physiochemical characterization, cytotoxicity behavior and biocompatibility. *Applied Surface Science*, *414*, 171–187. https://doi.org/10.1016/j.apsusc.2017.03.002

Arenas-Alatorre, J., Silva-Velazquez, Y., Alva Medina, A., & Rivera, M. (2010). Advantages and limitations of OM, SEM, TEM and AFM in the study of ancient decorated pottery. *Applied Physics A*, *98*(3), 617–624. https://doi.org/10.1007/s00339-009-5451-4

Auffan, M., Decome, L., Rose, J., Orsiere, T., De Meo, M., Briois, V., Chaneac, C., Olivi, L., Berge-lefranc, J., Botta, A., Wiesner, M. R., & Bottero, J. (2006). In Vitro Interactions between DMSA-Coated Maghemite Nanoparticles and Human Fibroblasts: A Physicochemical and Cyto-Genotoxical Study. *Environmental Science & Technology*, *40*(14), 4367–4373. https://doi.org/10.1021/es060691k

Barceloux, D. G. (1999). Cobalt. *Journal of Toxicology: Clinical Toxicology*, *37*(2), 201–216. https://doi.org/10.1081/CLT-100102420

Berra, E., Ginouvès, A., & Pouysségur, J. (2006). The hypoxia-inducible-factor hydroxylases bring fresh air into hypoxia signalling. *EMBO Reports*, *7*(1), 41–45. https://doi.org/10.1038/sj.embor.7400598

Bhattacharjee, S. (2016). DLS and zeta potential – What they are and what they are not? *Journal of Controlled Release*, *235*, 337–351. https://doi.org/10.1016/j.jconrel.2016.06.017

Brenner, S. (1974). THE GENETICS OF *CAENORHABDITIS ELEGANS*. *Genetics*, *77*(1), 71–94. https://doi.org/10.1093/genetics/77.1.71

Brewer, K., Maylin, G. A., Fenger, C. K., & Tobin, T. (2016). Cobalt use and regulation in horseracing: A review. *Comparative Exercise Physiology*, *12*(1), 1–10. https://doi.org/10.3920/CEP140008

Brunner, T. J., Wick, P., Manser, P., Spohn, P., Grass, R. N., Limbach, L. K., Bruinink, A., & Stark, W. J. (2006). In Vitro Cytotoxicity of Oxide Nanoparticles: Comparison to Asbestos, Silica, and the Effect of Particle Solubility. *Environmental Science & Technology*, *40*(14), 4374–4381. https://doi.org/10.1021/es052069i

Burkemper, N. M. (2015). Contact Dermatitis, Patch Testing, and Allergen Avoidance. *Missouri Medicine*, *112*(4), 296–300.

Cagno, S., Brede, D. A., Nuyts, G., Vanmeert, F., Pacureanu, A., Tucoulou, R., Cloetens, P., Falkenberg, G., Janssens, K., Salbu, B., & Lind, O. C. (2017). Combined Computed Nanotomography and Nanoscopic X-ray Fluorescence Imaging of Cobalt Nanoparticles in *Caenorhabditis elegans*. *Analytical Chemistry*, *89*(21), 11435–11442. https://doi.org/10.1021/acs.analchem.7b02554

Campbell, G. A. (2020). The cobalt market revisited. *Mineral Economics*, *33*(1–2), 21–28. https://doi.org/10.1007/s13563-019-00173-8

Campbell, P. G. C., Hodson, P. V., Welbourn, P. M., & Wright, D. A. (2022). *Ecotoxicology*. Cambridge university press.

Chalfie, M., Tu, Y., Euskirchen, G., Ward, W. W., & Prasher, D. C. (1994). Green Fluorescent Protein as a Marker for Gene Expression. *Science*, *263*(5148), 802–805. https://doi.org/10.1126/science.8303295

Chen, J., & Caswell-Chen, E. P. (2004). Facultative Vivipary is a Life-History Trait in Caenorhabditis elegans. *Journal of Nematology*, *36*(2), 107–113.

Chen, L., Huang, Y., Huang, L., Liu, B., Wang, G., & Yu, S. (2011). Characterization of Co(II) removal from aqueous solution using bentonite/iron oxide magnetic composites. *Journal of Radioanalytical and Nuclear Chemistry*, *290*(3), 675–684. https://doi.org/10.1007/s10967-011-1337-y

Clogston, J. D., & Patri, A. K. (2011). Zeta Potential Measurement. In S. E. McNeil (Ed.), *Characterization of Nanoparticles Intended for Drug Delivery* (Vol. 697, pp. 63–70). Humana Press. https://doi.org/10.1007/978-1-60327-198-1_6

Colognato, R., Bonelli, A., Ponti, J., Farina, M., Bergamaschi, E., Sabbioni, E., & Migliore, L. (2008). Comparative genotoxicity of cobalt nanoparticles and ions on human peripheral leukocytes in vitro. *Mutagenesis*, *23*(5), 377–382. https://doi.org/10.1093/mutage/gen024

Corsi, A. K., Wightman, B., & Chalfie, M. (2015). A Transparent Window into Biology: A Primer on *Caenorhabditis elegans*. *Genetics*, *200*(2), 387–407. https://doi.org/10.1534/genetics.115.176099

Coutris, C., Hertel-Aas, T., Lapied, E., Joner, E. J., & Oughton, D. H. (2012). Bioavailability of cobalt and silver nanoparticles to the earthworm *Eisenia fetida*. *Nanotoxicology*, *6*(2), 186–195. https://doi.org/10.3109/17435390.2011.569094

Davidson, M. W., & Abramowitz, M. (1999). Optical microscopy. *National High Magnetic Field Laboratory at The Florida State University*, 41. https://doi.org/10.29172/a40cc113-e132-471a-bb1b-2d29d8248a64

De Jong. (2008). Drug delivery and nanoparticles: Applications and hazards. *International Journal of Nanomedicine*, 133. https://doi.org/10.2147/IJN.S596

Derjaguin, B. V., Churaev, N. V., & Muller, V. M. (1987). The Derjaguin—Landau—Verwey—Overbeek (DLVO) Theory of Stability of Lyophobic Colloids. In B. V. Derjaguin, N. V. Churaev, & V. M. Muller, *Surface Forces* (pp. 293–310). Springer US. https://doi.org/10.1007/978-1-4757-6639-4_8

Donaldson, K. (2004). Nanotoxicology. *Occupational and Environmental Medicine*, *61*(9), 727–728. https://doi.org/10.1136/oem.2004.013243

Duarte, I., Mendonça, R. F., Korkes, K. L., Lazzarini, R., & Hafner, M. D. F. S. (2018). Nickel, chromium and cobalt: The relevant allergens in allergic contact dermatitis. Comparative study between two periods: 1995-2002 and 2003-2015. *Anais Brasileiros de Dermatologia*, *93*(1), 59–62. https://doi.org/10.1590/abd1806-4841.20186047

Emmons, S. W. (2014). The development of sexual dimorphism: Studies of the *CAENORHABDITIS elegans* male. *WIREs Developmental Biology*, *3*(4), 239–262. https://doi.org/10.1002/wdev.136

Epstein, A. C. R., Gleadle, J. M., McNeill, L. A., Hewitson, K. S., O'Rourke, J., Mole, D. R., Mukherji, M., Metzen, E., Wilson, M. I., Dhanda, A., Tian, Y.-M., Masson, N., Hamilton, D. L., Jaakkola, P., Barstead, R., Hodgkin, J., Maxwell, P. H., Pugh, C. W., Schofield, C. J., & Ratcliffe, P. J. (2001). C. elegans EGL-9 and Mammalian Homologs Define a Family of Dioxygenases that Regulate HIF by Prolyl Hydroxylation. *Cell*, *107*(1), 43–54. https://doi.org/10.1016/S0092-8674(01)00507-4

Fernando, I., Qian, T., & Zhou, Y. (2019). Long term impact of surfactants & polymers on the colloidal stability, aggregation and dissolution of silver nanoparticles. *Environmental Research*, *179*, 108781. https://doi.org/10.1016/j.envres.2019.108781

Fouad, A. S., & Hafez, R. M. (2018). Effect of cobalt nanoparticles and cobalt ions on alkaloids production and expression of CrMPK3 gene in Catharanthus roseus suspension cultures. *Cellular and Molecular Biology*, *64*(12), 62–69. https://doi.org/10.14715/cmb/2018.64.12.13

Foxler, D. E., Bridge, K. S., Foster, J. G., Grevitt, P., Curry, S., Shah, K. M., Davidson, K. M., Nagano, A., Gadaleta, E., Rhys, H. I., Kennedy, P. T., Hermida, M. A., Chang, T.-Y., Shaw, P. E., Reynolds, L. E., McKay, T. R., Wang, H.-W., Ribeiro, P. S., Plevin, M. J., … Sharp, T. V. (2018). A HIF-LIMD1 negative feedback mechanism mitigates the pro-tumorigenic effects of hypoxia. *EMBO Molecular Medicine*, *10*(8), e8304. https://doi.org/10.15252/emmm.201708304

Fu, X., Beatty, D. N., Gaustad, G. G., Ceder, G., Roth, R., Kirchain, R. E., Bustamante, M., Babbitt, C., & Olivetti, E. A. (2020). Perspectives on Cobalt Supply through 2030 in the Face of Changing Demand. *Environmental Science & Technology*, *54*(5), 2985–2993. https://doi.org/10.1021/acs.est.9b04975

Gaikwad, A. V., Holuigue, A., Thathagar, M. B., ten Elshof, J. E., & Rothenberg, G. (2007). Ion- and Atom-Leaching Mechanisms from Palladium Nanoparticles in Cross-Coupling Reactions. *Chemistry – A European Journal*, *13*(24), 6908–6913. https://doi.org/10.1002/chem.200700105

Ginouvès, A., Ilc, K., Macías, N., Pouysségur, J., & Berra, E. (2008). PHDs overactivation during chronic hypoxia "desensitizes" HIFα and protects cells from necrosis. *Proceedings of the National Academy of Sciences*, *105*(12), 4745–4750. https://doi.org/10.1073/pnas.0705680105

González-Montaña, J.-R., Escalera-Valente, F., Alonso, A. J., Lomillos, J. M., Robles, R., & Alonso, M. E. (2020). Relationship between Vitamin B12 and Cobalt Metabolism in Domestic Ruminant: An Update. *Animals*, *10*(10), 1855. https://doi.org/10.3390/ani10101855

Handy, R. D., Van Den Brink, N., Chappell, M., Mühling, M., Behra, R., Dušinská, M., Simpson, P., Ahtiainen, J., Jha, A. N., Seiter, J., Bednar, A., Kennedy, A., Fernandes, T. F., & Riediker, M. (2012). Practical considerations for conducting ecotoxicity test methods with manufactured nanomaterials: What have we learnt so far? *Ecotoxicology*, *21*(4), 933–972. https://doi.org/10.1007/s10646-012-0862-y

Hassan, P. A., Rana, S., & Verma, G. (2015). Making Sense of Brownian Motion: Colloid Characterization by Dynamic Light Scattering. *Langmuir*, *31*(1), 3–12. https://doi.org/10.1021/la501789z

Hockel, M., & Vaupel, P. (2001). Tumor Hypoxia: Definitions and Current Clinical, Biologic, and Molecular Aspects. *JNCI Journal of the National Cancer Institute*, *93*(4), 266–276. https://doi.org/10.1093/jnci/93.4.266

Hunt, P. R. (2017). The *C. elegans* model in toxicity testing. *Journal of Applied Toxicology*, *37*(1), 50–59. https://doi.org/10.1002/jat.3357

ISO. (2017). *Particle size analysis- Dynamic light scattering (DLS) (ISO Standard No. 22412:2017)*. International Organization for Standardization.

ISO. (2020). *Water and soil quality—Determination of the toxic effect of sediment and soil samples on growth, fertility and reproduction of Caenorhabditis elegans (Nematoda) (ISO standard no. 10872:2020)*. International Organization for Standardization.

Jiang, J., Oberdörster, G., & Biswas, P. (2009). Characterization of size, surface charge, and agglomeration state of nanoparticle dispersions for toxicological studies. *Journal of Nanoparticle Research*, *11*(1), 77–89. https://doi.org/10.1007/s11051-008-9446-4

Jomova, K., & Valko, M. (2011). Advances in metal-induced oxidative stress and human disease. *Toxicology*, *283*(2–3), 65–87. https://doi.org/10.1016/j.tox.2011.03.001

Kent, C. (1998). *Basics of toxicology*. Wiley. https://books.google.no/books?hl=no&lr=&id=VEUlWz4vQssC&oi=fnd&pg=PR9&dq=toxicology+definitions&ots=0ueDdRRaWY&sig=VYXZcnz-9Jj-m38WpS1EkmdQvgQ&redir_esc=y#v=onepage&q&f=false

Khusnuriyalova, A. F., Caporali, M., Hey-Hawkins, E., Sinyashin, O. G., & Yakhvarov, D. G. (2021). Preparation of Cobalt Nanoparticles. *European Journal of Inorganic Chemistry*, *2021*(30), 3023–3047. https://doi.org/10.1002/ejic.202100367

Kiontke, K. C., Félix, M.-A., Ailion, M., Rockman, M. V., Braendle, C., Pénigault, J.-B., & Fitch, D. H. (2011). A phylogeny and molecular barcodes for Caenorhabditis, with numerous new species from rotting fruits. *BMC Evolutionary Biology*, *11*(1), 339. https://doi.org/10.1186/1471-2148-11-339

Kleiven, M., Rossbach, L. M., Gallego-Urrea, J. A., Brede, D. A., Oughton, D. H., & Coutris, C. (2018). Characterizing the behavior, uptake, and toxicity of NM300K silver nanoparticles in *Caenorhabditis elegans*. *Environmental Toxicology and Chemistry*, *37*(7), 1799–1810. https://doi.org/10.1002/etc.4144

Kosler, J., & Sylvester, P. J. (2003). Present Trends and the Future of Zircon in Geochronology: Laser Ablation ICPMS. *Reviews in Mineralogy and Geochemistry*, *53*(1), 243–275. https://doi.org/10.2113/0530243

Leica Microsystems GmBH. (2020). *POWERFUL UPRIGHT MICROSCOPE SOLUTIONS FOR LIFE SCIENCE AND CLINICAL APPLICATIONS Leica DM4 B Leica DM6 B*.

Leonard, S., M. Gannett, P., Rojanasakul, Y., Schwegler-Berry, D., Castranova, V., Vallyathan, V., & Shi, X. (1998). Cobalt-mediated generation of reactive oxygen species and its possible mechanism. *Journal of Inorganic Biochemistry*, *70*(3–4), 239–244. https://doi.org/10.1016/S0162-0134(98)10022-3

Leyssens, L., Vinck, B., Van Der Straeten, C., Wuyts, F., & Maes, L. (2017). Cobalt toxicity in humans—A review of the potential sources and systemic health effects. *Toxicology*, *387*, 43–56. https://doi.org/10.1016/j.tox.2017.05.015

Liao, W.-H., Aggarwal, S. J., & Aggarwal, J. K. (1997). The reconstruction of dynamic 3D structure of biological objects using stereo microscope images. *Machine Vision and Applications*, *9*(4), 166–178. https://doi.org/10.1007/s001380050038

Lin, P.-C., Lin, S., Wang, P. C., & Sridhar, R. (2014). Techniques for physicochemical characterization of nanomaterials. *Biotechnology Advances*, *32*(4), 711–726. https://doi.org/10.1016/j.biotechadv.2013.11.006

Lints, R., & Hall, D. H. (2004). WormAtlas Hermaphrodite Handbook—Reproductive System—Egg-laying Apparatus. *WormAtlas*. https://doi.org/10.3908/wormatlas.1.24

Ma, R., Zhou, G., Gu, M., Tang, X., Ding, W., Guan, Y., Jiang, Y., Yin, J., Zhang, L., & Huixiang Ang, E. (2024). Cobalt leaching inhibition: Transforming coordination polymers into spherical Co3O4@NC catalysts for accelerated tetracycline degradation via enhanced PMS activation. *Applied Surface Science*, *648*, 158980. https://doi.org/10.1016/j.apsusc.2023.158980

Majtan, T., Frerman, F. E., & Kraus, J. P. (2011). Effect of cobalt on Escherichia coli metabolism and metalloporphyrin formation. *BioMetals*, *24*(2), 335–347. https://doi.org/10.1007/s10534-010-9400-7

Malvern Instruments Ltd. (2013). *Zetasizer Nano Series User Manual*.

Mango, S. (2007). The C. elegans pharynx: A model for organogenesis. *WormBook*. https://doi.org/10.1895/wormbook.1.129.1

Mann, C. J., Yu, L., Lo, C.-M., & Kim, M. K. (2005). High-resolution quantitative phase-contrast microscopy by digital holography. *Optics Express*, *13*(22), 8693. https://doi.org/10.1364/OPEX.13.008693

Maxeiner, S., Grolleman, J., Schmid, T., Kammenga, J., & Hajnal, A. (2019). The hypoxia-response pathway modulates RAS/MAPK–mediated cell fate decisions in *Caenorhabditis elegans*. *Life Science Alliance*, *2*(3), e201800255. https://doi.org/10.26508/lsa.201800255

Meneely, P. M., Dahlberg, C. L., & Rose, J. K. (2019). Working with Worms: *Caenorhabditis elegans* as a Model Organism. *Current Protocols Essential Laboratory Techniques*, *19*(1), e35. https://doi.org/10.1002/cpet.35

Mörck, C., Axäng, C., & Pilon, M. (2003). A genetic analysis of axon guidance in the C. elegans pharynx. *Developmental Biology*, *260*(1), 158–175. https://doi.org/10.1016/S0012-1606(03)00238-0

Nelson, D. L., Cox, M. M., & Lehninger, A. L. (2017). *Lehninger principles of biochemistry* (Seventh edition). W.H. Freeman and Company ; Macmillan Higher Education.

Osman, D., Cooke, A., Young, T. R., Deery, E., Robinson, N. J., & Warren, M. J. (2021). The requirement for cobalt in vitamin B12: A paradigm for protein metalation. *Biochimica et Biophysica Acta (BBA) - Molecular Cell Research*, *1868*(1), 118896. https://doi.org/10.1016/j.bbamcr.2020.118896

Oughton, D. H., Hertel-Aas, T., Pellicer, E., Mendoza, E., & Joner, E. J. (2008). Neutron activation of engineered nanoparticles as a tool for tracing their environmental fate and uptake in organisms. *Environmental Toxicology and Chemistry*, *27*(9), 1883–1887. https://doi.org/10.1897/07-578.1

Padmanabha, D., Padilla, P. A., You, Y.-J., & Baker, K. D. (2015). A HIF-Independent Mediator of Transcriptional Responses to Oxygen Deprivation in *Caenorhabditis elegans*. *Genetics*, *199*(3), 739–748. https://doi.org/10.1534/genetics.114.173989

Patel, V. B. (2020). *Molecular nutrition: Vitamins*. Academic press.

Pisanic, T. R., Blackwell, J. D., Shubayev, V. I., Fiñones, R. R., & Jin, S. (2007). Nanotoxicity of iron oxide nanoparticle internalization in growing neurons. *Biomaterials*, *28*(16), 2572–2581. https://doi.org/10.1016/j.biomaterials.2007.01.043

Pope, C. N., Schlenk, D., & Baud, F. J. (2020). History and basic concepts of toxicology. In *An Introduction to Interdisciplinary Toxicology* (pp. 3–15). Elsevier. https://doi.org/10.1016/B978-0-12-813602-7.00001-6

Pourmand, A., & Abdollahi, M. (2012). Current Opinion on Nanotoxicology. *DARU Journal of Pharmaceutical Sciences*, *20*(1), 95, 2008-2231-20–95. https://doi.org/10.1186/2008-2231-20-95

Prabhakar, N. R., & Semenza, G. L. (2015). Oxygen Sensing and Homeostasis. *Physiology*, *30*(5), 340–348. https://doi.org/10.1152/physiol.00022.2015

Prasher, D. C., Eckenrode, V. K., Ward, W. W., Prendergast, F. G., & Cormier, M. J. (1992). Primary structure of the Aequorea victoria green-fluorescent protein. *Gene*, *111*(2), 229–233. https://doi.org/10.1016/0378-1119(92)90691-H

Pröfrock, D., & Prange, A. (2012). Inductively Coupled Plasma–Mass Spectrometry (ICP-MS) for Quantitative Analysis in Environmental and Life Sciences: A Review of Challenges, Solutions, and Trends. *Applied Spectroscopy*, *66*(8), 843–868. https://doi.org/10.1366/12-06681

Ranquet, C., Ollagnier-de-Choudens, S., Loiseau, L., Barras, F., & Fontecave, M. (2007). Cobalt Stress in Escherichia coli. *Journal of Biological Chemistry*, *282*(42), 30442–30451. https://doi.org/10.1074/jbc.M702519200

Rejman, J., Oberle, V., Zuhorn, I. S., & Hoekstra, D. (2004). Size-dependent internalization of particles via the pathways of clathrin- and caveolae-mediated endocytosis. *Biochemical Journal*, *377*(1), 159–169. https://doi.org/10.1042/bj20031253

Rizzo, G., & Laganà, A. S. (2020). A review of vitamin B12. In *Molecular Nutrition* (pp. 105–129). Elsevier. https://doi.org/10.1016/B978-0-12-811907-5.00005-1

Sanderson, M. J., Smith, I., Parker, I., & Bootman, M. D. (2014). Fluorescence Microscopy. *Cold Spring Harbor Protocols*, *2014*(10), pdb.top071795. https://doi.org/10.1101/pdb.top071795

Shao, Z., Zhang, Y., & Powell-Coffman, J. A. (2009). Two Distinct Roles for EGL-9 in the Regulation of HIF-1-Mediated Gene Expression in *Caenorhabditis elegans*. *Genetics*, *183*(3), 821–829. https://doi.org/10.1534/genetics.109.107284

Shaye, D. D., & Greenwald, I. (2011). OrthoList: A Compendium of C. elegans Genes with Human Orthologs. *PLoS ONE*, *6*(5), e20085. https://doi.org/10.1371/journal.pone.0020085

Simonsen, L. O., Harbak, H., & Bennekou, P. (2012). Cobalt metabolism and toxicology—A brief update. *Science of The Total Environment*, *432*, 210–215. https://doi.org/10.1016/j.scitotenv.2012.06.009

Slack, J. F., Kimball, B. E., & Shedd, K. B. (2017). *Cobalt, Chapter F of Critical mineral resources of the United States—Economic and environmental geology and prospects for future supply* (1802, pp. F1–F40) [Professional Paper]. U.S. Geological Survey.

Soto, K., Garza, K., & Murr, L. (2007). Cytotoxic effects of aggregated nanomaterials☆. *Acta Biomaterialia*, *3*(3), 351–358. https://doi.org/10.1016/j.actbio.2006.11.004

Stetefeld, J., McKenna, S. A., & Patel, T. R. (2016). Dynamic light scattering: A practical guide and applications in biomedical sciences. *Biophysical Reviews*, *8*(4), 409–427. https://doi.org/10.1007/s12551-016-0218-6

The Royal Society. (2004). *Nanoscience and nanotechnologies: Opportunities and uncertainties*. Royal Society : Royal Academy of Engineering.

Triantafyllou, A., Liakos, P., Tsakalof, A., Georgatsou, E., Simos, G., & Bonanou, S. (2006). Cobalt induces hypoxia-inducible factor-1α (HIF-1α) in HeLa cells by an iron-independent, but ROS-, PI-3K- and MAPK-dependent mechanism. *Free Radical Research*, *40*(8), 847–856. https://doi.org/10.1080/10715760600730810

VanLoon, G. W., & Duffy, S. J. (2017). *Environmental chemistry: A global perspective* (4th ed). Oxford university press.

Vishwakarma, V., Samal, S. S., & Manoharan, N. (2010). Safety and Risk Associated with Nanoparticles—A Review. *Journal of Minerals and Materials Characterization and Engineering*, *09*(05), 455–459. https://doi.org/10.4236/jmmce.2010.95031

Wang, G. L., Jiang, B. H., Rue, E. A., & Semenza, G. L. (1995). Hypoxia-inducible factor 1 is a basic-helix-loop-helix-PAS heterodimer regulated by cellular O2 tension. *Proceedings of the National Academy of Sciences of the United States of America*, *92*(12), 5510–5514. https://doi.org/10.1073/pnas.92.12.5510

Wang, X., & Lai, Y. (2021). Three basic types of fluorescence microscopy and recent improvement. *E3S Web of Conferences*, *290*, 01031. https://doi.org/10.1051/e3sconf/202129001031

Williams, D. B., & Carter, C. B. (2009). The Transmission Electron Microscope. In D. B. Williams & C. B. Carter, *Transmission Electron Microscopy* (pp. 3–22). Springer US. https://doi.org/10.1007/978-0-387-76501-3_1

Wilschefski, S., & Baxter, M. (2019). Inductively Coupled Plasma Mass Spectrometry: Introduction to Analytical Aspects. *Clinical Biochemist Reviews*, *40*(3), 115–133. https://doi.org/10.33176/AACB-19-00024

Yuan, Y., Hilliard, G., Ferguson, T., & Millhorn, D. E. (2003). Cobalt Inhibits the Interaction between Hypoxia-inducible Factor-α and von Hippel-Lindau Protein by Direct Binding to Hypoxia-inducible Factor-α. *Journal of Biological Chemistry*, *278*(18), 15911–15916. https://doi.org/10.1074/jbc.M300463200

Zernike, F. (1942). Phase contrast, a new method for the microscopic observation of transparent objects. *Physica*, *9*(7), 686–698. https://doi.org/10.1016/S0031-8914(42)80035-X

Zhang, W., Li, Z., Wu, G., Wu, W., Zeng, H., Jiang, H., Zhang, W., Wu, R., & Xue, Q. (2023). Effects of Coloration of Spinel CoAl2O4 Cobalt Blue Pigments: Composition, Structure, and Cation Distribution. *Inorganics*, *11*(9), 368. https://doi.org/10.3390/inorganics11090368

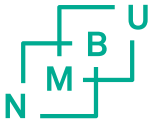

Norges miljø- og biovitenskapelige universitet
Noregs miljø- og biovitskapelege universitet
Norwegian University of Life Sciences

Postboks 5003
NO-1432 Ås
Norway